Summer 2017

Mining asteroids for volatile resources: an experimental demonstration of extraction and recovery

Egboche Christopher Unobe

Department:

MINING ASTEROIDS FOR VOLATILE RESOURCES: AN EXPERIMENTAL DEMONSTRATION OF EXTRACTION AND RECOVERY

by

EGBOCHE CHRISTOPHER UNOBE

A THESIS

Presented to the Faculty of the Graduate School of the

MISSOURI UNIVERSITY OF SCIENCE AND TECHNOLOGY

In Partial Fulfillment of the Requirements for the Degree

MASTER OF SCIENCE IN GEOLOGICAL ENGINEERING

2017

Approved by

Leslie S. Gertsch, Advisor
Micheal Moats
David Wronkiewicz

ABSTRACT

Gaseous compounds trapped within carbonaceous asteroids may prove to be important targets for prospective space miners in the near-term. Volatile release is from hydrated, hydroxylated and carbonated phases present, making such bodies attractive as feedstock for the production of H_2O, CO_2 and simple organic compounds. A source of these species in orbit provides an opportunity to locally produce space-craft propellant and other life-support gases through the application of In-situ Resource Utilization (ISRU).

For this study, an experimental vacuum system was modified and used to test the technical validity of radiatively heating asteroid simulants to extract contained gaseous resources while simultaneously recovering evolved products using a cryogenic trap. A furnace placed within the vacuum chamber carries the sample and provides resistive-radiative heating, temperature is applied in ramped steps and held at four plateaus for extended periods. A mass spectrometer scanning the spectrum from 1-200 atomic mass units records the composition of the residual environment as gas is produced from the simulant and retrieved as a solid icy mixture on the surface of a liquid nitrogen cooled trap. K-type thermocouples emplaced within the simulant sample mass yield information on the nature and progress of heat and mass transfer.

Results indicate that volatile production is driven by predictable endothermic reactions such as dehydration and de-hydroxylation. Material properties of bulk bodies strongly influence the pace of thermal devolatilization and cryo-trapping was found to effectively capture released species within limits.

ACKNOWLEDGMENTS

I acknowledge my maker, the Supreme Being and ultimate Geological engineer, whose mysterious designs obey no known laws but withstand the eternal test of time for giving me the strength and wisdom to carry out this seemingly arduous task with relative ease and without whom my efforts would have been a farce. I must also thank without reservation from the bottom of my heart my advisor Dr. Leslie Gertsch for guiding me through this project. My immense gratitude and appreciation goes to my thesis committee as well as the entire faculty of the department of Geological Engineering for their unalloyed support, training, encouragement, and cheerful willingness to impart priceless knowledge to me. I acknowledge the love and support of my siblings; Ejakuwa, Ikwulono, Ochanya and Adah and from my parents, Professor and Mrs E.A Unobe.

TABLE OF CONTENTS

LIST OF ILLUSTRATIONS

LIST OF TABLES

1. INTRODUCTION

1.1. BACKGROUND AND MOTIVATION

The idea of space mining has enchanted imaginations for decades. Potential natural resources available in the solar system can be divided into those that can be put to use in space and those that can be brought back to Earth and sold. Economic justification for the latter is yet to be established therefore it is appropriate to define a resource based on its predicted value or usefulness in space. Evidence of the presence of iron-nickel alloys, ilmenite, silicates and volatile-bearing minerals have been highlighted in meteoritic and spectroscopic studies of asteroids and comets. Sonter (1997) points at the availability of non-stop solar power at a rate of about 1.3kW/m^2 (thermal) or 100W/m^2 (electrical) as an important natural resource. An increase in human and robotic activities in space will require the utilization of materials such as metals and volatiles for applications ranging from the creation of structures to the manufacture of rocket propellant. The high cost of moving mass from Earth's orbit has made the exploitation of raw materials from non-terrestrial sources an attractive proposition. As such, it is now widely accepted that to extend and expand human exploration across the solar system, these resources must be harnessed and put to use in developing technologies for advanced robotics, power, propulsion, life support and habitats.

A variety of volatile-bearing phases have been identified to be present in carbonaceous asteroids through correlative studies on their spectral properties and from analysis of meteoritic samples. These phases include phyllosilicates, clays and organic compounds known to be capable of releasing gas when heated to sufficient temperatures. This makes carbonaceous asteroids favorable targets for space mining processes geared

towards extracting volatile compounds such as water, carbon dioxide and methane from solar system bodies for use as raw materials. A source of these volatiles in space provides an opportunity to locally produce spacecraft propellant and other life-support gases that could potentially revolutionize the economics of space exploration. Compounds of hydrogen, oxygen, carbon and sulphur may be produced from carbonaceous ore and utilized, either in their raw form or processed into more useful end products. This thesis details experiments conducted using a laboratory-scale, vacuum-pyrolysis system to demonstrate the extraction and recovery of such gases from asteroid simulants.

1.2. THE APPEAL OF IN-SITU RESOURCE UTILIZATION (ISRU)

ISRU is a concept of "living off the land" that involves the utilization of extraterrestrial resources found on bodies such as the Moon, Mars and asteroids to advance the exploration and commercial development of space (Sanders et al., 2000). Within this strategic plan, technologies related to resource extraction, resource processing, surface construction and manufacturing with space resources will be developed. Among the benefits of this approach is its potential to reduce the mass, cost and risk of near and long term human and robotic space exploration while providing a platform for the development of capabilities that enable space exploration (Sanders et al, 2005).

In-situ mining of volatile resources from asteroids is directly related to a key sub-set of the ISRU strategic plan outlined by Sanders et al., (2000) and termed In-Situ Consumable Production (ISCP). It calls for acquiring, manufacturing, and storing propellants for planetary vehicles, gases and water for crew, life support and fuel cell reagents for power generation using resources available at the site of exploration.

1.3. PROBLEM DEFINITION AND SCOPE

A resource may be defined as anything with the potential of being mined for a net benefit while recovery is the proportion of the in-place resource that can be separated from waste material. In conventional terrestrial resource extraction, four major stages define the process:

a) Resource assessment involves the determination of what is available, its location, its form and the best method for extraction.
b) Resource acquisition involves the separation and removal of the target material-gas, liquid, and/or solid from the parent body.
c) Resource beneficiation involves the conversion of the raw material into a form suitable for direct use, manufacturing, or further processing.
d) Site management comprises of activities needed for a safe and effective operation.

The volatile resources in carbonaceous asteroids have been assessed (see discussion in Section 2). This research project largely falls within the realm of resource acquisition which is concerned with separating and recovering the desired volatile material from its parent body. Resource beneficiation and site management are beyond the scope of this work.

The discussion here is largely based on a mining method where the asteroid body of interest is in some fashion completely enclosed within a low pressure vessel and heated (see discussion of some proposed mining concepts in section 2). No attempt is made to separate volatile bearing minerals from inert and non-reactive minerals meaning the entire body is subjected to the process selected as the extraction mechanism. Heating asteroids in

bulk introduces uncertainties related to the influence of heat and mass transfer through the body, the effect of fluid-fluid and fluid-rock interactions on the nature and amount of recovered products, and the net effect of de-volatilization on the material properties of the body.

The selection, design and operation of a feasible metallurgical or mining process in resource development often requires extensive research. This study explores volatile resource acquisition from carbonaceous asteroids by providing qualitative and quantitative information on volatile release as a function of increasing temperature. Extraction is experimentally studied, primarily from the point of view of yield and recovery as the quantification of these parameters is vital in the determination of economic feasibility. Using large samples with embedded thermocouples allow for the observation of the influence of key variables such as heat and mass transport. In addition, recovering gaseous products by cryogenic means reveal some of the factors that determine the efficacy of this method. Herein, specific information important to the development of any mining system designed to produce volatiles from carbonaceous bodies is provided.

1.4. OBJECTIVES AND SIGNIFICANCE

This experimental project is a demonstration of resource acquisition from bulk volatile-rich asteroidal minerals using radiative heating, specifically to answer questions concerning:

a) The nature of gases that can be produced.

b) The temperature at which they evolve.

c) How much can be recovered.

To this end, a laboratory-scale system was designed and built to simulate solar thermal heating in vacuum of carbonaceous asteroid-like material. This apparatus was utilized to evaluate the technical validity of using radiative heat and cryogenic cooling respectively to extract and recover volatile gases derived from hydrated and carbonated phases.

1.5. THESIS OVERVIEW

A major part of this thesis comprises of the presentation of details on a number of vacuum pyrolysis experiments conducted on materials that act as analogs for carbonaceous asteroids. Section 2 reviews relevant and important previous work. Section 3 provides details on the setup of the laboratory system highlighting the technical approach and the methodology adopted in conducting experiments. Section 4 presents and discusses the results that were obtained from the tests while Section 5 presents the inferences that were drawn from results of this exercise.

2. LITERATURE REVIEW

A review of asteroid mining is presented, supported by brief discussions on a number of proposed mining and processing concepts. Current knowledge of the geology of these bodies is also examined on the basis of composition, form and location. Finally, a summary of recent work at devolatilizing carbonaceous (C-type) asteroidal material using thermal methods is laid out, these bodies will be the target of future asteroid mining projects focused on extracting volatile resources.

2.1. ASTEROID MINING AND PROCESSING

The utilization of natural resources already in space was conceived by the first rocketry pioneers as a logical step towards space colonization (Tsiolkovsky, 1903). O'Neill (1974), Johnson and Holbrow (1977) are some of the early writings that recognized the need for materials to feed factories in orbit if space industrialization was to be achieved. The Earth's gravity well makes the transportation of large quantities of equipment and supplies into space to support science and exploration goals infeasible, this has led to the adoption of In-Situ Resource Utilization (ISRU), which calls for substituting Earth derived resources for local resources as the preferred methodology to achieve space industrialization. The benefits and relevance of ISRU concepts are discussed in Sanders et al., (2000, 2005). Low capital investments and quick returns were identified by Cutler and Hughes (1985) as critical to the economic feasibility of space mining. They proposed propellants and metal plate delivered to low Earth orbit (LEO) as the best products for meeting these objectives and also identified the design and development of mining processes as the biggest time bind. Cordell and Steinbronn (1988) found space resources

to be pivotal for large-scale human operations in space and concluded that volatiles should be mined. In a similar vein, Lewis & Lewis, (1987) suggested that access to the huge energy and material resources of the solar system favored space colonization. The development of enabling technologies for tele-robotic and autonomous mining are critical steps to the actualization of extra-terrestrial mining (Mueller and van Susante, 2012). Figure 2.1 shows the main asteroid populations in the solar system.

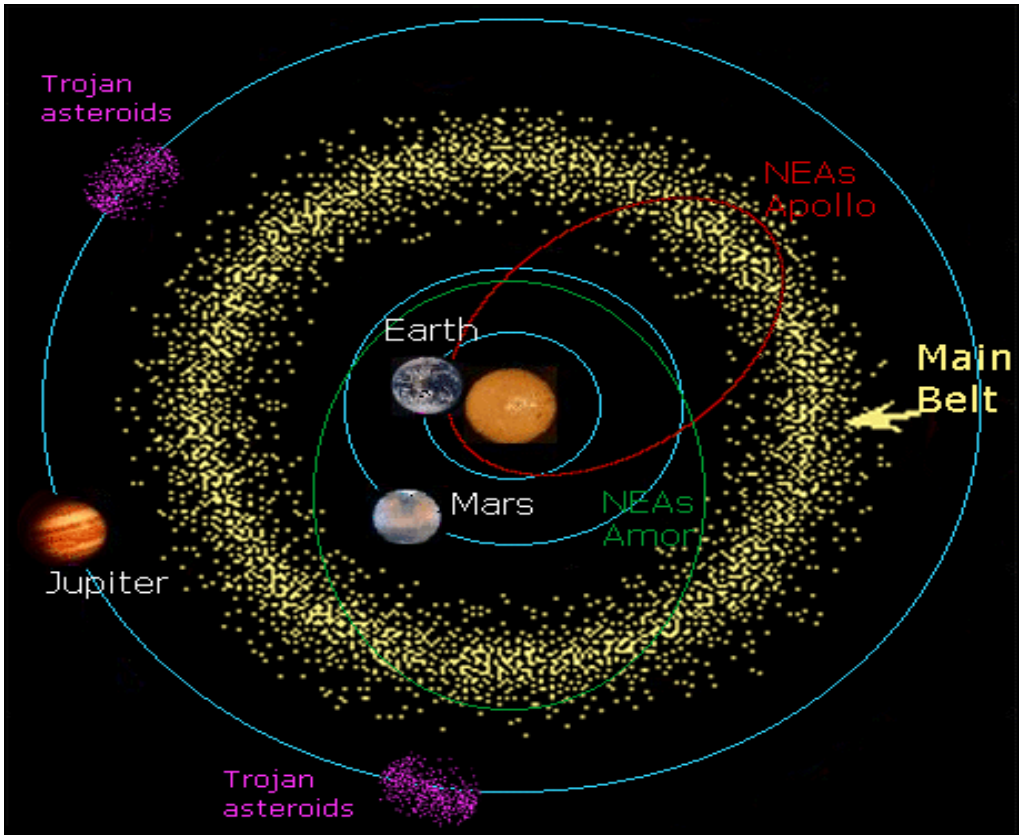

Figure 2.1. Orbit Diagram for Major Asteroid Groups.

Asteroid mining was first discussed by Cox and Cole, (1964) and by Brian O'Leary (1977), Herrick (1979), Morrison and Niehoff (1979), and Kuck (1979). Space industry involving the exploitation of asteroid resources would classify these materials as ores

(defined as any material that can be mined for a net benefit) in the terrestrial sense, and raw materials retrieved would not incur as high a cost as retrieving material from the Earth because of lower energy requirements to return material from a number of possible target asteroids.

Near Earth Asteroids (NEAs) are an especially appealing source of resources because of their accessibility from Earth and their potential wealth (Lewis 1996). They have orbits which pass close to the Earth and just over 16000 of various sizes have been discovered as at June 2017 (Figure 2.2).

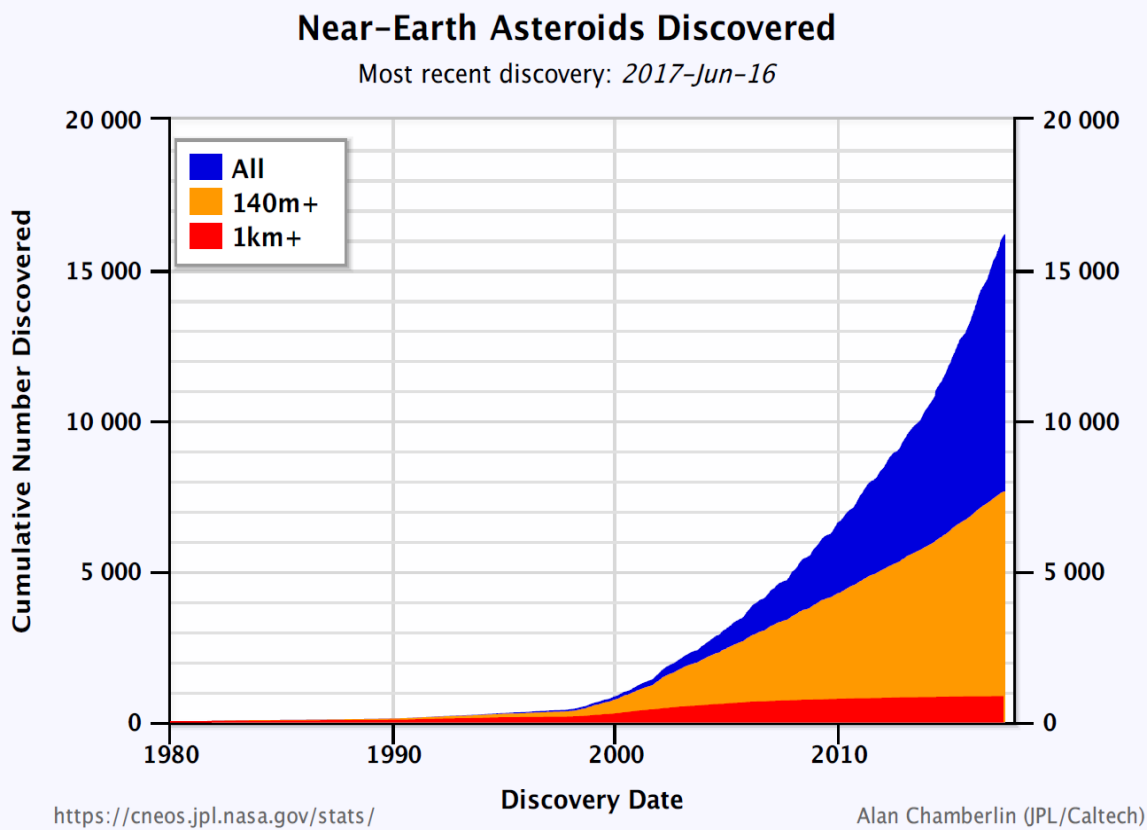

Figure 2.2. Near-Earth Asteroids Discovered. (Alan Chamberlain, JPL/Caltech).

The majority of known asteroids orbit within what is referred to as the main asteroid belt between the orbits of Mars and Jupiter. Tadesco and Desert (2002) estimated that this belt contains as many as 1.1-1.9 million bodies larger than 1km in diameter and millions of smaller ones. Trojans are asteroids that share an orbit with a larger planet or the Moon, the most significant population identified are the Jupiter Trojans. These bodies are compositionally diverse but a good proportion are thought to be volatile-rich (Lewis, 1997) and could be a source of water and other gaseous compounds to be utilized for life support and propellant.

A number of the proposed methods for mining asteroids are based on capturing the targeted body within an enclosure of some sort, partially (Gertsch, R. 1992) or completely (O'Leary 1979, Zacny et al., 2013, Sercel 2016). Gertsch R et al., (1997) and Gertsch L and Gertsch R (2000) postulated that asteroid mining methods based on bags will involve all or some of the following steps:

a) Tether anchoring to the asteroid.
b) Asteroid motion control.
c) Body restraint system placement.
d) Operations platform construction.
e) Bag construction.
f) Auxiliary and support equipment placement.
g) Mining operations.
h) Processing operations.
i) Product transport to markets.

Anchoring and tethering may serve multiple purposes, most importantly to bring the asteroid under control to allow for machinery and possibly people to be affixed to it. A restraint system will serve to hold the body in place while it undergoes the mining process. An operations platform may then be put in place to allow for efficient movement of man and machine. At this point, a lightweight and robust bagging system may deployed. The authors noted that enclosing all or part of the body may serve to mitigate the engineering drawbacks of mining in an unfamiliar environment highlighting the ability of said enclosure to contain material fragments, to provide a processing vessel, and to provide an operating platform for mining machinery. Equipment placement will be based on the mining method selected. The mining and processing selection will depend on the physical characteristics of the body, the use of solar reflectors was recommended for use in devolatilizing gas-rich bodies. The value of the material being mined will control the methods and distance of shipping. While asteroid mining as a concept includes any process that involves the extraction and retention of useful material from asteroids, the discussion that follows is restricted to a review of some in-situ mining concepts concerned with the extraction and retention of useful volatile material.

2.1.1. Robotic Asteroid Prospector (RAP). Zacny et al., (2013) identified water as the commodity most likely to be of value for extraction and sale to customers in space for use as a propellant. The authors designed a prototype prospecting and mining spacecraft (RAP) that utilizes a solar thermal propulsion system fueled by liquid water and incorporated with solar concentrators capable of concentrating sunlight to 10000x the incident insolation (Figure 2.3). An important use of concentrated sunlight in this concept is the provision of process heat to onboard mining, extraction, processing and refining

systems. This approach calls for the capture and in-situ extraction of volatile resources from asteroids less than 20m in size (captive recovery) while those of larger sizes would be mined by smaller robotic spacecraft termed ‘spiders’ which could either deliver feedstock material back to the RAP mother spacecraft for processing (mine-transport-extract) or process material in-situ and deliver only processed material to the RAP (mine-extract in-situ).

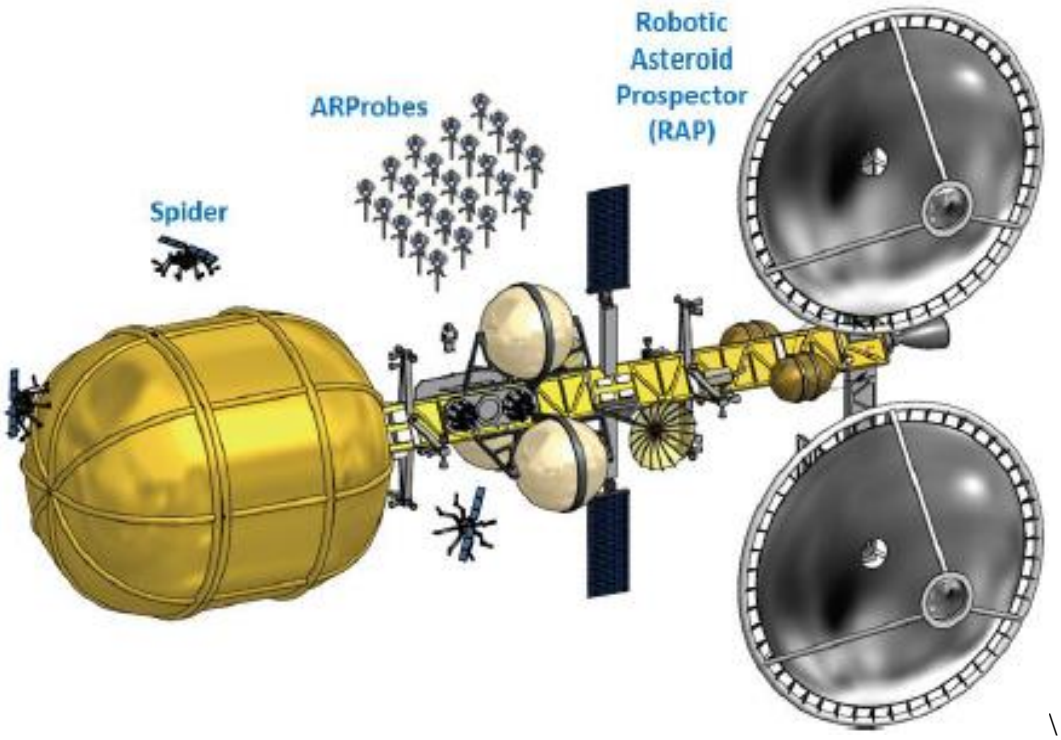

Figure 2.3. The RAP Spacecraft with Spiders and ARProbes. (Zacny et al., 2013).

The asteroid Reconnaissance Probe (ARProbe) would be fully robotic and tasked with acquiring a sample of the asteroid surface for analysis to determine the amount and nature of water present before the mining process begins (Figure 2.4).

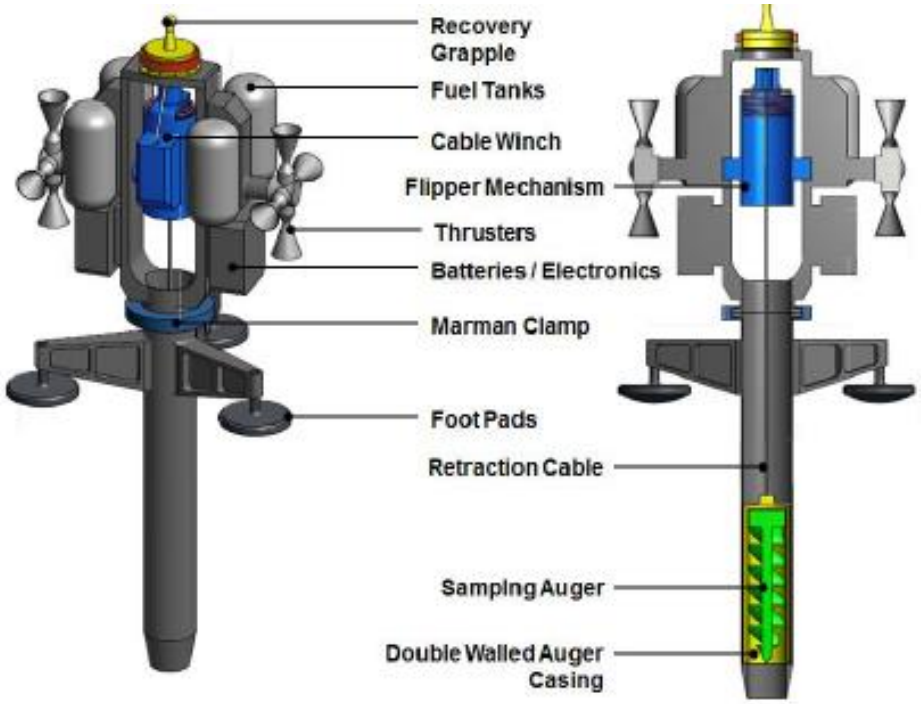

Figure 2.4. ARProbes. (Zacny et al., 2013).

In the notional concept of operations for larger bodies (>20m) the ‘spiders’ which would be robots with augers mounted at the ends of multiple flexible legs would follow to the asteroid surface after the ARProbes, anchor themselves, and acquire loose, ice rich regolith (a layer of loose, heterogeneous material) to either process it in-situ or deliver it to the RAP spacecraft for processing. In captive recovery, an asteroid could be placed inside a bag and sealed. The RAP then directs concentrated sunlight from solar concentrators directly onto the bag which acts to distribute heat evenly around the asteroid surface. Extracted water vapor will then be captured on a cold trap. For in-situ water recovery using ‘spiders’, the auger attached to its legs would dig into ice-bearing regolith to acquire a load of material for processing (Figure 2.5). Once loaded, it retracts into a reactor where it is

heated by electrical means or by use of concentrated sunlight. Extracted water vapor would then be captured on a cold trap.

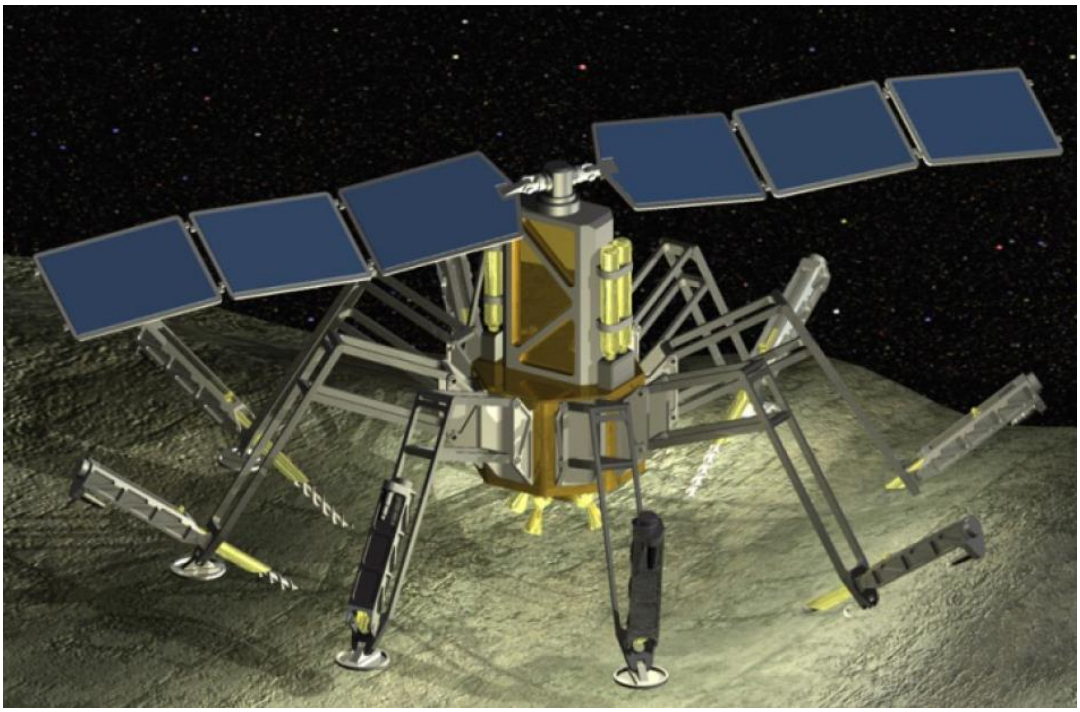

Figure 2.5. Spider. (K. Zacny et al., 2013).

2.1.2. Asteroid Provided In-situ Supplies. Figure 2.6 presents a conceptual diagram of an in situ resource utilization (ISRU) propellant and mission consumable mission architecture called APIS (Asteroid Provided In-Situ Supplies), an approach to the extraction, processing, and delivery of water from asteroids to in-space assets (Sercel, 2016; Personal communication). Optical Mining™ is a key aspect of this approach to exploiting carbonaceous asteroids of their volatile resources by combining material excavation with resource extraction. In this concept, highly concentrated sunlight is delivered to an asteroid captured in a low-pressure inflatable bag causing thermal stress on

the receiving surface. This will result in spalling and continual exposure of new material to the incident beam. High temperatures generated also lead to the simultaneous extraction of water and other volatile compounds from excavated material. Evolved resources are recovered through the application of cryogenic methods.

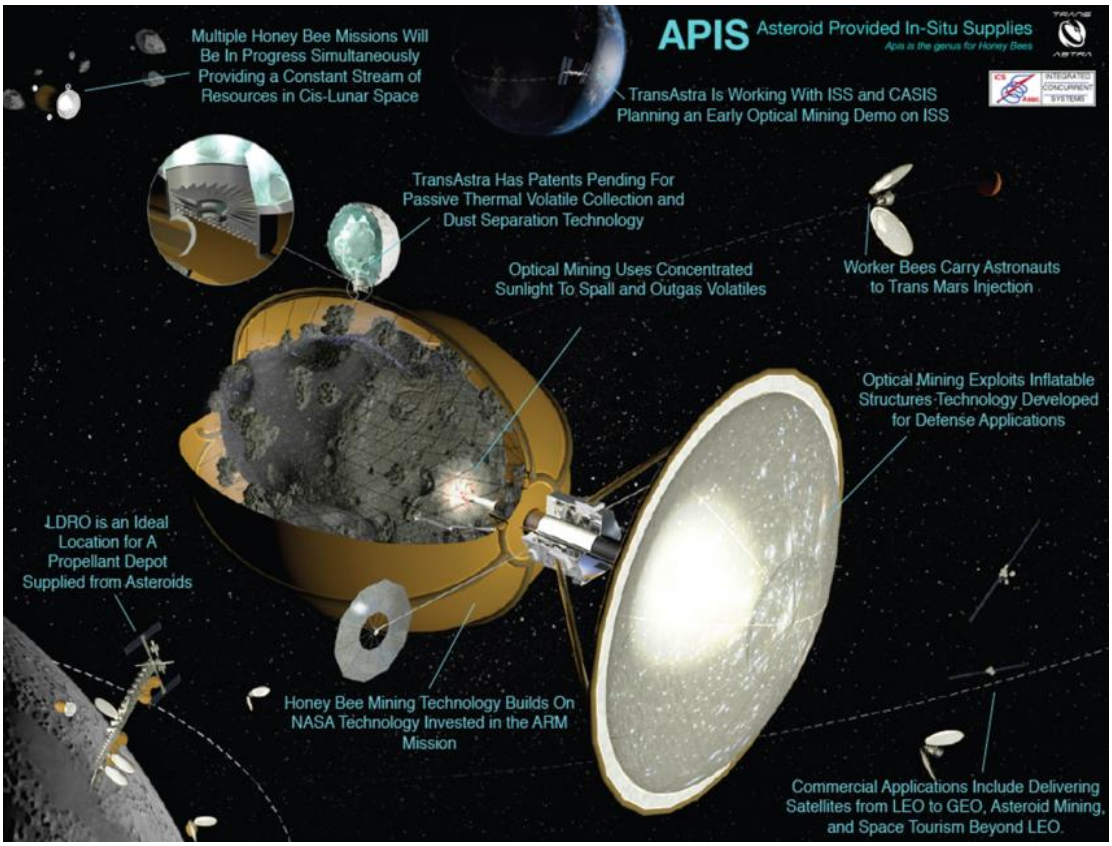

Figure 2.6. APIS Conceptual Diagram. (Sercel, 2016).

2.2. ASTEROID GEOLOGY

When discussing the presence of water (volatiles) in the solar system, the concept of a snow-line is commonly used. The snow line references a heliocentric distance (measured from the center of the sun) at which water-ice is stable enough to accrete to solar system bodies. The general idea is that varying conditions existing within the vicinity of

these bodies during their formation led to the development of a zonal structure ranging from metallic silicates near the sun, through concentrations of organic and rocky material in the mid solar system to concentrations of various ices in the outer system. While some studies (Lunine, 2006) show that the snow-line may have fallen within the main asteroid belt, its placement has varied in different models (Rivkin et al, 2015). Recent observations on the asteroid-comet continuum (Gounell, 2011) and on the intermittent cometary behavior of some main belt and near-Earth asteroids (e.g. Hsieh and Jewitt, 2006; Licandro et al., 2007, 2011b; Jewitt et al., 2013; Mommert et al., 2014) also paint a more complex picture. This study focuses not on water-ice but on mineral-bound volatiles.

Remote sensing remains the primary method for investigating the mineralogy of solar system bodies using three wavelength regions; the visible and near infrared region (~0.4-0.8 um), the 3-um region and the mid-infrared region (5-13 um) but meteorites have given us the most information about the specific minerals present in the asteroids (Rivkin et al., 2015). Of these spectral regions, absorptions in the 3-um region are diagnostic of the presence of water, hydroxyls (OH), methane and other organic species. Carbonaceous meteorites in the meteorite collection also display a strong absorption band in these region establishing a link between these meteorite types and volatile bearing solar system bodies. Hence, characterizing these resources mostly entail investigation conducted on carbonaceous chondrites and remote spectral studies in the 3-um region.

2.2.1. Asteroid and Meteorite Composition. The three main types of asteroids are classified based on meteoritic composition into stony, carbonaceous and metallic. These 3 primary types map into 34 classification sub-types for meteorites (Burbine et al., 2002) but unfortunately, the exact links between the asteroid and meteorite system are uncertain and

so accordingly, the range of possible meteorite types for a given asteroid type can be quite large (Gaffey et al.,1993, Thomas and Binzel., 2010). The C-group includes carbonaceous objects, i.e. carbon rich asteroids with appreciable water content and some organic molecules. This group comprises about 75% of all asteroids; they are most numerous in the outer main belt (Gradie et al. 1989). The S-group contains siliceous asteroids, and makes up 17% of asteroids. The third is the M-group, including generally metal-rich asteroids, but also objects with different compositions. Table 2.1 (modified from Britt, 2014; SBAG, 2014) presents the general relationship between different known asteroid types and their representative meteorite analogues. The majority of work on hydrated asteroids has focused on the C-type which have low albedos (proportion of incident light reflected by a surface) and are generally associated with carbonaceous chondrite meteorites. Most of the largest bodies in the main asteroid belt are of this type including Ceres, Pallas, Hygiea, Interamnia, and Europa.

Table 2.1. Relationships of Asteroid Types, Meteorite Analogs and Expected Resources. (Modified from Britt, 2014; SBAG 2014).

Asteroid Type	**Meteorite Analog**	**Major Surface Mineral**	**Expected Resources**
C (carbonaceous)	Carbonaceous chondrites (CI, CM, CV, CO)	Phyllosilicates/clays, Organics	Water, CO_2, simple hydrocarbons
M (metal)	Irons (enstatite chondrite)	Metal, Enstatite	Fe, Ni-Pt group metals
S (stony)	Ordinary chondrites, Pallasites, Mesosiderites	Olivine, Pyroxene, Metal	Oxides, Oxygen, Metals

The surface composition of an asteroid is presently evaluated by a comparison of the surface reflectance of sunlight from the asteroids with laboratory spectra of known terrestrial minerals and meteorites. Comparisons of reflectance spectra in the 3 um region has been challenging because meteorite spectra have usually been acquired under ambient terrestrial conditions with attendant interference from atmospheric water but advances in laboratory spectroscopy has allowed for spectra to be collected from samples at elevated temperatures and/or in vacuum to remove terrestrial water (Rivkin et al., 2014). The CI (named after type member the Ivuna meteorite) and CM (named after type member the Meghei meteorite) carbonaceous chondrite meteorites are widely thought to be possible analogs for dark and primitive (undifferentiated) C-type asteroids and offer some 'ground truth' for the composition of the most likely asteroidal source of volatiles. These meteorite groups experienced varying degrees of aqueous (fluid assisted) alteration on their parent bodies evidenced by the presence of aqueously altered material revealed by spectroscopic, mineralogic, oxygen and hydrogen isotopic and textural analyses (Takir et al., 2013: Hiroi et al., 1996: Beck et al., 2010: Zolensky et al., 1993: Clayton and Mayeda., 1999). The primary manifestation of aqueous alteration is the production of phyllosilicates (all phyllosilicate minerals are hydrated with either water or hydroxyl groups attached) from reactions between water and anhydrous components, more aqueously altered bodies therefore possess a higher degree of hydration. MacSween (1979b) demonstrated that more advanced alteration is associated with more Mg-rich matrices and serpentine compositions. Many of the C-type asteroids equally show hydration features indicating that they may be valuable sources of mineralogically bound water (Lebofsky et al. 1990). Hence, laboratory analyses of carbonaceous chondrites combined with astronomical observations of hydrated

asteroids has yielded important clues regarding the abundance and distribution of H_2O in the solar system.

Takir et al., (2013) identified 3 spectral groups of CM chondrites (plus the CI chondrite Ivuna), using the 3-um band center and shape of the Infrared (IR) reflectance spectra (Figure 2.7).

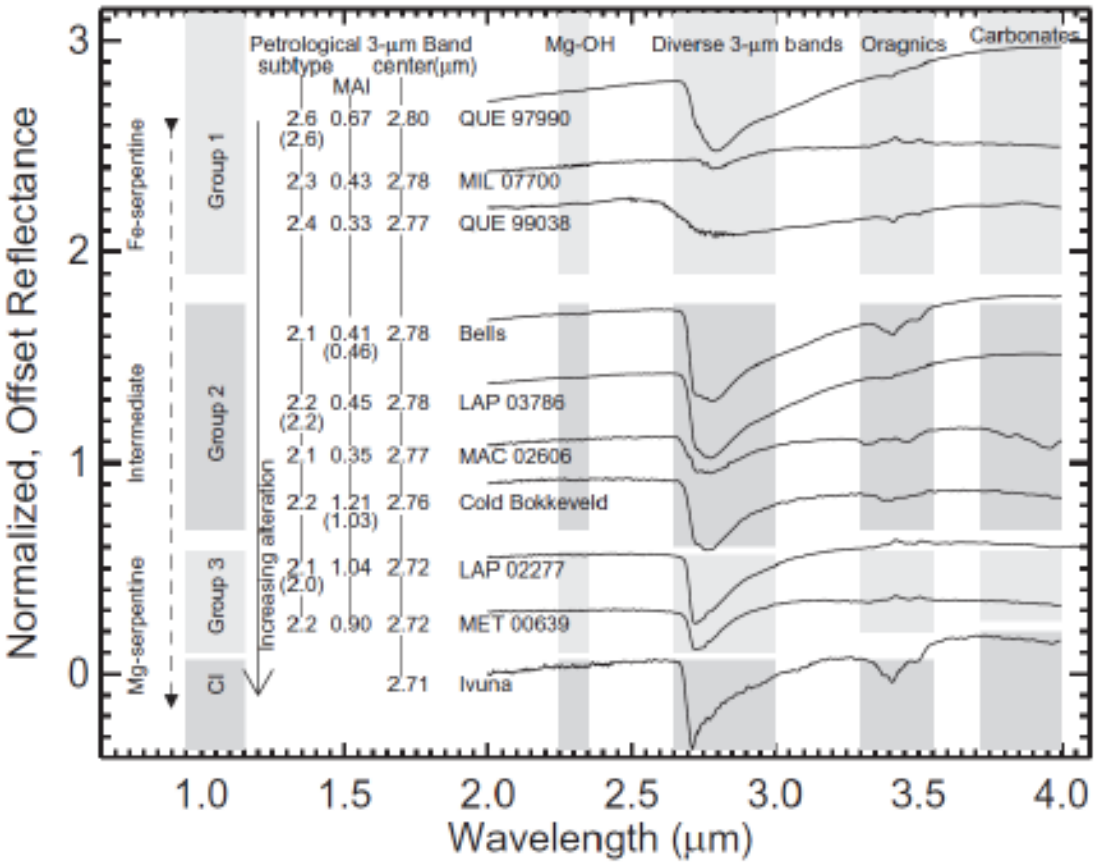

Figure 2.7. IR Reflectance Spectra of CM and CI Carbonaceous Chondrites. Measured Under Dry and Vacuum Conditions. (Takir et al. 2013).

Group 1 is consistent with the occurrence of Fe-rich serpentine (cronstedtite) and shows the lowest degree of aqueous alteration. Group 3 exhibits the highest degree of aqueous alteration and is consistent with the occurrence of Mg-rich serpentine (antigorite).

The third group is intermediate in terms of degree of aqueous alteration and is likely to contain both types of serpentine minerals. Ivuna was found to have a spectrum consistent with the occurrence of the other Mg-rich serpentine minerals (lizardite and chrysotile).

Takir and Emery (2012) identified four 3-um spectral groups using high-quality near-infrared (0.7-4.0 um) spectra of 35 main belt asteroids, each of these groups is thought to have a distinct surface mineralogy (Figure 2.8). Table 2.2 (Rivkin et., 2015) shows these groups (named after a type member asteroid), examples of each, alternate names, and compositional interpretation.

Table 2.2. Main Groupings in the 3-μm Region. Defined by Takir et al. (2012) and Rivkin et al. (2012), with type examples and possible compositions for each group (Rivkin et al., 2015).

Example body	Takir class	Rivkin class	Interpretation
511 Davida	Sharp	Pallas	CM-like phyllosilicates
24 Themis	Rounded	Themis	Water ice frost, organics
52 Europa	Europa	Themis	Water ice frost, organics
1 Ceres	Ceres	Ceres	Brucite, carbonates
21 Lutetia	--	Lutetia	Goethite?

The sharp group (pallas types) exhibits a sharp 3-um feature attributed to OH-stretching in hydrated minerals (e.g. phyllosilicates) (Rivkin et al., 2002b). The second group, the rounded group (Themis types), exhibits a rounded 3-um band attributed to the

presence of water-ice (Rivkin and Emery, 2010, Campins et al., 2010). The third group (Ceres-like) is characterized by a narrow 3-um band center consistent with brucite (Milliken and Rivkin et al., 2009). The fourth group, the 52 Europa-like group (grouped into the Themis types by Rivkin et al) exhibits a 3-um band centered around 3.15 um with longer wavelength band minimum and steeper rise on the long-wavelenght edge of the absorption. On the basis of the 3-um band shape and center, Takir et al., (2015) found that the sharp asteroids (pallas types) possibly have a similar phyllosilicate mineralogy as the CM group 2 and the CI meteorite Ivuna, suggesting that CM and CI chondrites are possibly the meteorite analogs for the sharp group (Figure 2.9).

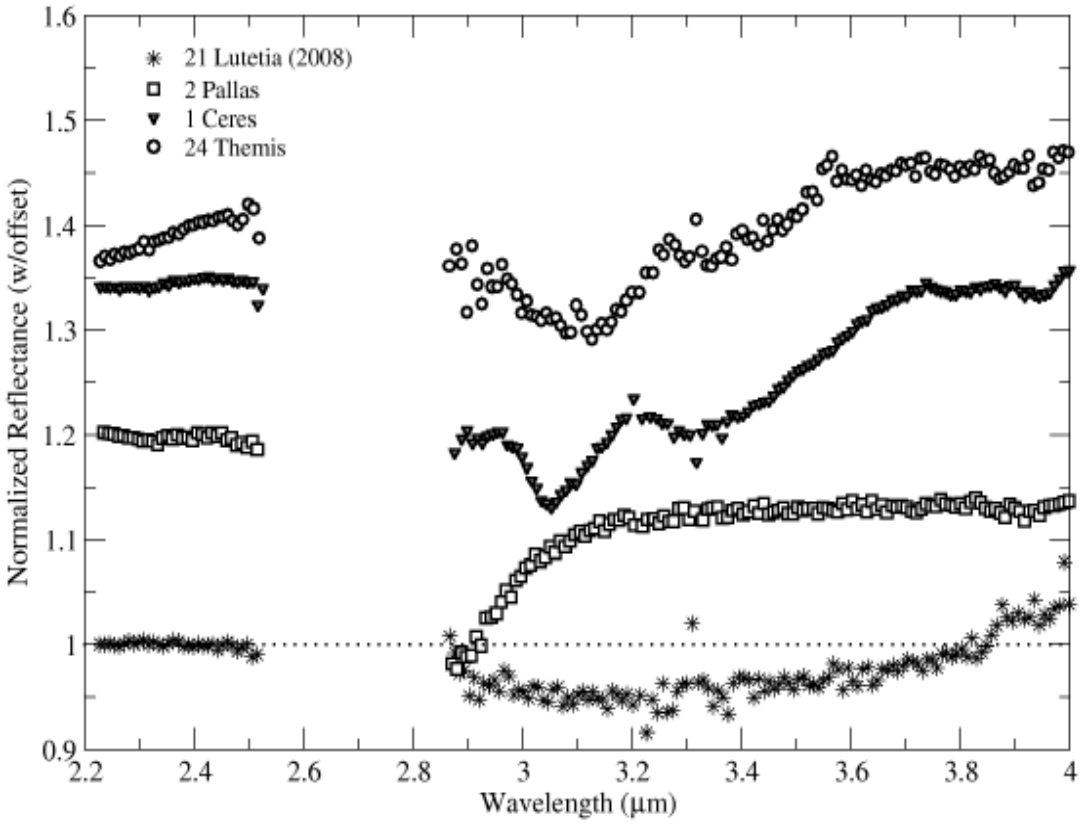

Figure 2.8. The Compositional Diversity of Asteroids in the 3-μm Spectral Region. Rivkin et al. (2011).

Near-Earth Asteroids (NEAs) are derived from the main belt but the populations are not exact mirrors of one another. Observations of NEAs in the 3-um region have been rare with the vast majority of objects too faint to observe (Rivkin et al., 2015). Absorptions have been found on 1992 UY4 (Volquardsen et al., 2007) similar to the Ceres or Themis type though observational uncertainties do not rule out a Pallas-type spectrum.

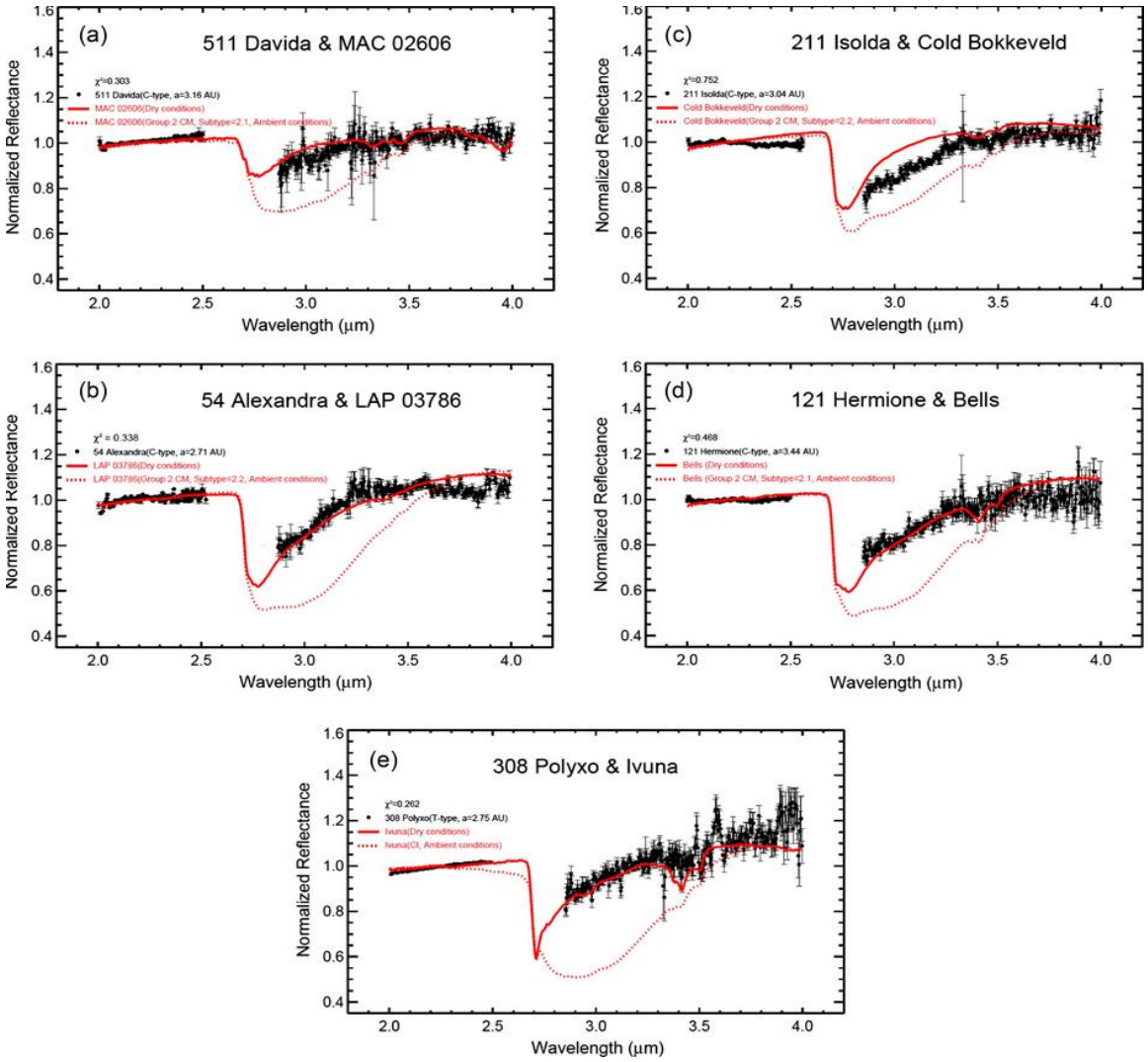

Figure. 2.9. Comparison between Some CMs and the CI Ivuna. With Some Sharp/Pallas Spectral Group Asteroids in the 3-um Region. While Asteroid Spectra have been Poor Matches for Meteorite Spectra Taken in Ambient Conditions (Dotted Red Line), Meteorite Spectra with Terrestrial Water Removed (Solid Red Line) are Much Better Matches. Figure from Takir et al. (2015).

2.2.2. Physical Nature. Starting with the Galileo flyby of asteroids (951) Gaspra (Figure 2.10a) and (243) Ida (Figure 2.10.b) on its way to Jupiter, spacecraft investigations of asteroids have provided validation for ground-based spectroscopic studies. Some of the other asteroids visited include 253 Mathilde in 1997 by the first dedicated asteroid probe NEAR Shoemaker which landed on 433 Eros in 2001, 21 Lutetia in 2010 and 2867 Steins in 2008 by the European Rosetta probe amongst others. These visits have allowed for more accurate measurements of asteroid properties such as size, density, composition, shape, surface morphology, mass, porosity etc. More recently, the Japanese Hayabusa and NASA's Dawn missions have completed detailed studies of asteroids (25143) Itokawa and (4) Vesta respectively from orbit. A sample of the near-Earth asteroid Itokawa was returned and 2 more sample return missions are ongoing targeting primitive carbonaceous asteroids. Hayabusa-2 will return a sample from (162173) 1999 JU3 while OSIRIS-Rex will return a sample from Bennu. Planetary radar astronomy is an active form of observation that also aids in investigating the physical properties of solar system bodies.

The Near-Earth asteroid Itokawa is spectrally classified as an S-type body with a surface mineralogy composed of silicates (pyroxene and olivine) and Iron (Fe) (Binzel et al., (2001). The Hayabusa spacecraft successfully collected data on its shape, mass and surface topography estimating a mass of 3.51×10^{10} kilograms and a bulk density of about 1.9 g/cm^3 (Fujiwara et al., 2006). The surface of Itokawa is divided into a rough terrain, mostly consisting of numerous boulders and a smooth terrain (Muses Sea separating 2 distinct parts and the Sagamihara located around the north-polar region), Figure 2.11(a) shows an image of Itokawa taken at 7-km altitude. This is unlike Eros which was reported to be mostly covered by a thick regolith layer (Chapman et al., 2002). The smooth region

was found to be composed of fragmental debris with grain sizes of cm to mm scales from close up images (Yano et al., 2006). Abe et al., (2006) and Okada et al., (2006) reported homogeneity in mineralogical composition over the entire body in spite of its bifurcated nature.

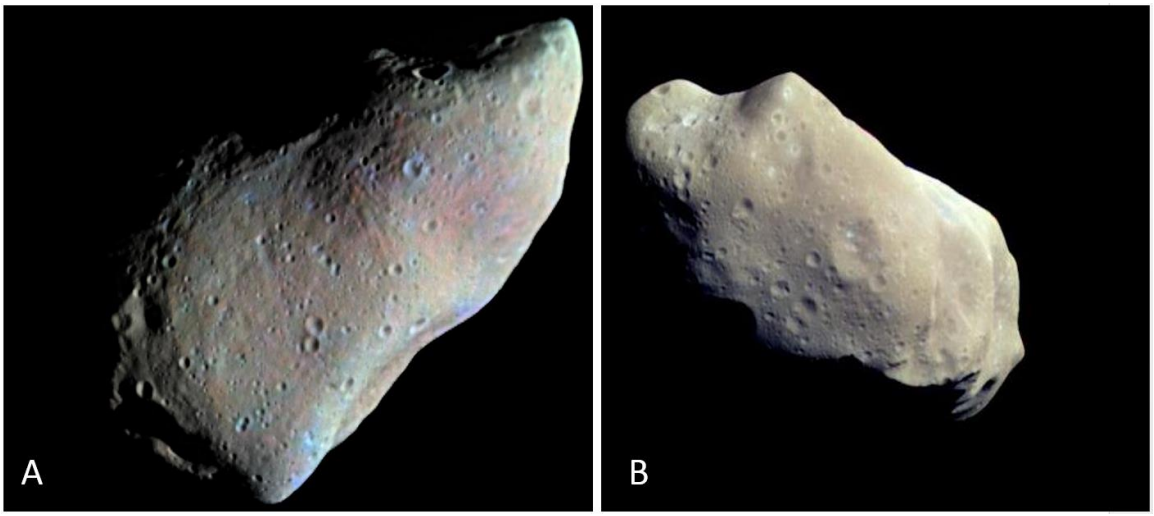

Figure 2.10. Enhanced Color Imagery from Galileo Flyby. a) 951 Gaspra b) Ida.

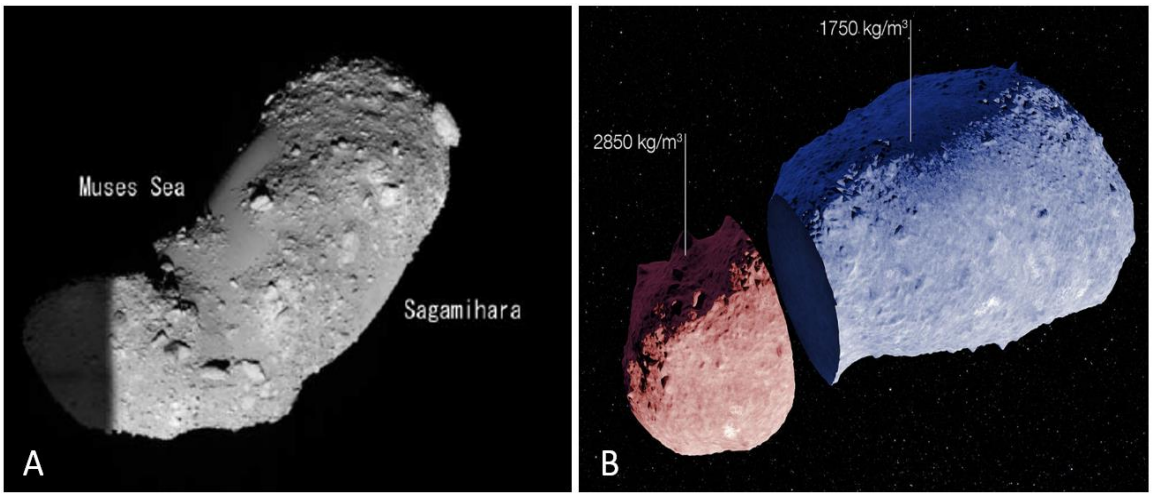

Figure 2.11. Image of Itokawa. A) Taken by Hayabusa at 7-km Altitude. B) Diagram Showing Average Density of Two Lobes. (JAXA) (Densities from S.C Lowry et al., 2014).

The smooth regions had near zero slopes and are considered to be energetically relaxed which is thought to have allowed the migration and accumulation of loose, smooth granular material through secondary movement of grains on the surface (Fujiwara et al. 2006). Itokawa's bulk density is significantly lower than the ~2.6 g/cm3 determined for other S-type asteroids with well determined bulk densities (Thomas et al., 2001) suggesting a macroporosity on the order of 41% (Fujiwara et al., 2006), a value substantially higher than the average value of ~30% for s-type asteroid including Eros. This is suggestive of considerable void space within its interior, terrestrially, materials with porosities larger than 30% are usually considered loose soils or rubble (Britt et al., 2002). Based on the lack of conspicuous linear structures extending over its length like the ridge on Eros (Ververka et al., 1997), coupled with the existence of multiple local facets with scales of several tens of meters, Fujiwara et al., postulated that Itokawa is not a single consolidated, coherent body but rather an aggregate of rubble (Figure 2.12) with sizes ranging up to about 50 meters. These authors suggested that if Itokawa was once a coherent body, it might have experienced collisional disruption followed by re-agglomeration, meaning that this asteroid could either be a 'young' object or a loosely consolidated body or both. Landslide-like deposits were also observed (Demura et al., 2006) in a region with slopes in excess of 35^0. Few asteroids of a similar size or larger than Itokawa are fast rotators and this evidence has been used to argue that most asteroids larger than about 150 meters may be rubble piles (Whitely at al., 2002). Radar imaging has revealed more than 30 NEAs that are deeply bifurcated (Benner et al., 2006; Brozovic et al., 2010; Magri et al., 2011). The fraction of candidate contact binaries (defined as obviously bifurcated objects that possess components that can be significantly different in size, and mass distributions that aren't

bimodal) imaged by radar stands at ~14% (Taylor et al., 2012). Scheeres and Gaskell 2008) suggested that the two parts of the Itokawa defined in Demura et al. (2006) as the head and body components may have different densities (see Figure 2.11b). This was motivated by the NEA contact binary asteroid 199 KW4 which was reported (Ostro et al., 2006) to have a 40% disparity between its primary and secondary parts. Scheeres and Gaskell suggested a head density of 2.20g/cm^3 and a body density of 1.83 g/cm^3 from approximate calculations. Regolith samples returned from the surface of 25143 Itokawa were found to be highly poly-disperse, with grain sizes ranging from micro- to millimeter scales (Tsuchiyama et al. 2011). Other asteroids such as Eros (Veverka 2000, Robinson et al. 2002, Li et al. 2004) are thought to have solid cores with a surface regolith composed of a granular material.

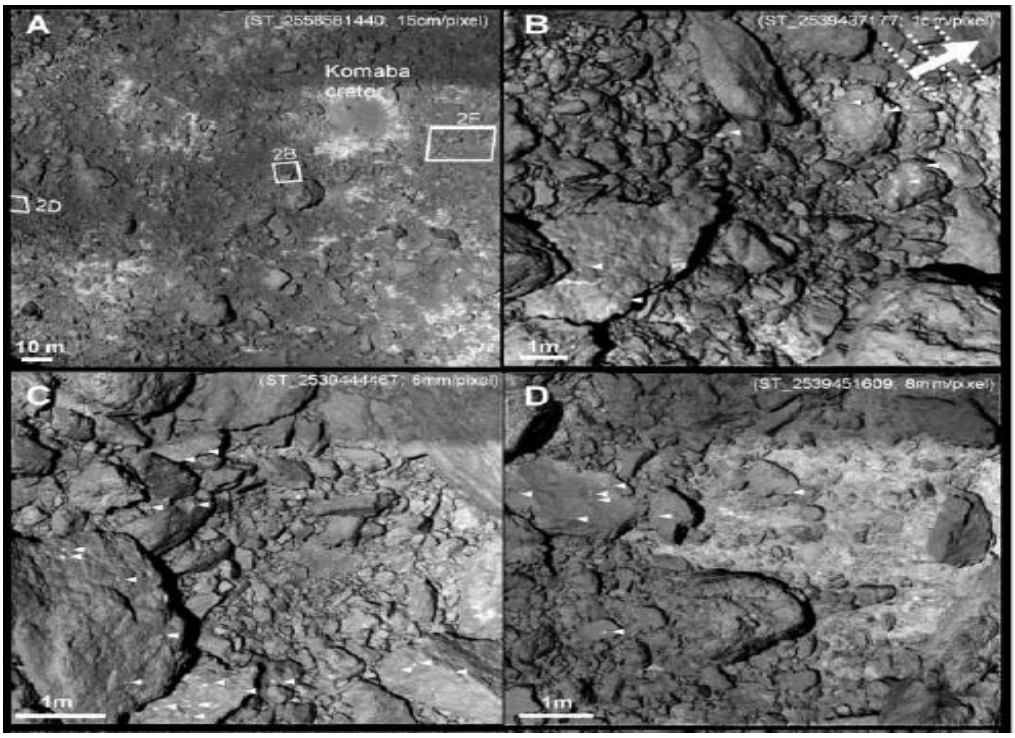

Figure 2.12. Close-Up Images of the Rubble-Pile Asteroid Itokawa. (Miyamoto et al. 2006).

Chesley et al., (2014) used radar astrometry and optical astrometry to calculate estimates of the mass and bulk density of the asteroid Bennu. The estimated density of 1.3 kg/m^3 implies a macroporosity of ~40% suggesting a rubble-pile internal structure. Raw radar imagery show that Bennu is roughly spheroidal (Figure 2.13) with some large scale but fairly subtle features (Nolan et al., 2013). The asteroid has a fairly smooth "spinning top" shape similar to that of binary asteroids such as 1999 KW4 (Ostro et al., 2006) and other "speherioidal" asteroids such as 2008 EV5 (Busch et al., 2011), but with a less well-defined equatorial ridge. The shape appears fairly smooth at small scales, with some large-scale features. There is one 10-20 m boulder on the surface that appears in both 1999 and 2005 radar images, but no other small-scale surface features are evident down to the radar resolution of 7.5 m (Nolan et al).

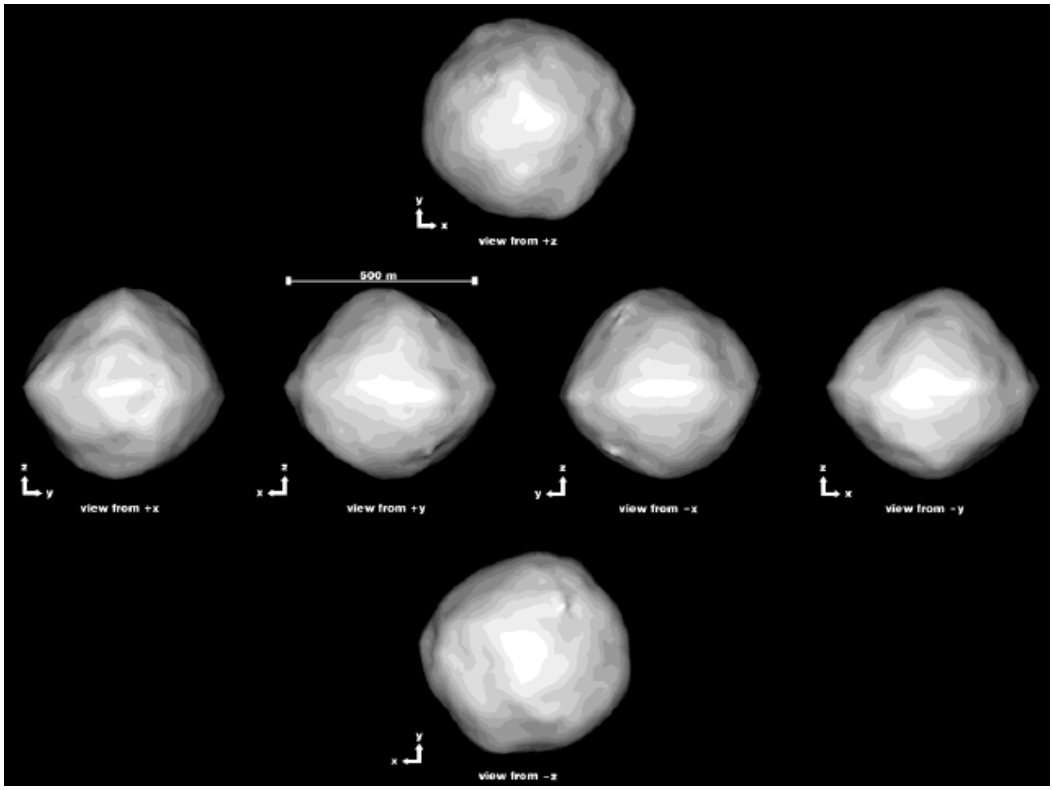

Figure 2.13. The Shape of Bennu. (Nolan et al. 2013).

The strength of a rubble-pile body will control how fast it can rotate before breaking apart or loosing mass, influence the process by which binary asteroids are created (Sanchez and Scheeres, 2014). Current theories on strength and morphology of these bodies are largely motivated by simple interpretations of their size/spin rate curves. Pravec and Harris (2000) theorized that all bodies spinning at rates beyond the surface disruption spin period (defined as the spin period at which gravitational attraction is overcome by centripetal acceleration at the surface of a rapidly spinning spherical asteroid) of approximately 2.3 hours were coherent bodies or monoliths. This theory suggests that rubble piles will disaggregate if spun beyond this limit presupposing a lack of cohesive strength beyond their components. Holsapple (2007) investigated the relationship between the deformation of a rubble-pile body and its spin rate and showed that the level of cohesive strength necessary to keep the known fast spinning asteroids bound together is modest and corresponds to relatively weak rock. Britt et al., (2002) presented a model to explain the high porosities observed in rubble-pile bodies where they suggest that the interior consists mainly of large boulders with finer gravels trapped at the surface. Other descriptive models presented include those by Asphaug et al., (2001) and Miyamoto et al., 2007). Sanchez and Scheeres (2014) tested an analytical model based on a view of a rubble-pile body where interstitial grains of finer size play an important role as a cement in holding larger boulders and grains together allowing it to spin more rapidly than the surface disruption limit, they develop a model for an asteroid strength and use it to provide a theoretical link between cohesive strength and failure. They also show that the strength of such a matrix is inversely dependent on the mean grain size within the cohesive matrix and show the consistency of their model with a cohesive strength in rubble-pile asteroids on the order of 25 Pa.

G.J. Consolmagno et al., (2008) investigated the porosity, grain density and bulk density of meteorites in the meteoritic collection and used the information derived to estimate the bulk porosity of asteroids and assess their internal structure. They posited that any deviation of an asteroid's bulk density from its meteorite analog's grain density provides an estimate of the bulk porosity of an asteroid. That bulk porosity has two components: the microporosity of the asteroidal material which was assumed by the authors to be the same as the porosity of the meteorite analog, and the macroporosity of large-scale voids within the asteroid itself. In this method, macroporosity represents void spaces whose dimensions are on the order of the dimensions of the analog meteorites themselves or larger as opposed to microporosity which equals the porosity measured within the meteorites themselves. Parallel grooves seen in images of Phobos and the body-wide faults of Eros were put forward as possible hints to the way macroporosity could be expressed within an asteroid. These authors noted four trends in their estimates presented in Figure 2.14: First, the largest asteroids (with masses greater than 1020 kg) all have essentially zero macroporosity. Second, virtually all asteroids smaller than that mass have at least 20% or more macroporosity. Third, with exceptions, there is a general trend where the roughly 20% macroporous bodies tend to be S-type asteroids, while the much more macroporous bodies tend to be C-types and finally, the icy bodies of the outer solar system-the comets, centaurs, and Trans-Neptunian Objects (TNOs) are extremely macroporous. Note that this analysis is strongly dependent on 2 assumptions: First, an accurate knowledge of an asteroid appropriate meteorite analog and second, on the similarity between the meteorite and its asteroid parent body after its removal and delivery to the Earth.

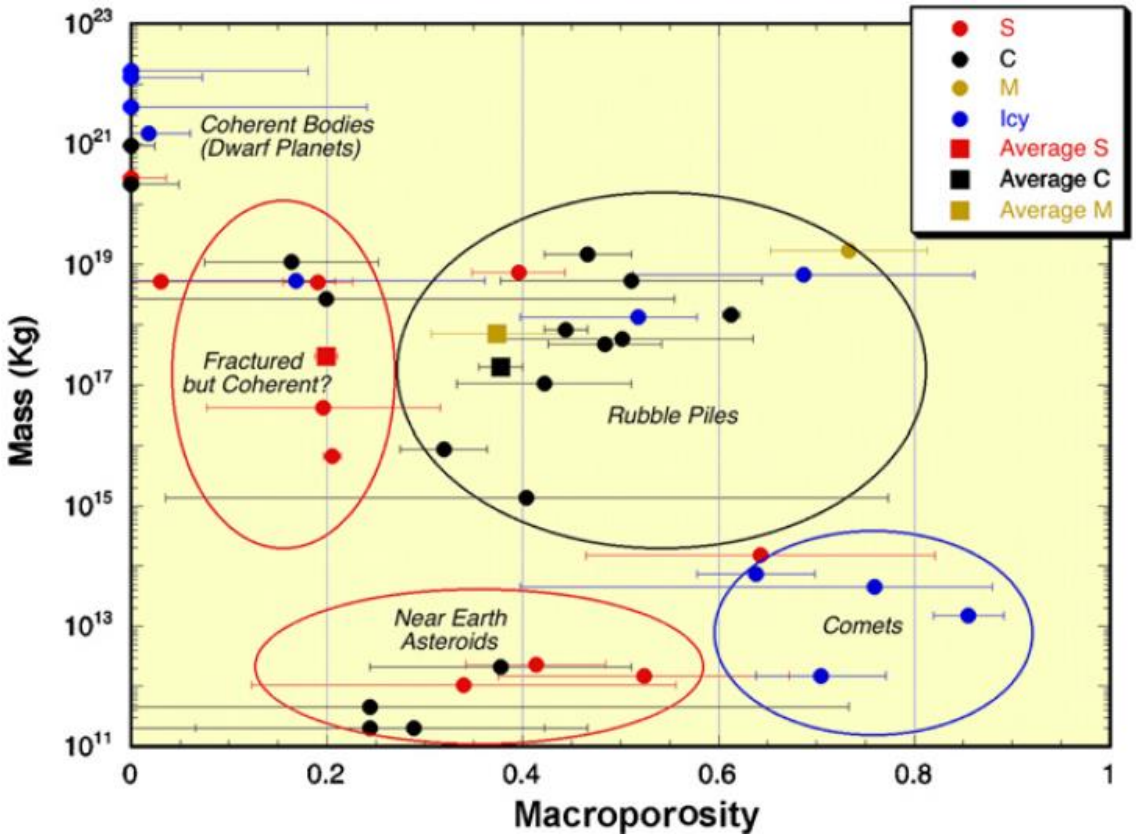

Figure 2.14. Estimated Macroporosity for a Range of Solar System Bodies. Adapted by G.J. Consolmagno et al. (2008) from Britt et al. (2002).

Figure 2.15 (from G.J. Consolmagno et al) presents a plot of the macroporosities of the asteroids measured as a function of their position in the asteroid belt, note a general trend of higher macroporosities to be found in bodies further out in the belt and further away from the Sun. The idea of a chemically zoned solar nebula controlled by proximity to the Sun was first discussed by Urey (1952) and Lewis (1974). Gradie and Tedesco, (1982) did an analysis of the asteroid spectral classes vs. their orbital locations and showed a distinct gradation of material types within the asteroid belt as a function of their distance from the sun: the high-moderate temperature silicate minerals dominate the inner solar system at heliocentric distances of less than ~2.5 AU, while lower-temperature carbonaceous minerals are common in the cooler, outer regions of the solar system beyond

2.5 AU. This boundary apparently marks the location where cooling temperatures allowed for the formation of carbon compounds. At about 3.5 AU, the nebula was cool enough to allow the formation of water-ice. A solar nebula was envisioned by G.J. Consolmagno et al where distance from the sun not only controls the composition of the material but also its physical nature.

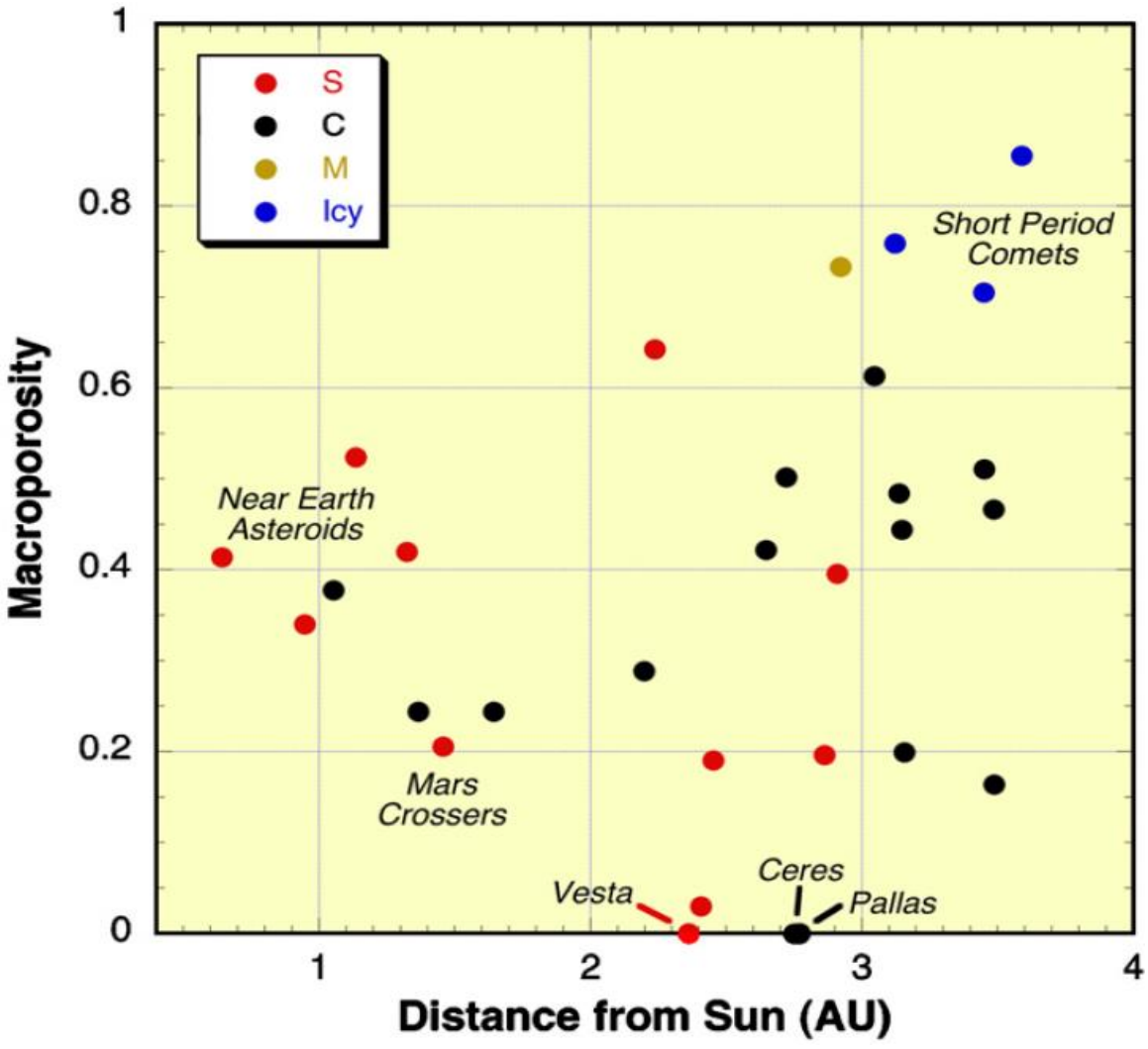

Figure 2.15. Macroporosity of Asteroids as a Function of Their Location. In the Asteroid Belt. G.J. Consolmagno et al. (2008).

2.3. THERMAL PROCESSING AND MINERAL SOURCE OF VOLATILES

Hydrated carbonaceous chondrite meteorites (primarily CIs and CMs) contain numerous phases of phyllosilicates, organic matter, carbonates and sulphates, all of which are capable of producing volatile gases of different compositions upon thermal degradation. Phyllosilicates comprise as much as 70 wt. % of some chondritic meteorites (Bland et al., 2004). Sources of water are hydroxyl groups bound within the phyllosilicate mineral structure and molecular water trapped between phyllosilicate sheets. In CM chondrites, most phyllosilicates belong to the serpentine group, with a typical formula of $(Mg,Fe)_3Si_2O_5(OH)_4$. Fe-rich serpentine phases are generally referred to as Fe-cronstedtite, while the more magnesian members are cited as Mg-serpentine (Howard et al., 2009). In CI chondrites, pervasive aqueous alteration has resulted in the formation of abundant saponite $(Mg,Fe)_3Si_4O_{10}(OH)_2\_4H_2O$, intergrown with serpentine and ferrihydrite $(Fe^{3+}{}_2O_3\_0.5(H_2O))$. The behavior of these phases at elevated temperatures is summarized in Table 2.3 (modified from Court and Sephton, 2014).

Heating saponite in air causes dehydration and loss of interlayer water around 400^0C–600^0C, followed by the decomposition and the loss of bound hydroxyl groups around 700^0C–800^0C (Brindley and Hayami, 1965; Akai, 1992; Greshake et al., 1998; Nozaki et al., 2006). Serpentine, lacking the interlayer water of saponite, produces water only upon decomposition, which occurs around 400^0C–500^0C for Fe-cronstedtite (Mackenzie and Berezowski, 1981) and around 500^0C–600^0C for Mg-serpentine (Brindley and Zussman, 1957; Brindley and Hayami, 1965; Akai, 1992; Greshake et al., 1998; Nozaki et al., 2006)

Table 2.3. Temperature of Decomposition of Volatile-Generating Phases Identified in Carbonaceous Chondrites. (Modified from Court and Sephton, 2014).

Phase	Reaction	Volatile Evolved	Approximate Temperature of Evolution (^{0}C)
Adsorbed Water	Desorption/Dehydration	H_2O	<300
Ferrihydrite	Dehydration/Decomposition	H_2O	100-200, 500-600
Mg-Serpentine	Decomposition	H_2O	400-600
Saponite	Dehydration/Decomposition	H_2O	400-600, 700-800
Gypsum	Dehydration/Decomposition	H_2O, SO_2	<200, 1200
Epsomite	Dehydration/Decomposition	H_2O, SO_2	310, 1100
Ni-Blodite	Dehydration/Decomposition	H_2O, SO_2	260
Tochilinite	Dehydration/Decomposition	H_2O, SO_2	<400, 400-600
Breunnerite	Decomposition	CO_2	400-650
Dolomite	Decomposition	CO_2	700
Calcite/Aragonite	Decomposition	CO_2	890
Sulphur	Oxidation	SO_2	<200
Sulphides	Oxidation	SO_2	400-600
Intermolecular Organic Matter (IOM)	Oxidation	H_2O, CO_2, SO_2	_

Hydrated sulphates are also a potent source of water. Sulphates are most abundant in CI chondrite meteorites, with reports of total abundances ranging from around 2 wt.% to up to 15wt.% (Burgess et al., 1991; Gao and Thiemens, 1993), occurring in the Orgueil meteorite (CI) as phases such as gypsum ($CaSO_4$_$2H_2O$), Ni-blodite (Na,Mg,Ni)$(SO_4)_2$_$2H_2O$ and epsomite $MgSO_4$_ $7H_2O$ (Bostrom and Fredriksson, 1966; Fredriksson and Kerridge, 1988; Burgess et al., 1991; Gounelle and Zolensky, 2001; Bullock et al., 2005). The water of hydration (water chemically combined with a substance to form a hydrate and can be expelled at relatively low temperatures without altering the composition of the substance) in sulphates is readily released at relatively low temperatures. For

example, dehydration of gypsum to anhydrous calcium sulphate ($CaSO_4$) occurs around 180^0C, while epsomite loses water progressively starting at very low temperatures until complete dehydration around 310^0C (Paulik et al., 1981).

Discerning the decomposition temperatures of the sulphur-bearing phases on the other hand is challenging. Sulphides lack the necessary oxygen within their chemical compositions to evolve sulphur dioxide upon thermal decomposition in a fashion analogous to that of water from phyllosilicates, instead requiring an external source of oxygen. Furthermore, the chemistry of sulphides and sulphates at high temperatures can be quite diverse (Court and Sephton, 2014).

The oxygen source required to generate sulphur dioxide from these sulphide phases is not clear, but reaction of hot sulphides with water evolving from phyllosilicates has been noted to be capable of producing elemental sulphur (Bostrom and Fredriksson, 1966), readily oxidised at these temperatures. Stoichiometry indicates that complete oxidation of the 2.1 wt. % troilite (FeS) and 4.5 wt.% pyrrhotite ($Fe_{(1-x)}S$: x=0 to 0.2) present in the Orgueil meteorite (Bland et al., 2004) could yield about 5 wt.% sulphur dioxide. This is considerably in excess of the observed production of sulphur dioxide of 3 wt.% in the 500^0C–800^0C window (Court and Sephton, 2014). The thermal stability of sulphate phases suggests that a significant proportion of sulphate could remain in the sample at 1000^0C (Burgess et al., 1991; Greshake et al., 1998).

Figure 2.16 (Court and Sephton, 2009b, 2011, 2014) presents a comparison of volatile yields from 5 carbonaceous chondrite meteorites of CI, CM, and CV-type subjected to stepped pyrolysis against yield from a single pyrolysis event at 1000^0C.

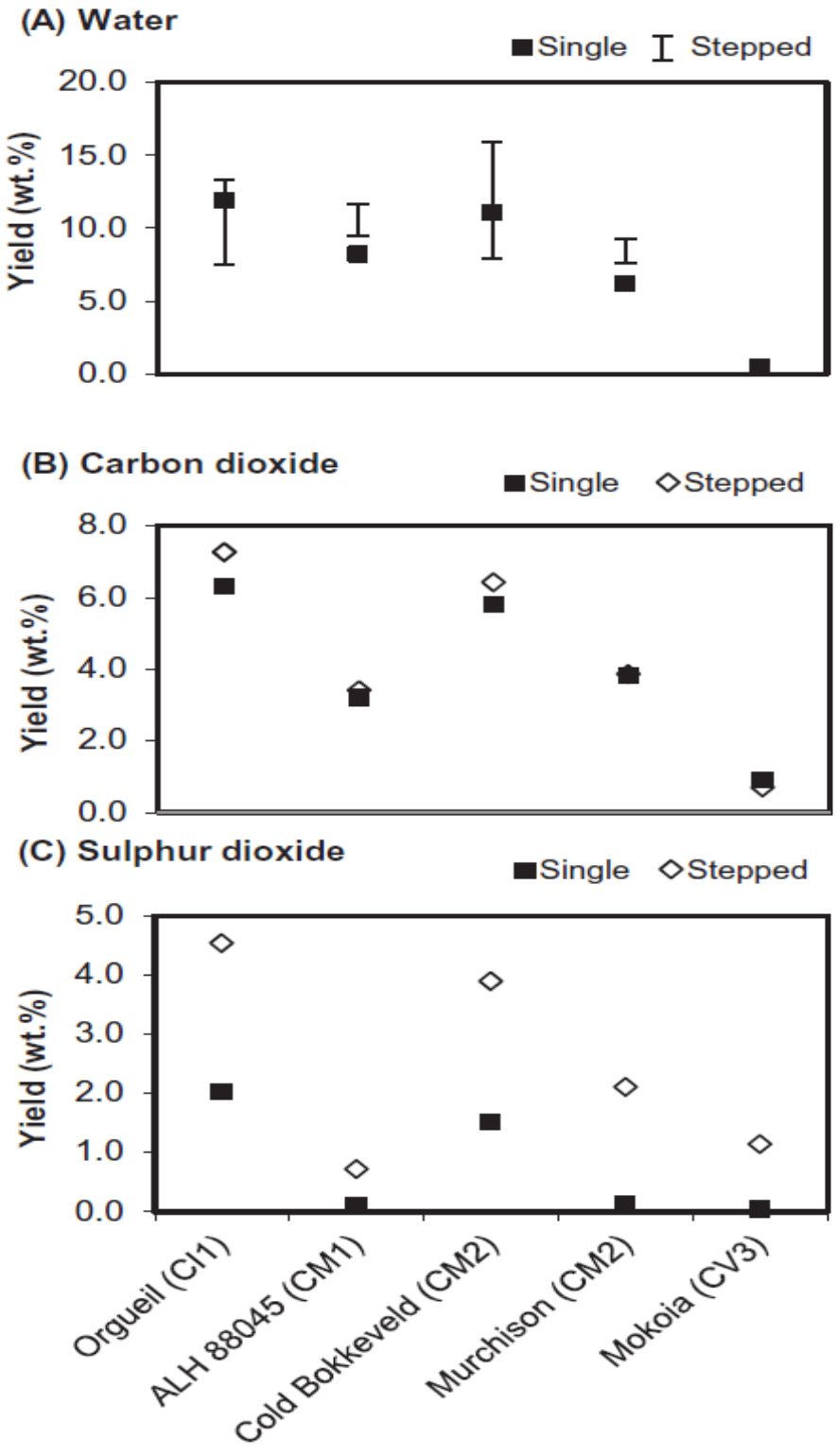

Figure 2.16. Comparison of Volatile Yields from Carbonaceous Chondrite Meteorites.

Any organic material present is capable of releasing water, carbon dioxide and sulphur dioxide. Pyrolysis of simple organic matter can produce volatiles at low temperatures, such as water from hydroxyl groups, carbon dioxide from carboxyl groups and sulphur dioxide from sulphuric acids (Court and Sephton, 2014). The other main source of carbon dioxide is carbonates, which most often occur as siderite ($FeCO_{3)}$, magnesite ($MgCO_3$), calcite and aragonite ($CaCO_3$), and dolomite ($CaMg(CO_3)_2$), frequently as solid solutions between phases. CI chondrite meteorites are generally enriched in dolomite (Fredriksson and Kerridge, 1988; Johnson and Prinz, 1993; Endress and Bischoff, 1996; Brearley and Jones, 1998), while the CM chondrites contain some calcite (Zolensky et al., 1997; Howard et al., 2009, 2011). Mg–Fe carbonate is reported to decompose in the 400^0C–650^0C temperature range, with Fe-carbonates decomposing from 400^0C and Mg-carbonate surviving until around 600^0C–650^0C (Smykatz-Kloss, 1974; Greshake et al., 1998; Nozaki et al., 2006). Dolomite is more resilient, surviving to 700^0C (Nozaki et al., 2006), while calcite is most resilient, decomposing to yield carbon dioxide around 890^0C (Smykatz-Kloss, 1974).

3. TECHNICAL APPROACH AND METHODOLOGY

3.1. TECHNICAL SETUP

The general approach of this work was to cause gas release by radiatively heating volatile-bearing materials in a vacuum environment, the released gas species were identified by a mass spectrometer and recovered as ice on the surface of the cryogenic trap. A simple way to consider this setup (Figure 3.1) is as a closed system with the furnace as the source of heat, the asteroid simulant sample as the source of volatiles and the cold trap as the sink. Key elements of this setup are considered in the next section**.**

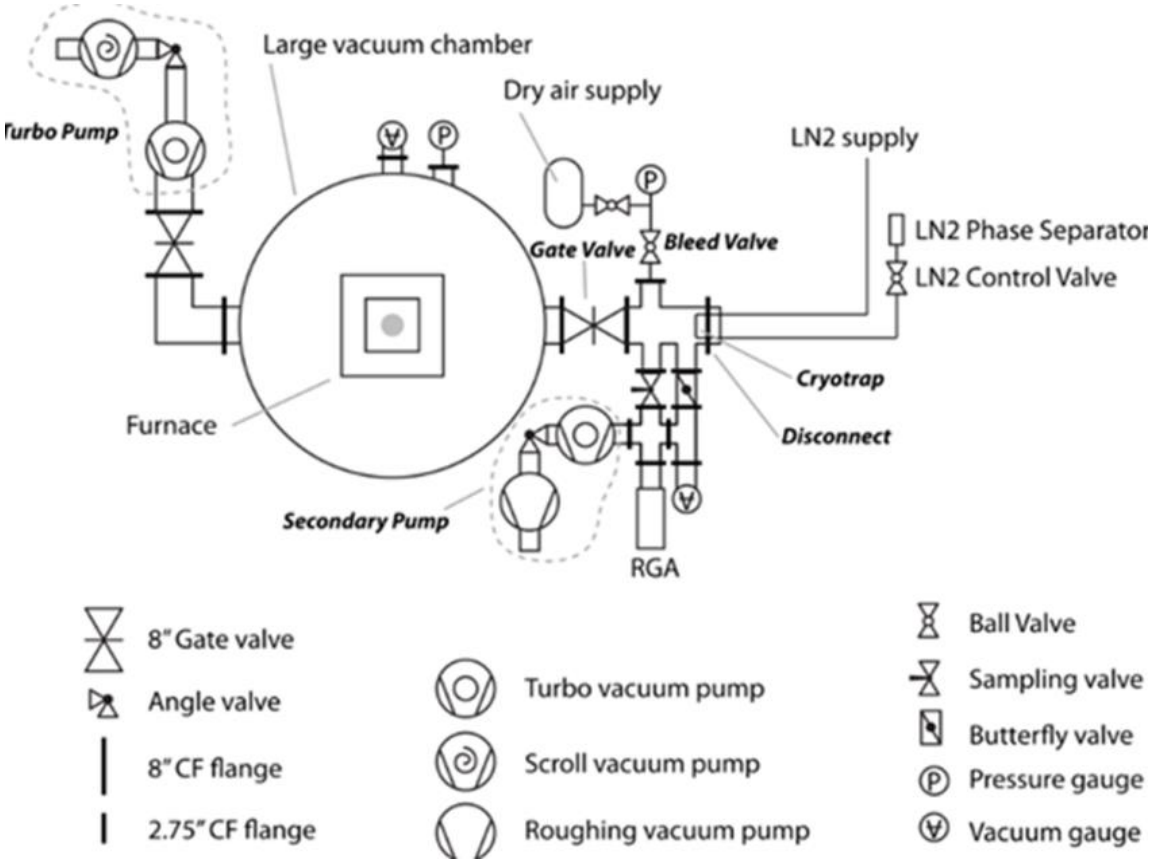

Figure 3.1. Schematic of Laboratory Vacuum-Pyrolysis System.

3.1.1. Main Vacuum Chamber. The main vacuum chamber was built by the National Aeronautics and Space Administration (NASA) to serve the Apollo missions during the period from 1963–1972; it is 1.23 m in diameter and 1.83 m in length and is made out of stainless steel. It has been maintained and housed at the Colorado School of Mines Center for Space Resources and for the purpose of this project was modified and instrumented to suit test conditions. It housed the furnace and provided the high vacuum environment within which the tests were conducted.

Figure 3.1 shows a schematic of the experimental vacuum-pyrolysis system. It consisted of the 6 m^3 main vacuum chamber (labeled large vacuum chamber) linked by a four-way cross connector to a mass spectrometer, a cold trap and a viewing window attached on each end. A furnace designed to simulate solar-thermal heating sat within the vacuum chamber providing a source of resistive-radiative heat. To run an experiment, the system was sealed and then pumped in two stages:

1. First, a roughing/oil pump was applied to reduce pressure from ambient atmosphere which typically ranged from 740-760 mmHg (torr) to low vacuum pressure (1×10^{-2} torr).
2. A turbo-molecular pump was then used to bring base pressures in system to the high vacuum range (5×10^{-7} torr).

The main vacuum chamber pictured in Figure 3.2, was wrapped on the outside by heat tape maintained at 50 ^{0}C. The objective in this instance was to maintain its walls at an elevated temperature to prevent adsorption of released moisture from sample out-gassing during the tests.

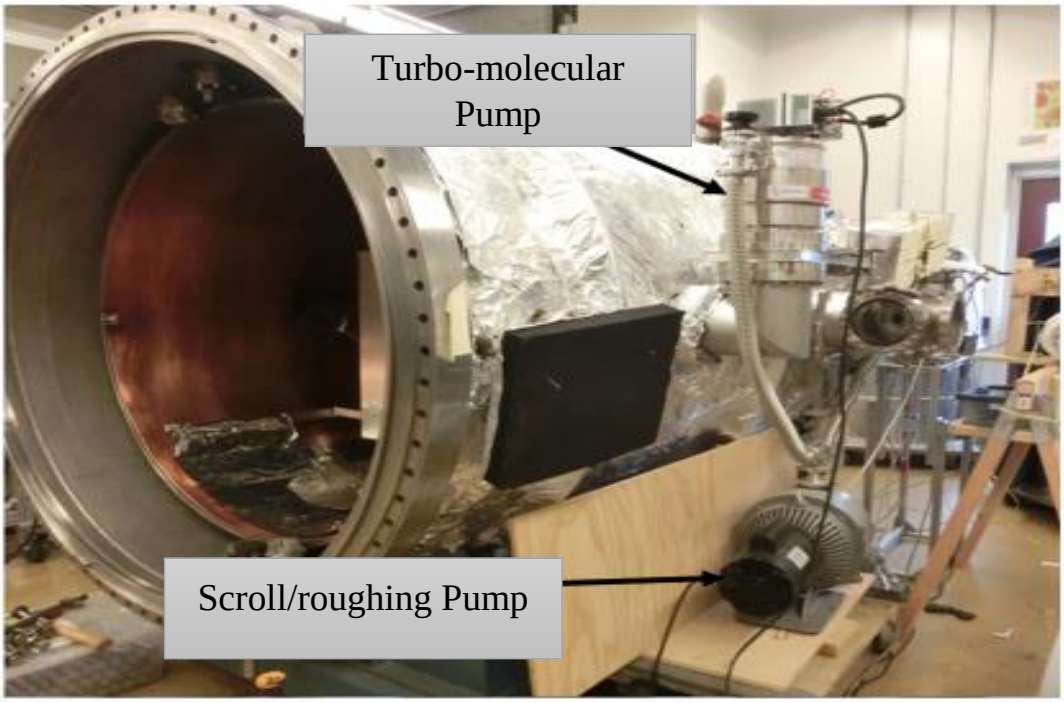

Figure 3.2. Angled-View of Vacuum-Pyrolysis System.

3.1.2. Furnace. The Paragon muffle furnace shown in Figure 3.3 was purchased and re-purposed for vacuum operation. This common type of ceramics kiln has resistive heating elements on three sides made from nichrome and was designed to reach a maximum temperature of 1300^0C in air. To ensure that the tested materials were the only source of gas, components such as the firebrick insulation and paint finish which would outgas under vacuum conditions were removed, electrical wiring was replaced with vacuum-compatible materials. Double-walled stainless steel insulation, with walls spaced 2.5 cm apart was added and the digital controller was detached and operated from outside the vacuum system. Within the vacuum chamber, the modified furnace sat on stainless steel rods and within an outer box of additional double-walled stainless steel insulation which

allowed the furnace to reach a maximum temperatures that ranged from 660^0C to 670^0C during tests.

Figure 3.3. Furnace. (Left: Original kiln model. Right: Repurposed kiln sitting in outer box of insulation).

3.1.3. Mass Spectrometer. A quadrupole mass spectrometer shown in Figure 3.4 was used for the identification of gas species present within the residual environment. The Stanford Research Systems (SRS) Residual Gas Analyzer (RGA) 200 ionizes a small fraction of the gas molecules present, it then separates, detects and measures the resulting ions according to their molecular masses or more accurately, their mass-to-charge ratio defined as the ratio of the mass number M of the ion to its charge (m/q). It was programmed to cover the range from 1 – 200 atomic mass units (amu) and operated at a rate of 1000 msec/amu producing a scan over the selected mass spectrum once every ~3 minutes. The

mass spectra produced over the course of an experiment generates data in the form of partial pressure or volume fraction of various gas species.

Figure 3.4. Quadrupole Mass Spectrometer.

3.1.4. Cold Trap. This device may be considered a variant of a cryogenic capture vacuum pump, it acts to maintain low pressure as gas molecules produced from samples being tested are immobilized on its surface through freezing action. The cryogenic trap (Figure. 3.5) was made out of 0.64 m (¼ inch) stainless steel tubing which was bent into a spiral in a manner such as to maximize the ratio of its frontal surface area to the surface area of warmer walls within the vacuum system. This ratio was found to directly affect the speed of cryo-trapping in initial testing and design. This device extended into the vacuum-pyrolysis system through a 20.3 cm (8 inch) diameter flange on one end of the four-way

cross. Its exterior lines were carefully insulated to limit temperature loss and conserve coolant use.

To operate this apparatus, liquid nitrogen (LN_2) coolant from a pressurized 230-liter cylinder was actively passed through the stainless steel tubes. Flow was modulated by use of an Arduino controller that utilized a K-type thermocouple reading temperature at a flow outlet to maintain desired temperatures. This automated control mechanism used a valve at this outlet to increase or impede flow (see schematic in Figure 3.6).

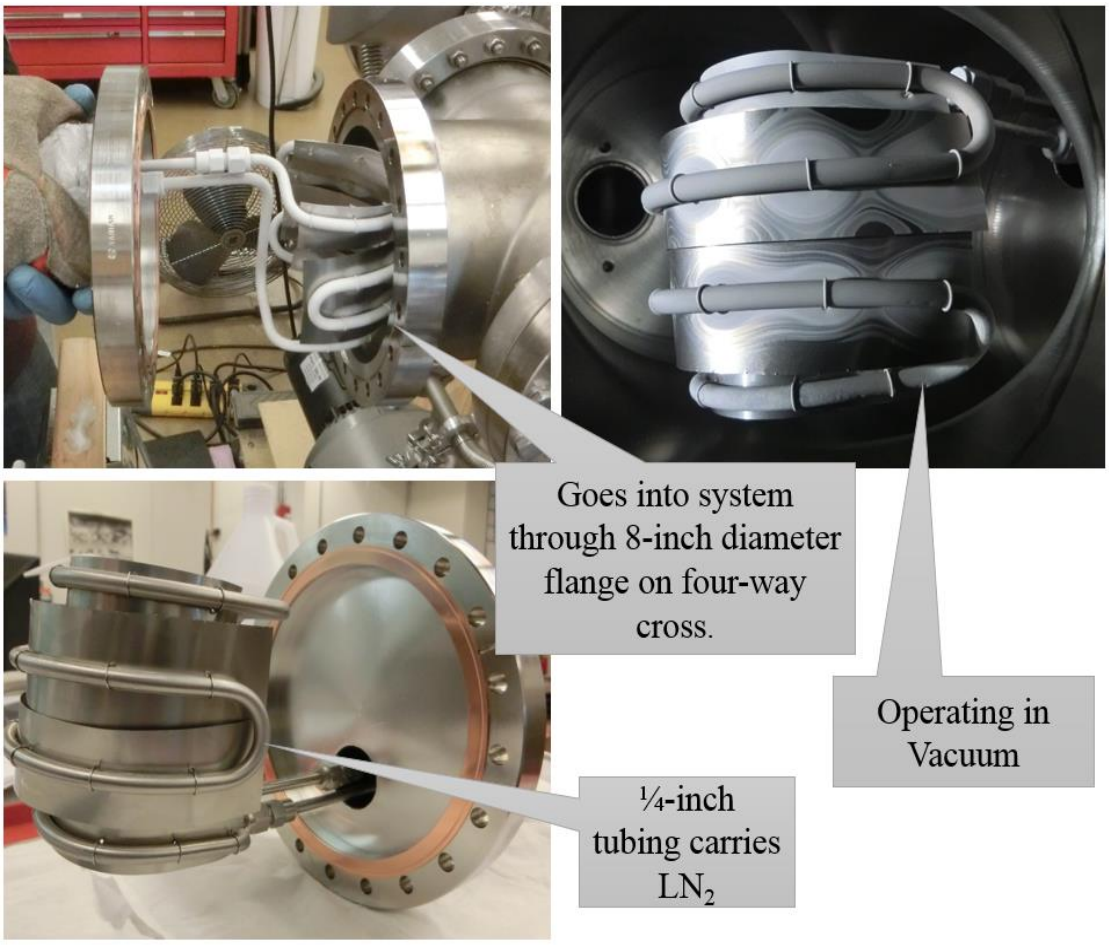

Figure 3.5. LN_2 Cooled Cold Trap.

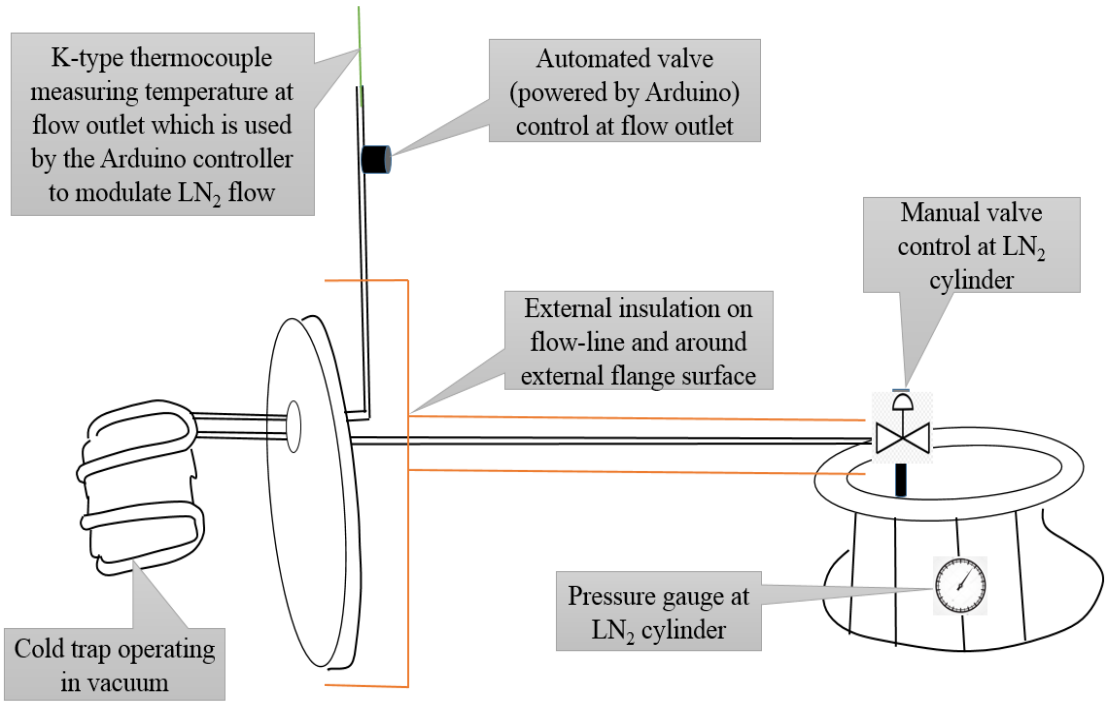

Figure 3.6. Schematic of Cooling System Setup.

3.1.5. Sensors. Pressure within the system was measured by Inficon inverted magnetron pirani gauges (MPG 400). Two were used with one measuring the pressure of the main vacuum-pyrolysis system while the other was used to monitor pressure at the mass spectrometer. These pressure gauges were designed for vacuum measurements in the range of 3.7×10^{-9} – 750 torr and were mounted on ~7 cm (2.75 inch) diameter flanges. They are ±30% accurate in the operating range from 7.5×10^{-9} – 75 torr and were also designed to operate optimally in the temperature range of 5^0C to 55^0C. Gauges of this kind consist of two separate measuring systems (Pirani and cold cathode system) which are combined in such a way that they behave as a single measuring system. The optimum measuring configuration for the pressure range, in which measurement was performed was used. The

Pirani measuring circuit is always on but the cold cathode circuit is only activated at pressures $<7.5 \times 10^{-3}$ torr. Figure 3.7 shows the location of both gauges.

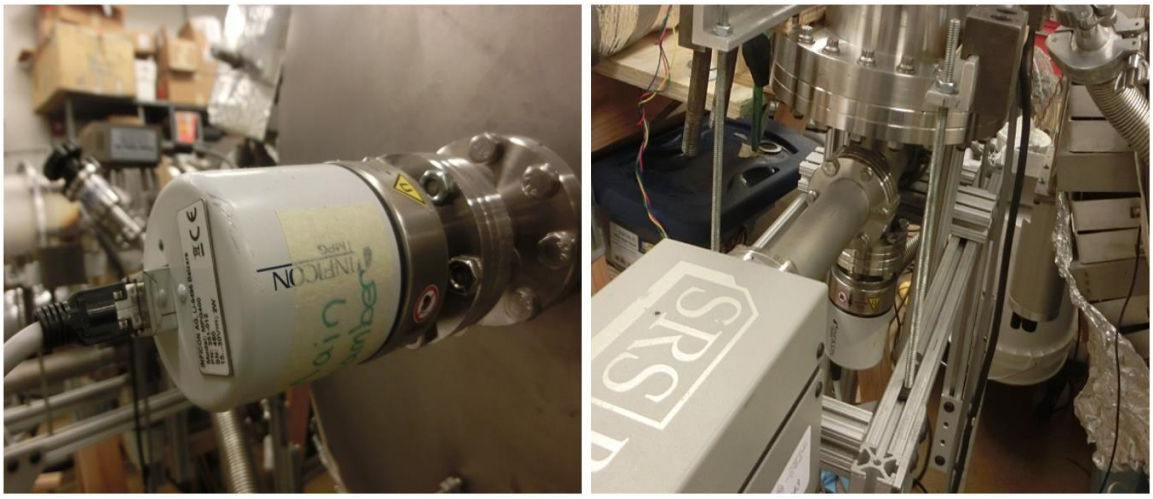

Figure 3.7. Inficon Pressure Gauges. Left: Main chamber gauge. Right: Mass Spectrometer Gauge.

Seven K-type thermocouples were used to monitor temperature at different of locations. Four were fed in through the top of the furnace (Figure 3.8) and embedded in samples (described in Section 3.2.3), one was left hanging in the main volume of the pyrolysis system, another was placed at a location just in front of the main chamber pressure gauge to ensure that temperature at that locale stayed within a safe operating range for the gauge while the last one was used to monitor temperature at the LN_2 flow outlet (see Figure 3.6), serving to provide information utilized by the Arduino micro-controller in modulating temperature at the cold trap . All thermocouples were sheathed in a protective high-temperature Alumina-Boric-Silicate fiber to prevent contact with each other and other metallic surfaces to minimize the possibility of a ‘short out’. K-type

thermocouples have positive Chromel (90% nickel, 10% chromium) and negative Alumel (95% nickel, 2% manganese, 2% aluminum and 1% silicon) wires and operate in the -200^{0}C - 1250^{0}C range.

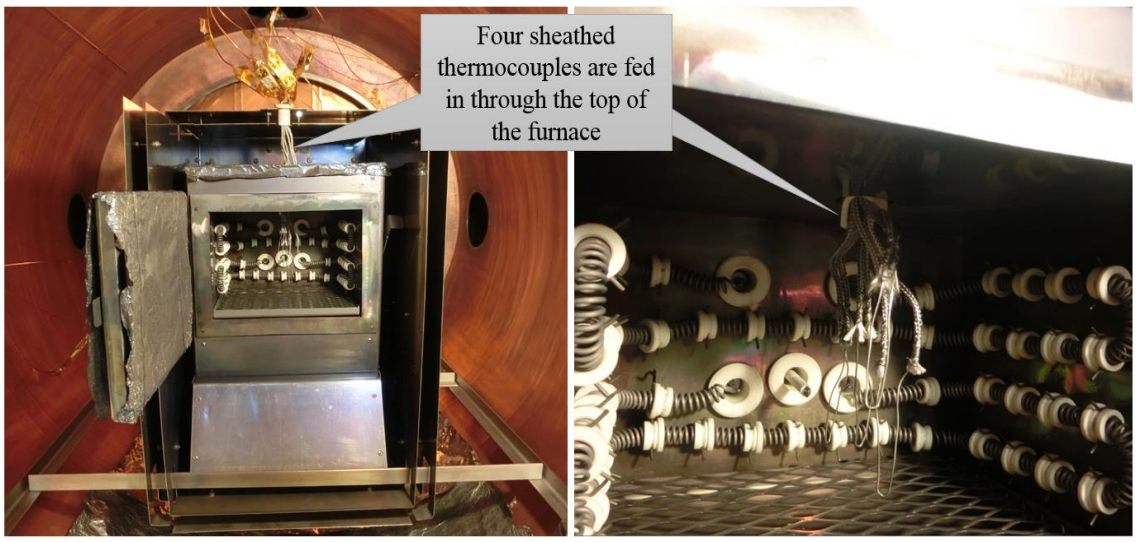

Figure 3.8. K-type Thermocouples in Furnace.

3.1.6. Data Acquisition System. Pressure and temperature readings provided by sensors were recorded using a computer-based data acquisition system (Figure 3.7). The data logging software (National Instruments LabVIEW) was programmed to record data once every two seconds, providing hundreds of thousands of readings for each test run. Temperature was recorded in degrees Celsius while pressure readings in volts were subsequently converted to torr through the application of pressure transducer calibration data. Mass spectrometer data was logged by the Residual Gas Analyzer (RGA) Windows software as raw data from multiple scans over the test period. During experiments, data collected was displayed in a spectrum analysis mode. The RGA head scanned from start

mass to stop mass generating partial pressure (torr) readings every 0.10 Atomic Mass Unit (amu) (see Figure 3.9).

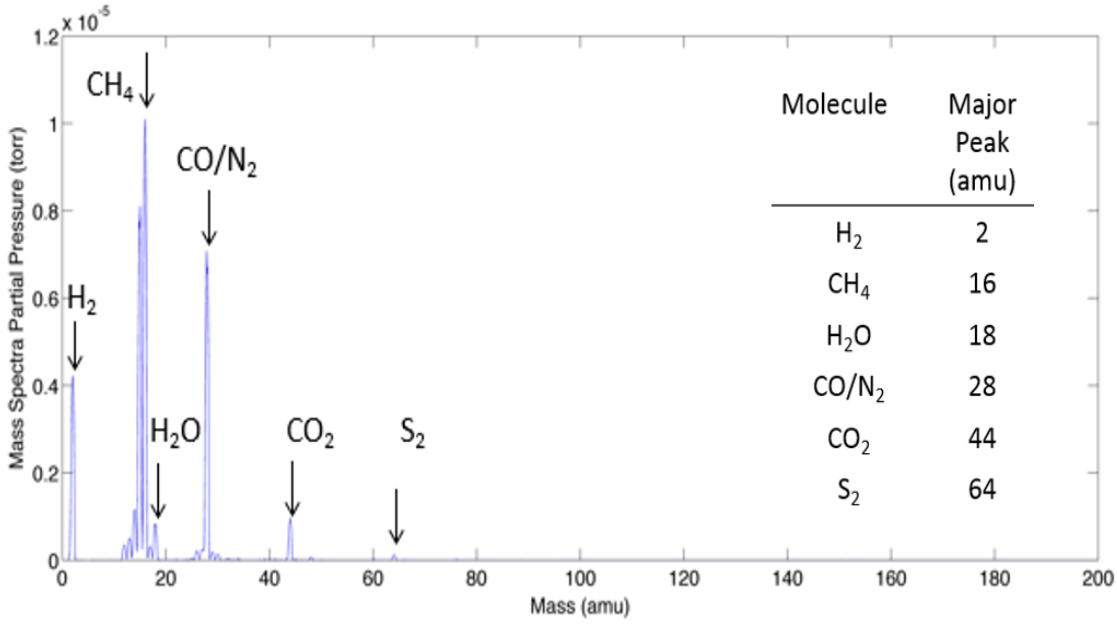

Figure 3.9. Typical RGA Spectrum Analysis View.

It took approximately three minutes to complete a scan over the entire spectrum. Data was recorded in the form of partial pressure readings over the 0-200 amu range. A second dataset was recorded by the RGA applying a matrix inversion technique over the entire derived spectrum to give volume fraction/mole percent readings of a pre-selected range of gases at the end of every three-minute spectral scan. Charts from the second dataset are presented in Section 4 and will herein be referred to as the RGA instant analysis. Figure 3.10 is a labelled diagram showing the location of a number of some system components.

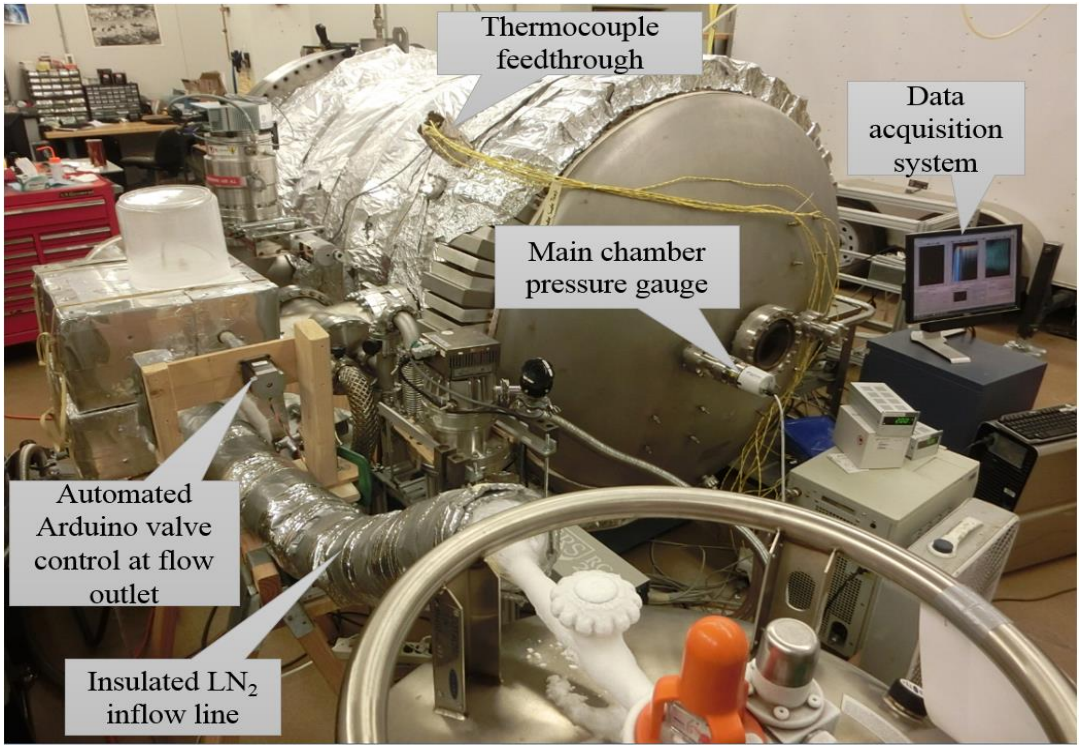

Figure 3.10. Rear-View of Vacuum-Pyrolysis System.

3.2. RESEARCH METHODOLOGY

To achieve stated objectives, a systematic experimental methodology was developed and refined with the various components of the experimental system fabricated and coupled as outlined above. The method adopted is hereby broken down into four parts: sample selection and characterization, system preparation, experimental procedures, measured and derived parameters and sources of error.

3.2.1. Sample Selection and Characterization. A total of eight bulk samples were tested using this setup. These include: one sample each of olivine and serpentine, three samples of high-fidelity simulants of volatile-bearing asteroid bodies of interest in

granular form and three samples of the same simulant but this time consolidated into a well-defined form.

Minerals of the serpentine group are phyllosilicates, having the general formula X_6 Y_4 O_{10} $(OH)_8$; X may be Mg, Fe, Ni, Al, Zn, Co, Cr, Ti, or Mn and Y stands chiefly for Si and in part for Al and Fe which allows for substitution not only in the X and Y positions but also in the position allocated to (OH) where F and Cl may enter (Faust and Fahey, 1962). The most abundant serpentine minerals are hydrous magnesium silicates classified as antigorite, chrysotile and lizardite based mostly on crystal structure (Faust and Fahey, 1962). Natural serpentines (serpentinite rock) like the kind that was used in this project are rarely, if ever, composed of a single pure end-member but rather belong to multicomponent systems.

Olivines are a group of non-hydrous silicate minerals that have a generalized chemical composition of X_2SiO_4. "X" in this composition is usually Mg or Fe, but can occasionally be Ca, Mn, or Ni. For most, composition lies somewhere between pure forsterite (Mg_2SiO_4) and pure fayalite (Fe_2SiO_4) and in this series, Mg and Fe can substitute freely for one another in the mineral's atomic structure. This type of continuous compositional variation is known as a "solid solution" and is represented in a chemical formula as $(Mg,Fe)_2SiO_4$.

Serpentine and olivine group minerals are major phases present in carbonaceous asteroids and represent opposite ends of the spectrum in terms of volatile production. While serpentine minerals are estimated to produce 12-13 wt.% water from hydroxyl groups present in their crystal structure, a pure olivine mineral is not expected to produce gas under the test conditions. Heating one of each type of these two minerals using the vacuum-

pyrolysis system demonstrates its response to a high-grade source of water (i.e. serpentine) and its response to a low-grade material (i.e. olivine). They were tested to evaluate the sensitivity of the experiment setup and procedures to the test parameters.

Gravel-sized pieces of naturally occurring serpentine and olivine were obtained from commercial vendors and broken down to smaller sizes using a jaw crusher, a roller crusher and a plate pulverizer. The actual composition of these samples was confirmed by collecting backscattered images and elemental maps from polished surfaces using Scanning Electron Microscopy (SEM) techniques while their mineralogical composition was investigated by use of X-Ray Diffractometry (XRD).

Backscattered electrons consist of high-energy electrons originating in the focused electron beam that are reflected or back-scattered out of the specimen by elastic scattering interactions with specimen atoms. The compositional contrast apparent in the backscattered images presented in Figures 3.11(a) and 3.12(a) alludes to the presence different chemical phases. This contrast mechanism, distinguishable by the different shades of grey arises from a specimen's compositional influence on backscattering as the intensity of the signal generated from areas with different composition is proportional to the difference in the average atomic number of the respective areas. Heavy elements backscatter electrons more strongly than light elements so accordingly, regions of high average atomic number appear bright relative to regions of low atomic number.

Energy dispersive spectroscopy (EDS) is also an SEM analytical technique used for the elemental analysis of a specimen. Characteristic x-rays are produced by the interaction of a focused electron beam with the specimen under study which are detected and analyzed to map the distribution of elements present and allows for the measurement

of elemental composition. Figures 3.11(b) and 3.12(b) show elemental maps collected over selected areas for selected elemental species.

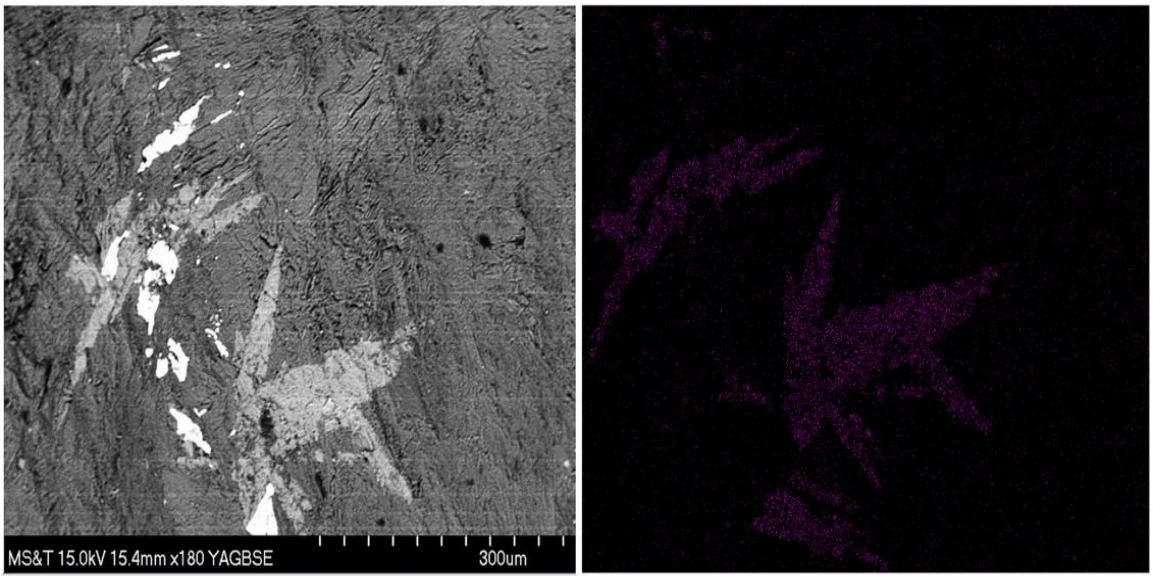

Figure 3.11. Serpentine. A) Backscattered image. B) Calcium elemental map.

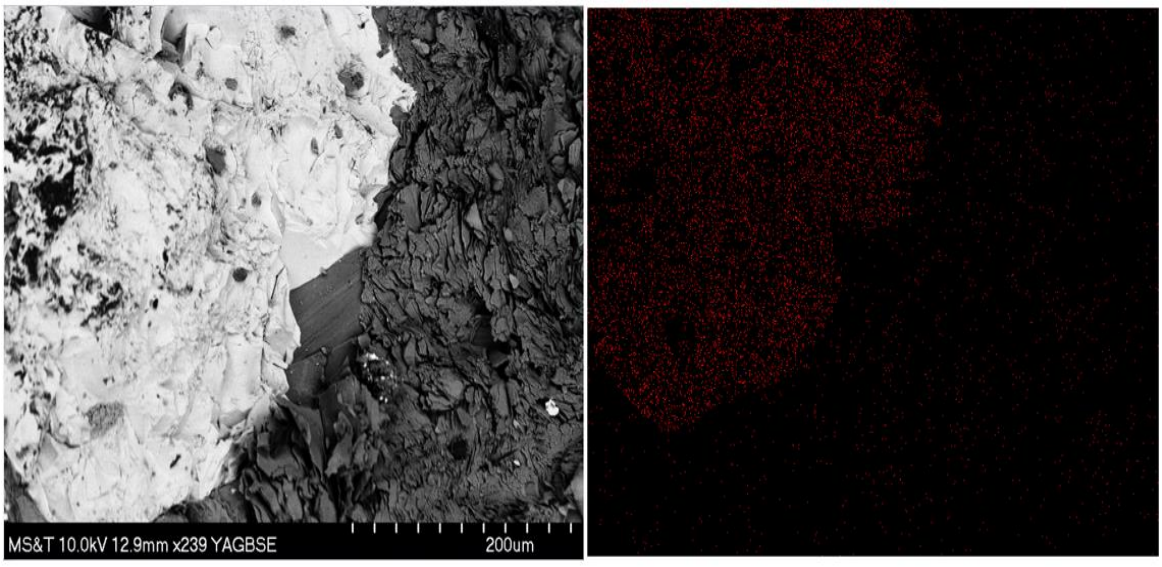

Figure 3.12. Olivine. A) Backscattered image. B) Chromium elemental map.

From Figure 3.11 (a), it can be seen that there are at least three distinct chemical phases present in the imaged surface of the serpentine specimen. Figure 3.11 (b) is an elemental map over roughly the same area that revealed that the second brightest phase shown in the backscattered image was rich in calcium. Other elements found to be present included carbon, iron, silicon and magnesium. Figure 3.12 (a) showed the presence of at least two distinct chemical phases in the imaged surface of the olivine specimen. Figure 3.12 (b) is an elemental map over roughly the same surface that revealed that the brightest phase shown in the backscattered image was rich in chromium. Other elements found to be present included carbon, aluminum, silicon and magnesium.

X-ray Diffraction (XRD) is an analytical technique which relies on constructive interference (and a diffracted ray) of monochromatic X-rays with a specimen for phase identification of crystalline materials. Constructive interference and a diffracted ray are produced when conditions satisfy Bragg's Law ($n\lambda=2d \sin \theta$). This law relates the wavelength of electromagnetic radiation to the diffraction angle and the lattice spacing in a crystalline material. Diffracted X-rays are then detected, processed and counted. Conversion of the diffraction peaks to d-spacings allows for the identification of the mineral because each mineral has a unique set of d-spacings. This is achieved by comparison of d-spacings with standard reference patterns.

Results shown in Figure 3.13 identified lizardite ($Mg_3Si_2O_5(OH)_4$) as the major mineral present in the serpentine sample. The presence of unmatched peaks indicate the presence of unidentified minor/accessory minerals.

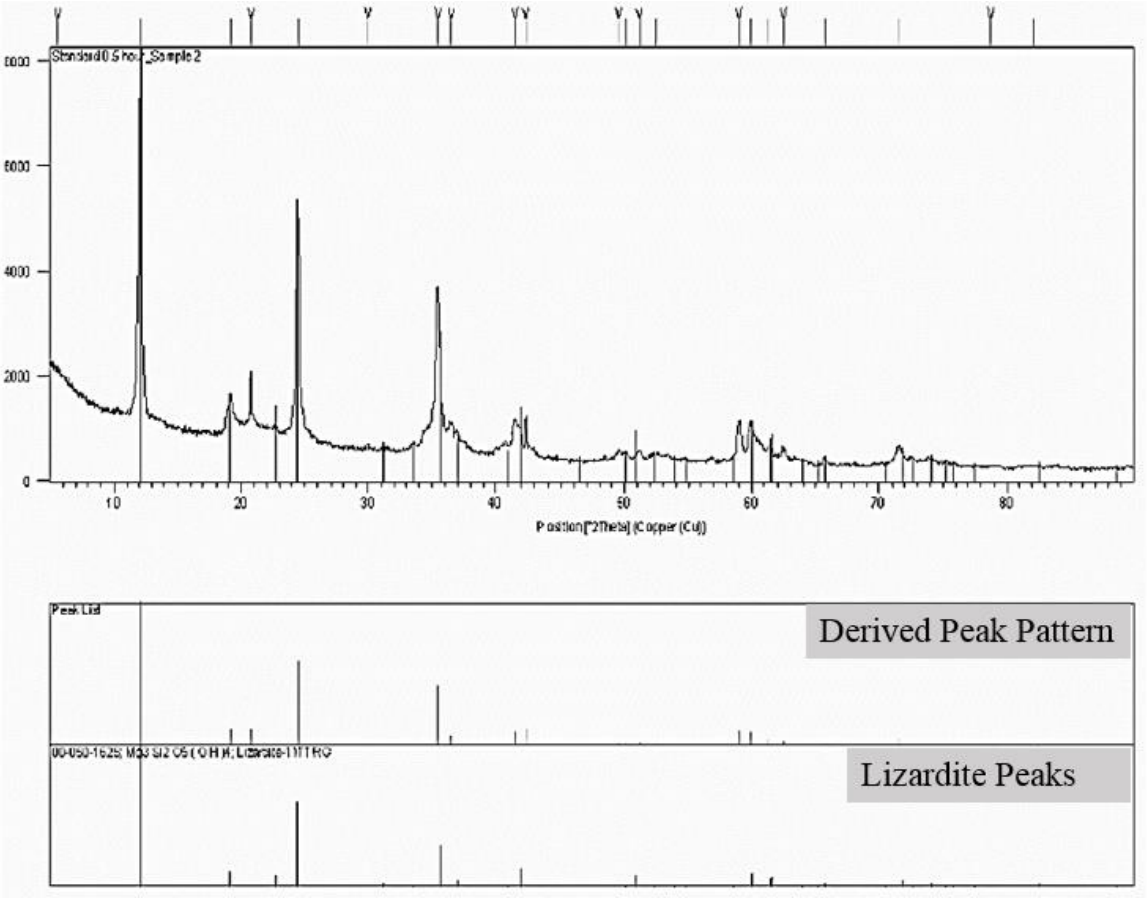

Figure 3.13. XRD Peak Pattern from Serpentine.

Figure 3.14 shows results from XRD tests conducted on olivine samples. The Mg-rich end member of the series forsterite (Mg_2SiO_4) was most abundant mineral present. Lesser amounts of impurities in the form of lizardite were also found to be present implying that this sample type was not completely inert and could produce gas at certain temperatures.

Carbonaceous meteorite simulants obtained from researchers from the Center for Lunar and Asteroid Surface Science (CLASS) at the University of Central Florida represented high fidelity simulants for this research project. These multi-mineralic samples were deliberately designed to mimic the mineralogical and material properties of the

Orgueil meteorite, a well-studied, primitive and volatile rich carbonaceous chondrite (CI-type) that fell in southwestern France in 1864. The most directly representative material for water-bearing asteroids are carbonaceous chondrite meteorites (Saal et al., 2013). The mineralogical make-up of this simulant is presented in Table 3.1, phases important for gas production are Mg-serpentine, vermiculite, epsomite, smectite, pyrite and kerogen (sub-bituminous coal). The manufacture of such simulants was authorized by NASA to fill the gap caused by the paucity of actual asteroid/meteorite samples.

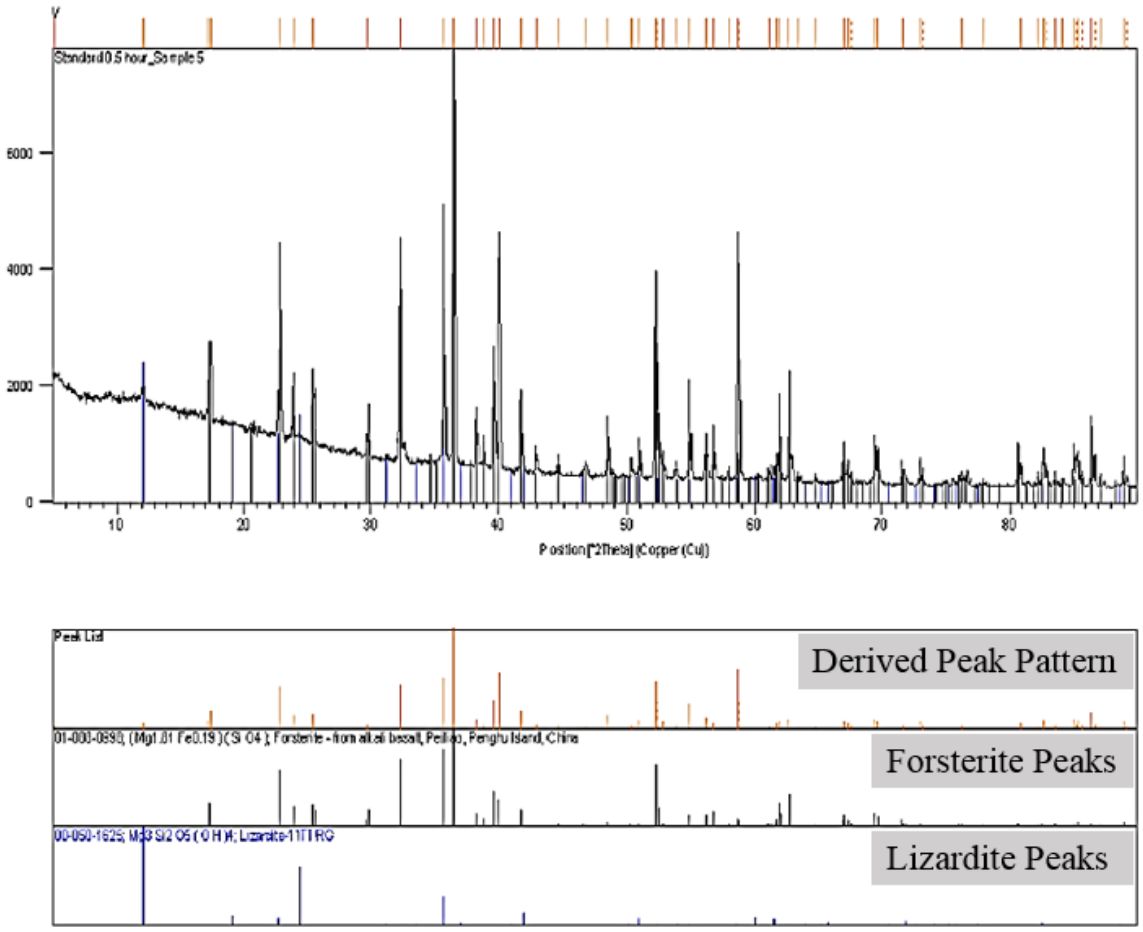

Figure 3.14. XRD Peak Pattern from Olivine.

The granular and ‘consolidated’ samples of this type, used in this project (Figure 3.15) contain a number of hydrated and carbonated phases fabricated into one material by mixing finely ground powders of several component terrestrial minerals. Consolidated samples were manufactured by CLASS personnel by further transforming originally granular simulant material into a solid by mixing four parts of the simulant with one part water, by mass. Spoonfuls were then gently packed by CLASS personnel into molds (Figure 3.15b) and dried for one week until the total mass ceased to decrease due to evaporation of loosely held excess water.

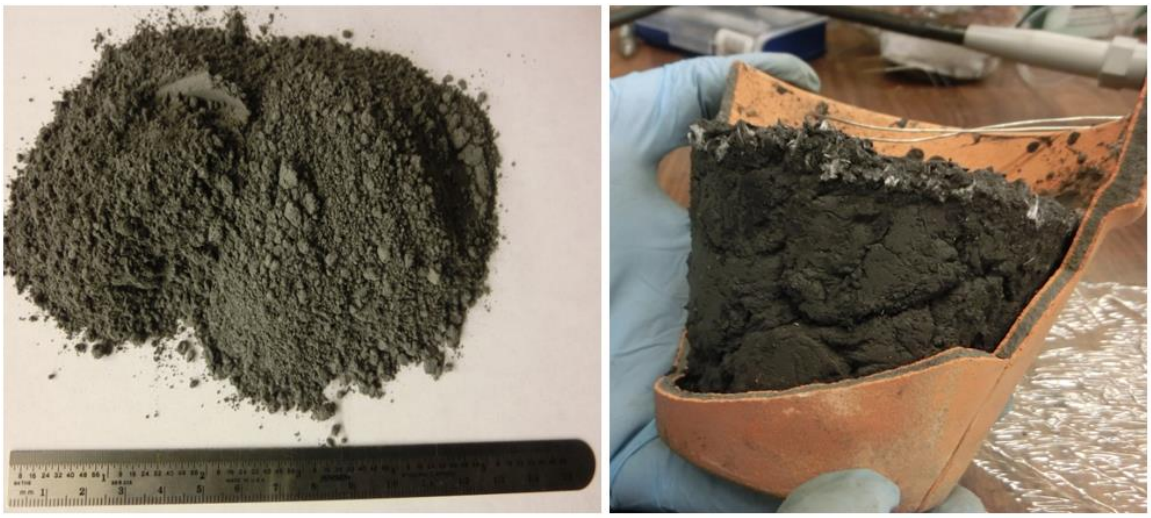

Figure 3.15. Orgueil Simulant. A) Granular form. B) Consolidated form while being removed from clay mold.

The granular simulants were sieved to determine their grain size distributions which was found to be relatively consistent. From Figure 3.16, a D_{50} passing size of 110µm, 190µm, 140µm was obtained for the Orgueil simulant, serpentine and olivine respectively. The D_{50} size defines the median value of a particle size distribution meaning 50% of the

grains in that distribution lie above the calculated value while the other 50% falls below the threshold.

Table 3.1. Orgueil Simulant Mineralogy. (D. Britt and Covey 2016).

Meteorite Type	Meteorite Sub-group	Asteroid Type	Major Simulant Minerals	Wt.%
Volatile-rich Carbonaceous Chondrites	CI	D, P, C	Mg-serpentine	48
			Magnetite	13.5
			Vermiculite	9
			Olivine	7
			Pyrite	6.5
			Epsomite	6
			Smectite	5
			Sub-bituminous Coal	5

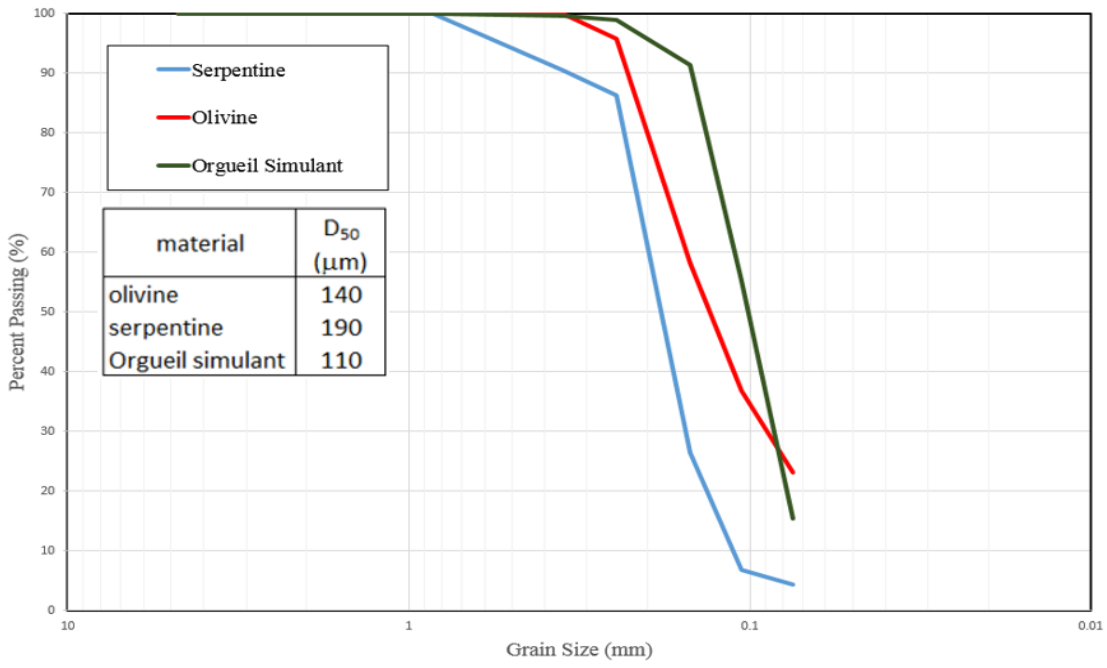

Figure 3.16. Grain Size Distribution of Sample Material. (D_{50} passing size in inset).

3.2.2. Thermogravimetric Analysis (TGA). Thermogravimetric analysis was conducted using an SDT Q600 thermoanalyzer and provided a means to establish the amount/concentration of volatiles within each sample type. In this technique, sample mass loss is recorded as a function of increasing temperature, in a controlled and inert nitrogen atmosphere. Mass loss is interpreted to be the result of de-volatilization and so by collecting this information, it is possible to predict the total amount of gas producible. Samples of 20–40 mg were heated at a constant heating rate of 1^0C/min from ambient to 1400^0C, in an atmosphere purged with dry nitrogen flowing at 100 ml/min. Weight loss profiles from tests on each sample type are presented in Figures 3.17-3.20. Note the variation in vertical scale.

Results from this technique form the basis of subsequent calculations of recovery defined as amount of contained resource successfully retrieved by a particular process. It is important to note however that the thermogravimetric technique differs from conducted vacuum pyrolysis tests in three important ways;

a) The presence of an atmosphere (nitrogen)

b) The size of heated samples.

c) The prograde nature of heat application.

These differences will affect the nature of heat progression and distribution through the material being tested but should not significantly affect the overall amount of gas that can be produced which would remain constant.

Figure 3.17 shows the typical weight loss curve derived from analysis of the Mg-serpentine (lizardite) sample. Total decomposition is achieved at approximately 870^0C with a total of 11.42% of its initial mass lost as volatiles. Significant dehydroxylation starts

to occur around 400^{0}C and most of the mass is lost between 500^{0}C and 730^{0}C as water vapor is formed in an endothermic reaction from the hydroxyl groups present.

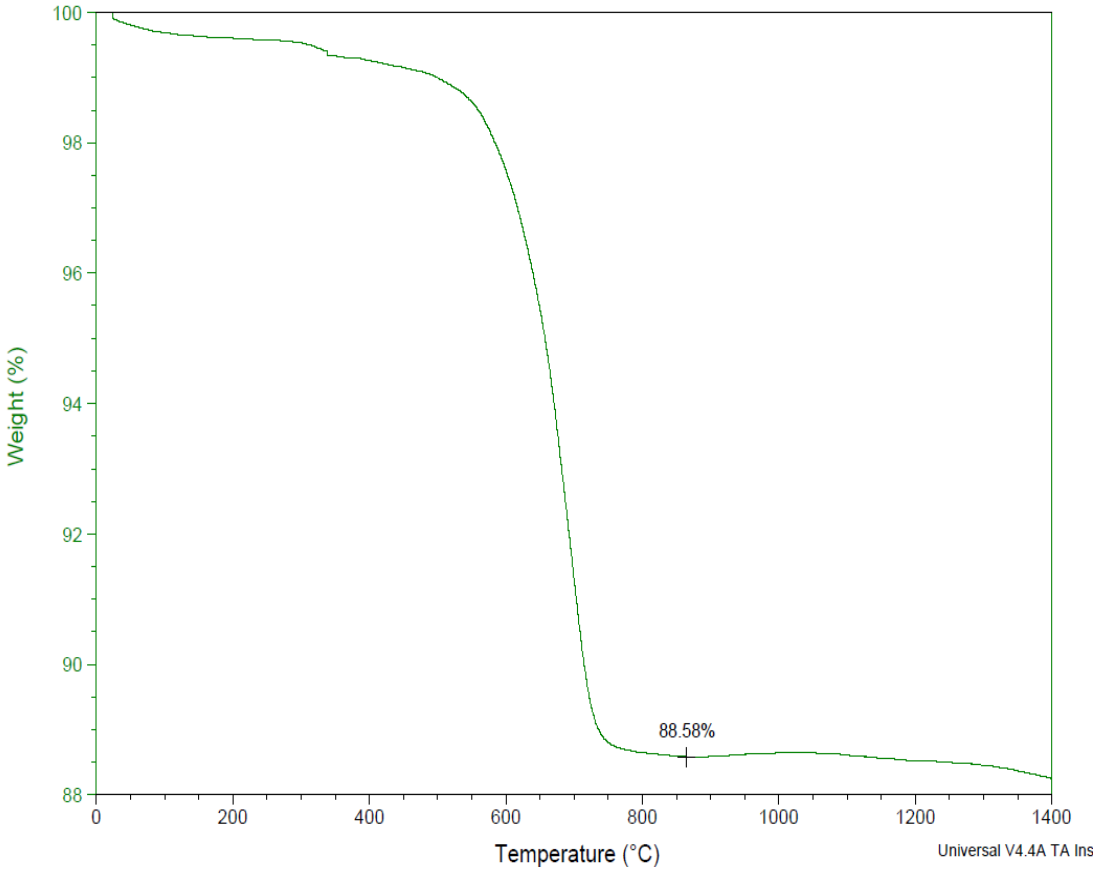

Figure 3.17. Weight Loss Profile of Serpentine. (lizardite).

Figure 3.18 shows the typical weight loss curve derived from heating olivine. Total decomposition is achieved at approximately 670^{0}C with a total of 1.42% of its initial mass lost as volatiles. Significant volatilization starts to occur around 400^{0}C and most of the mass loss occurs between 580^{0}C and 670^{0}C as gases are removed from phases present as impurities.

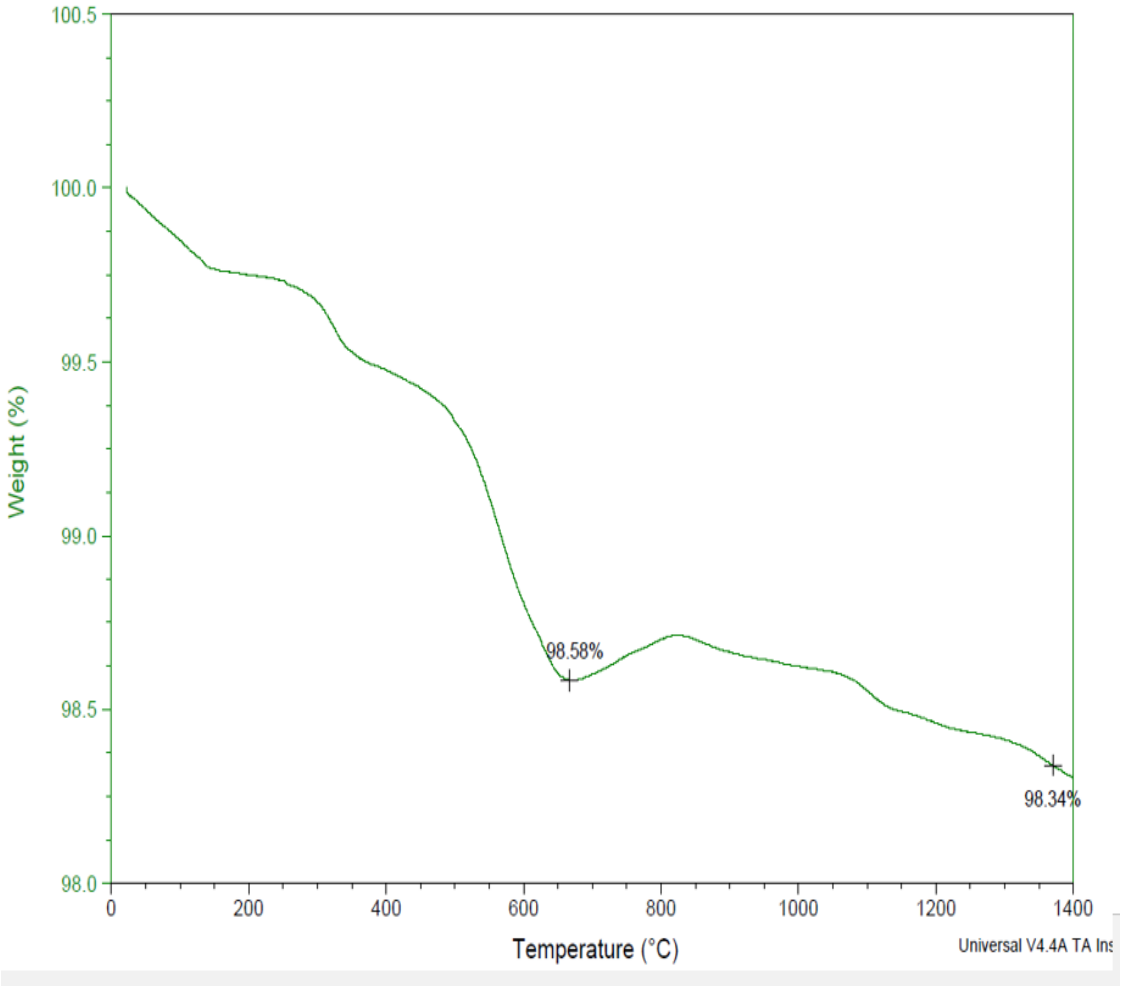

Figure 3.18. Weight Loss Profile of Olivine. (forsterite).

Figure 3.19 shows the typical weight loss curve derived from heating of the granular orgueil simulant. Total decomposition is achieved at approximately 1175^0C with a total of 19.41% of its initial mass lost as volatiles. A steep drop in sample mass occurs soon after heating starts as loosely held water is lost at lower temperatures, the period from 150^0C to 400^0C is relatively stable and significant outgassing resumes at about 450^0C. A significant fraction of total mass loss occurs between 500^0C and 1175^0C as gases are lost from hydroxylated and other volatile bearing phases.

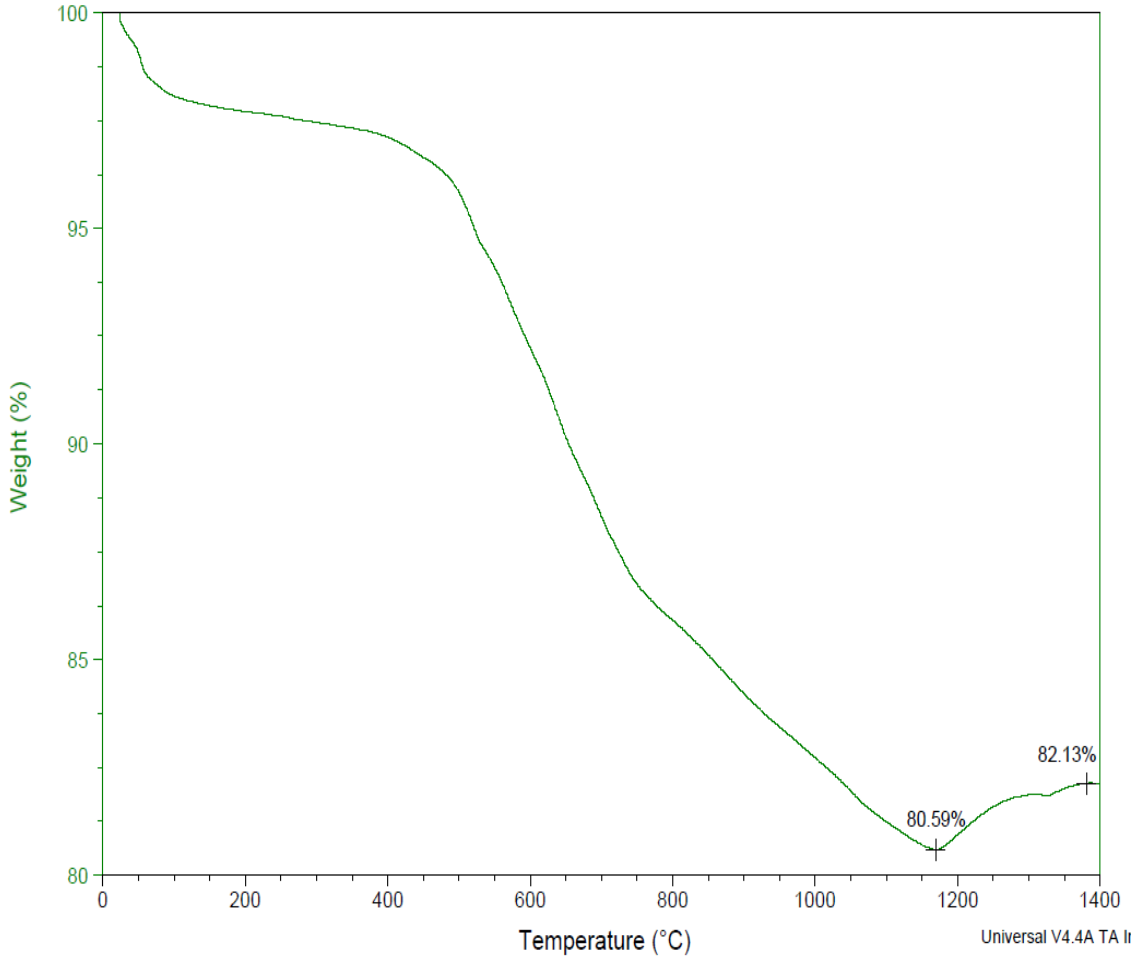

Figure 3.19. Weight Loss Profile of Granular Orgueil Simulant.

Figure 3.20 show the typical weight loss curve derived from heating the consolidated Orgueil simulant. Total decomposition is achieved at 1110^0C with a total of 23.53% of its initial mass lost as volatiles. An even steeper drop in sample mass occurs soon after heating starts as loosely held water is driven off at lower temperatures. The period from 150^0C to 400^0C is relatively stable and significant outgassing resumes soon afterward. A significant fraction of total mass loss occurs between 500^0C and 1110^0C as gases are extracted from hydroxylated and other volatile bearing phases.

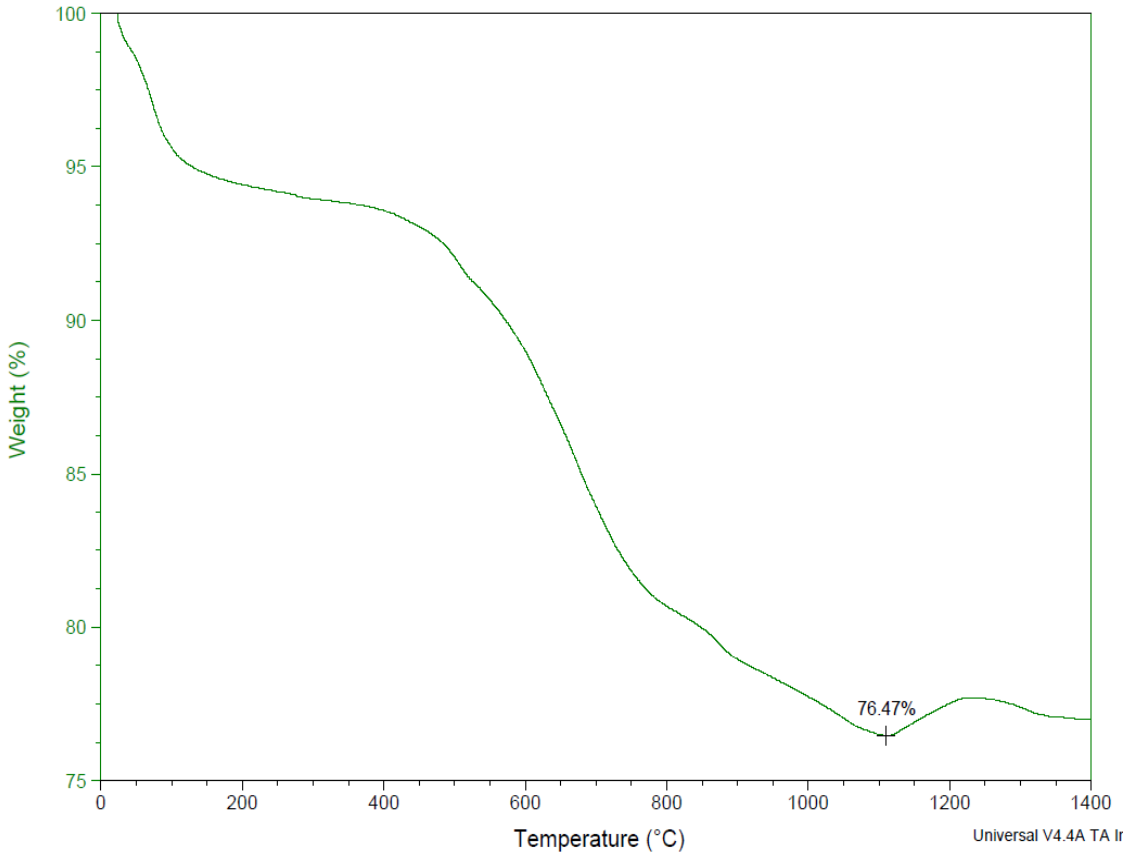

Figure 3.20. Weight Loss Profile of Consolidated Orgueil Simulant.

3.2.3. Sample Setup. Granular samples were placed inside cylindrical hand-fabricated sample containers, made from corrosion-resistant 316 stainless steel mesh cloth with 74microns (µm) openings. The mesh covering served to hold samples in a well-defined shape, prevent the loss of particles during testing and allowed for largely unhindered gas escape through openings. This configuration also allowed four K-type thermocouples to be fed through the top of the furnace and placed at specific locations within the sample mass. The manner of placement is shown in Figure 3.21 with one placed at the geometric center, a second almost centered at the bottom, and each of the remaining two placed at mid-radius from the back and front sides of the sample (back and front with respect to the furnace door.

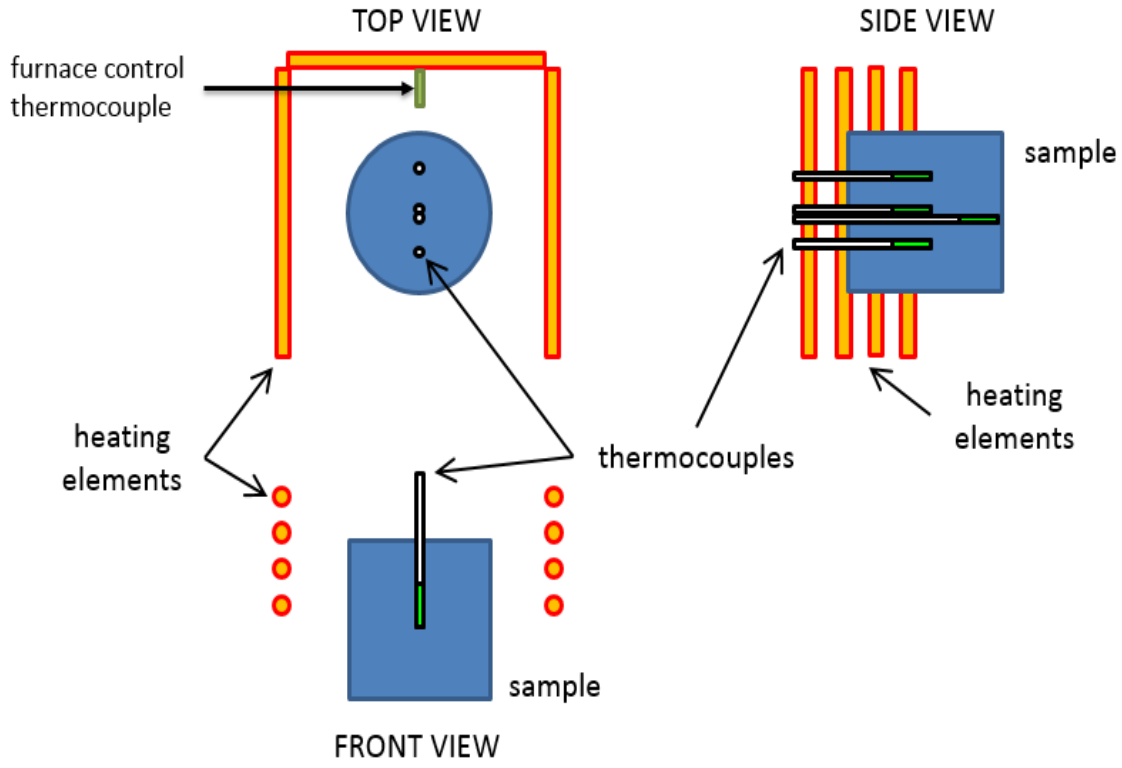

Figure 3.21. Schematic Showing Thermocouple Placement in Granular Sample Mass.

Consolidated Orgueil simulant samples were manufactured with one K-type thermocouple embedded at the geometric center of a truncated cone (Figure 3.22). A bulk granular sample sitting in a fabricated mesh-cloth is presented in Figure 3.23. All (powdered/granular and agglomerated/consolidated) samples sat on a tray mesh that acted to catch any loose particles that came off during sample handling and eventual heating (Figure 3.23 and 3.24). This way, the possibility that any measured loss in sample mass is the result of a phenomenon other than de-volatilization is reduced. Sample sizes were influenced by a desire to use large specimens for which heat and mass transport affect the kinetics of the overall process. A contrary consideration was the greater amount of time it would take to conduct vacuum pyrolysis on larger samples. Generally it is expected that the thermal response of smaller bodies is faster.

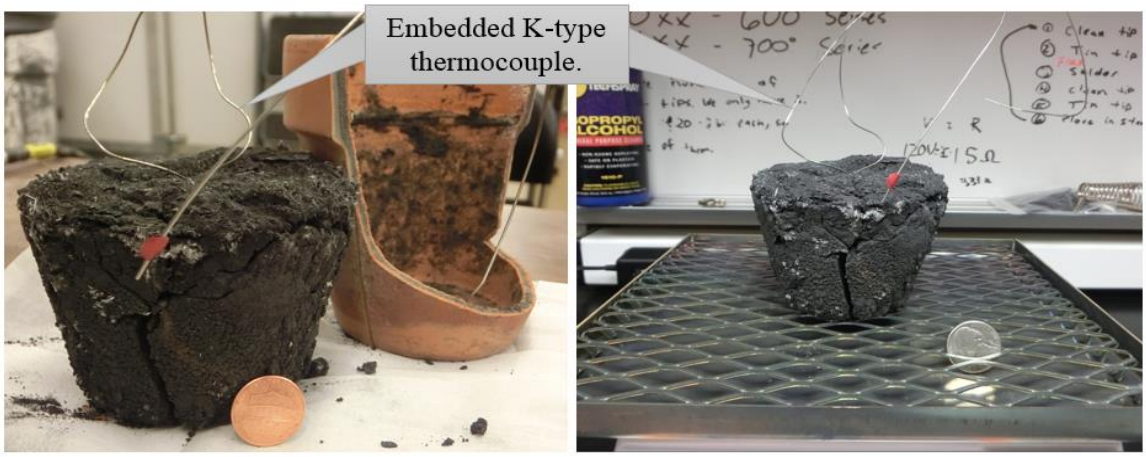

Figure 3.22. Consolidated Sample Setup.

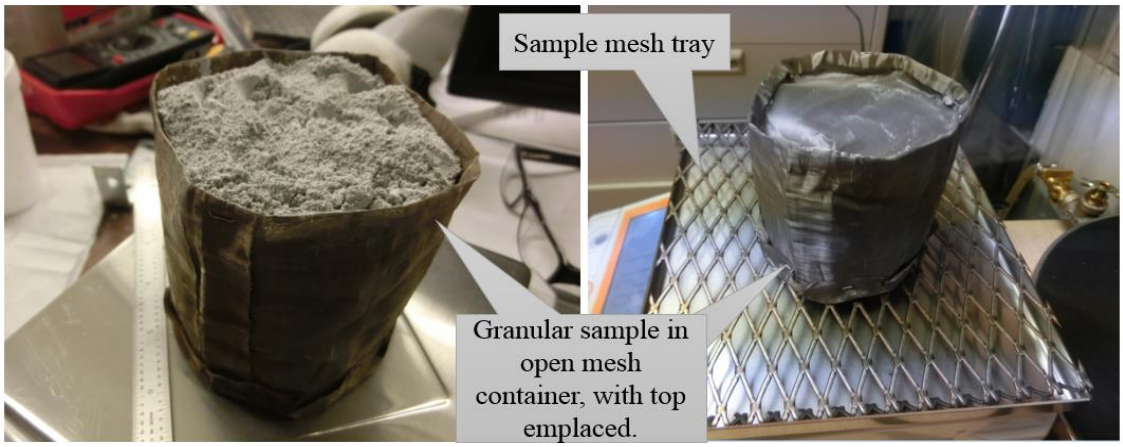

Figure 3.23. Granular Sample Setup.

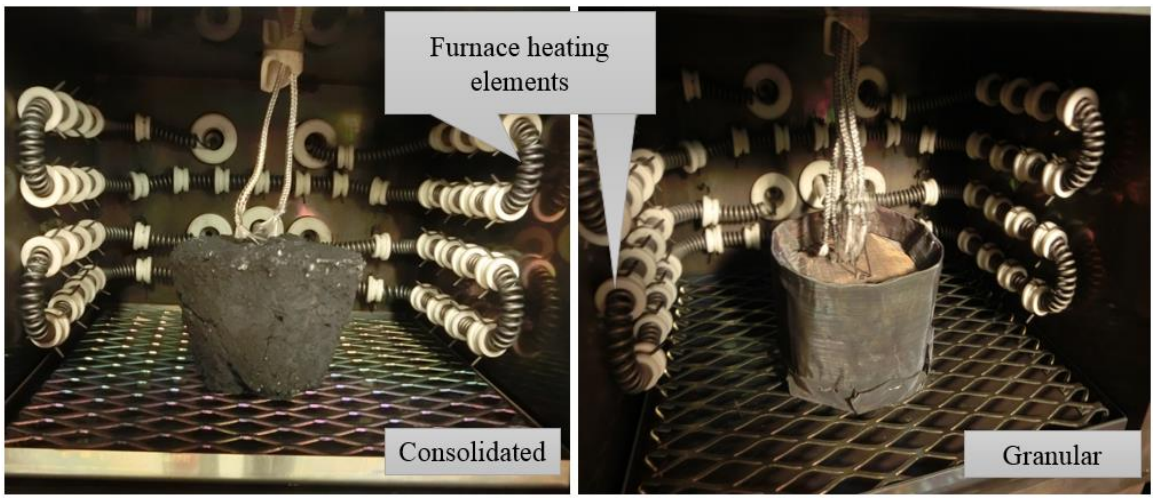

Figure 3.24. Sample Setup before Start of Experiment.

3.2.4. Vacuum System Preparation. Before the start of each experiment, the vacuum chamber and all components to be used were cleaned to minimize pump-down time and limit inter-test contamination. A mixture of non-toxic, non-flammable, biodegradable 'Simple Green' (soap) and clean water was used with a soft sponge to remove grime that may have accumulated from previous tests. Clean 'wipes' infused with ethanol were then used as a final cleaning step. Smaller components such as the sample mesh container and sample tray mesh were put in an ultrasonic cavitator filled with the 'Simple Green' mixture for at least 30 minutes to remove potential contaminants.

After the conclusion of these steps, the system was set up with all the components to be used but without the presence of a sample. The chamber was then sealed and subjected to a pumpdown-bakeout' sequence. During this procedure, the vacuum-pyrolysis system was brought down to test pressure and after this, the furnace was turned on to 650^0C to heat all surfaces within the system. The net effect of simultaneous heating and pumping of the system was the expulsion of moisture that may have adhered to the chamber surfaces during exposure to the atmosphere and the previous cleaning step. The system was allowed to run under these conditions for at least 12 hours. At the end of the pumpdown-bakeout sequence, pressure was allowed to naturally 'leak-up' so that the chamber could be opened and the samples inserted. The pressure history curves were recorded to determine if any leaks were present.

3.2.5. Experimental Procedures. The chamber was opened and a prepared sample was placed into the furnace on the sample tray. Samples were set up following the procedures outlined in Section 3.2.3 and embedded thermocouples were attached to

existing connectors and then checked to make sure of proper operation. After all sensors were verified to be working properly, the furnace and vacuum chamber doors were sealed.

For each sample tested, four temperature plateaus were held: the first ramp is from ambient to 250^0C while subsequent ramps are in 150^0C steps up to a maximum furnace temperature that varied between 658^0C and 670^0C. While the sample was being heated, the mass spectrometer identified evolved gas species produced in the residual environment and the cold-trap was kept frozen by flowing liquid nitrogen through its spiraled tubes acting to collect evolved products. Figure 3.25 shows an image of the furnace controller.

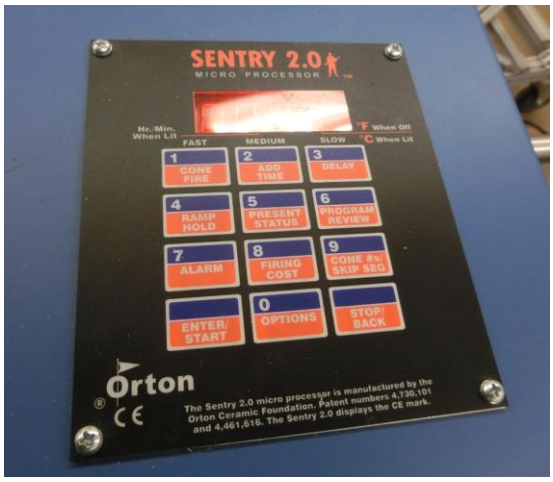

Figure 3.25. Furnace Controller.

Each temperature plateau was held for three thermal time constants, calculated by fitting an exponential curve to the temperature curve obtained from the thermocouple placed at the geometric center of the heated mass (Section 3.2.11). A second criteria to be met was evidence of a significant drop in volatile production indicated by a characteristic fall in total chamber pressure after an initial rise as furnace temperature was ramped

upwards. When a plateau was deemed to have ended, the icy material collected on the cold-trap was weighed, collected and stored for further analysis.

A simplified flow-chart of the procedures adopted is presented in Figure 3.26:

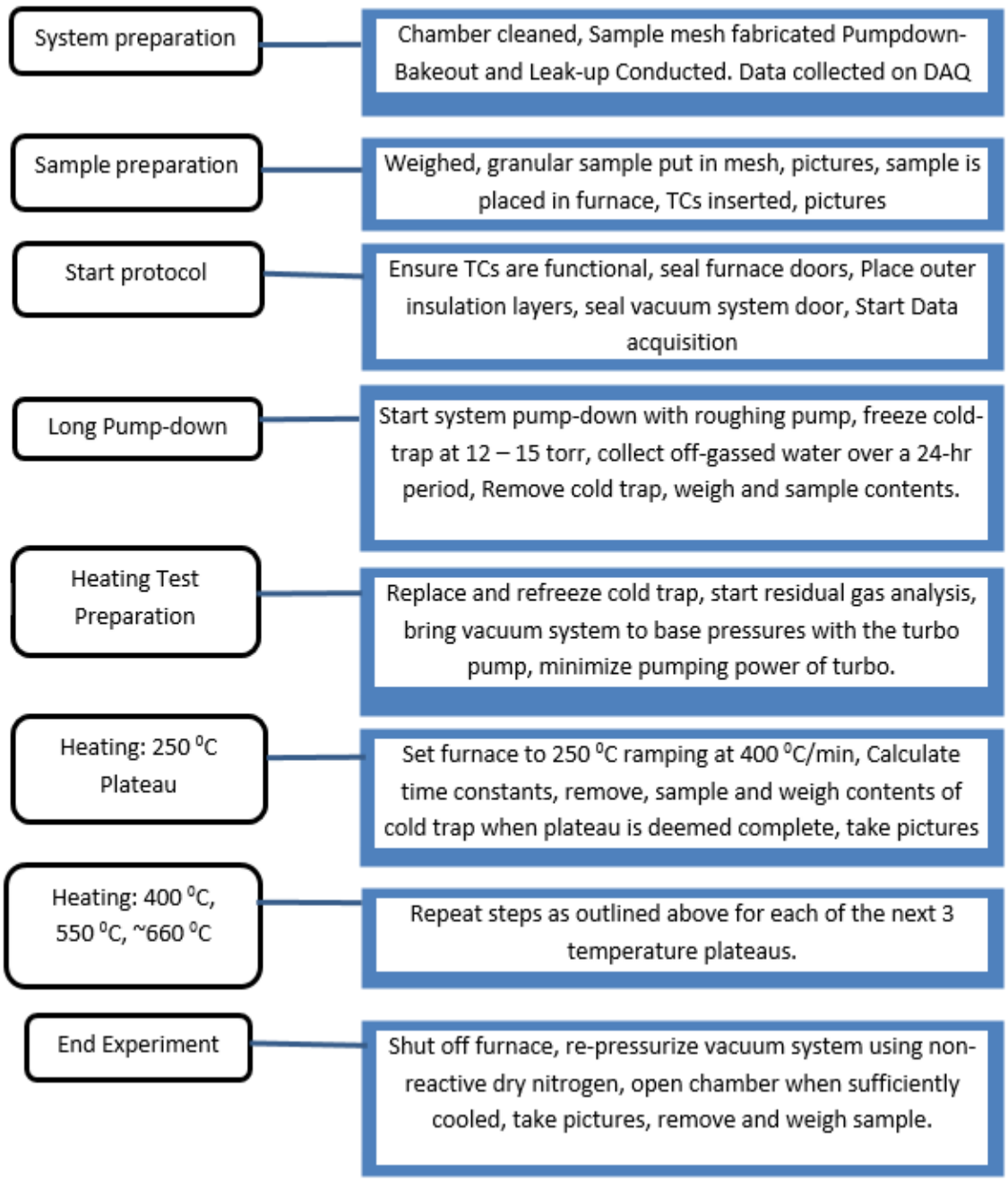

Figure 3.26. A Simplified Flow Chart of Procedures.

3.2.6. The Problem of Background and Un-trappable Gases. Gases such as hydrogen, water, nitrogen and carbon dioxide are commonly present within a vacuum system even at its ultimate vacuum. Hydrogen and other gases are produced from metal surfaces within the system. This is enhanced when these surfaces are at elevated temperatures which means that without the benefit of active pumping, chamber pressure will rise due to contributions from the release of these gases. This situation was exacerbated during testing by sample out-gassing of compounds such as carbon monoxide which cannot be captured by a LN_2 cooled trap. This led to a build-up in chamber pressure which if unchecked could cause arching of the furnace electronic connectors.

To deal with this, the experiments were run with the turbo-molecular pump operating at reduced capacity (throttled). The turbo-pump flowrate was reduced to approximately 1-2% of the cold trap by partially closing the gate valve leading to the turbo-pump. Running in this fashion allowed for background and un-trappable gases to be removed from the system at a slow but steady rate while trappable gases were immobilized on the surface of the cold-trap.

3.2.7. Handling Atmospheric Contamination. A certain fraction of the total volatile content producible from the samples can be considered to be the result of terrestrial atmospheric contamination in the sense that this portion is not mineralogically derived but was likely sourced as a result of adsorption from the earth's atmosphere. Such contamination in the Orgueil simulants may also conceivably be a byproduct of the process by which these simulants were manufactured (Section 3.2.1). This fraction therefore does not represent volatile gases present on an asteroid body of this type and should be dealt with separately. Researchers have typically used a low temperature threshold (200^0C-

300^0C) to separate this portion, characterizing gas that evolved below that point as atmospherically adsorbed (Court and Sephton, 2014). However, while low-temperature heating will drive off this weakly bonded water, it will also dehydrate some mineral phases of indigenous water, particularly sulphates such as epsomite.

To explore the effect of atmospheric contamination on test results, each sample was subjected to a pump-down at ambient temperature (~45^0C) for 24 hours. The cold trap was operated, and the icy material collected on the trap was retrieved and weighed just as at the end of a non-ambient temperature plateau. All data collected below 250^0C may be considered to be due to atmospheric contamination.

3.2.8. Temperature Plateau Duration. During testing, the furnace was held at each of four plateaus until certain well-defined criteria were met before increasing to the next. To ensure a workable and consistent plateau duration for different samples of varying sizes and material properties, the following conditions were to be achieved before moving to the next temperature step:

1. The plateau duration must exceed three times the thermal time constant of the sample, determined by fitting an exponential curve to the temperature history of the sample's centroid (see section 3.2.11).
2. The volatile release rate estimated by pressure in the vacuum chamber must fall below 10% of the initial peak for that temperature plateau.

Numerous experiments showed that the second condition was quickly met making the first criteria the controlling factor determining test duration. Thermal time constants were calculated by fitting an exponential curve to the temperature curve derived from the thermocouple placed at the sample center while volatile release rate was visually estimated

from observations of measured chamber pressure which is a proxy. Decisions regarding when to end a plateau were taken in real time while heating took place. After set criteria were met, the plateau was deemed to have ended and the cold-trap was removed, weighed and sampled.

3.2.9. Weighing and Sampling the Cold Trap. At the conclusion of each temperature step/plateau, the cross was isolated from the main vacuum chamber and the mass spectrometer by shutting the connecting gate valve and sampling valve respectively (see schematic in Figure 3.1). The isolated four-way cross was then pressurized using a carefully controlled flow of dry nitrogen into the volume through a 1.3 cm (~0.5-inch) line from the LN_2 cylinder. When the volume had been brought up to atmospheric pressure, flow of dry nitrogen and LN_2 was stopped and the cold trap was detached from the cooling lines and carefully pulled out from the four-way cross (Figure 3.27). Pictures were taken and the cold trap was placed into a measuring container of known mass, and subsequently weighed on a scale. This final step is done in the quickest possible fashion to minimize, the condensation of atmospheric gases on cryogenic surfaces of the cold trap.

After the mass was measured (mass of ice), pressurized air was flown through the stainless steel tubes of the cold trap while it remained in the measuring container to hasten the phase change from ice to a liquid melt. Once, the icy material was dissolved into the measuring container, the mass was again measured to obtain the mass of the liquid melt. The measuring scale was rated for 10 kg and had an accuracy of 0.1 gram. The liquid melt was afterward labelled and stored in clear containers for future analysis.

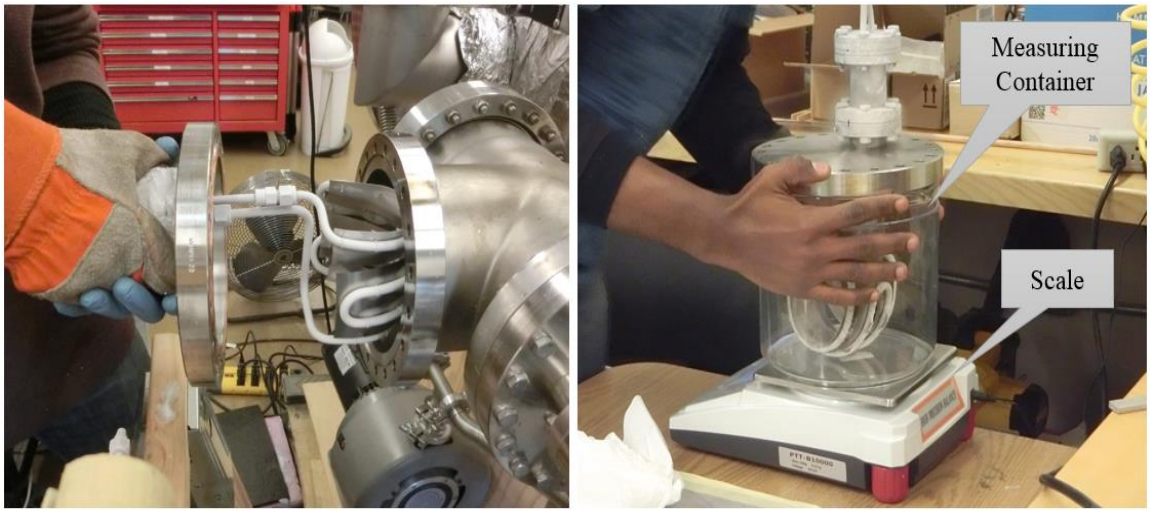

Figure 3.27. Detaching and Weighing the Cold Trap.

3.2.10. Measured Parameters.

- Initial Sample Mass (u). This was the mass of the sample measured prior to the start of heating. At this time the sample contained all of its volatile resource.
- Final Sample Mass (v). This was the mass of the sample measured immediately after it was removed from the chamber at the conclusion of a test. At this time, it had been depleted of some of its resource.
- Mass of Ice (m_i). This was the mass of icy material collected from the sample after specified periods. This measurement was taken five times (m1, m2 …m5) during a typical experiment; once at the end of each of four temperature plateaus and once after the initial ambient-temperature pump-down. A systematic error of 1.1 gram affecting this measure was subtracted from each raw measurement to get q1, q2…q5 (See Section 3.2.11).
- Mass of Liquid Melt (m_l). This is the mass measured after the artificially accelerated phase change from an icy material to a liquid melt at ambient

conditions. This measurement was typically taken five times (m1, m2 …m5) during an experiment. A systematic error of 1.1 gram affecting this measure was also subtracted from each raw measurement to get q1, q2….q5 (See Section 3.2.11).

- Sample and Chamber Temperature. K-type thermocouples placed at various locations provided information on temperature distribution within the overall vacuum-pyrolysis system and the tested samples.
- Chamber Pressure. Pressure was recorded from two locations within the vacuum-pyrolysis system.

3.2.11. Calculated Parameters.

- Change in Sample Mass (w). This is simply the difference in grams between a samples initial mass and its final mass. The change assumed to be a result of volatile removal.

$$w = Initial\ mass\ (u) - Final\ mass\ (v)$$

- Total Mass of Ice (z_i). This is the total sum in grams of the mass of icy material recovered at the cold trap during the various stages of an experiment on one sample.

$$zi = q1 + q2 + q3 + q4 + q5$$

- Total Mass of Liquid Melt (z_l). This is the total sum in grams of the mass of liquid melt collected after the various stages during an experiment on a particular sample.

$$zl = q1 + q2 + q3 + q4 + q5$$

- Cold Trap Efficiency (e) (%). This was defined as a ratio of the total amount of ice collected by the cold trap to the change in sample mass.

It provides a quantitative measure of the effectiveness of the trap at recovering produced gas as sample mass loss was assumed to be a direct consequence of de-volatilization.

$$e = \frac{zi}{w} \times 100$$

- Recovery (%). The recovery of a desired resource is the ratio of the amount extracted to the amount contained within the ore; for the purposes of this project, it provides a measure of the degree to which the available gas compounds in samples are retrieved by the cold trap. The samples tested in these experiments represent carbonaceous ore bodies for which thermogravimetric analysis revealed total amount of producible gas contained within each type. Recovery is calculated by deriving the ratio between the total mass of ice recovered and the total mass of gas producible.

$$Recovery = (zi \div total\ mass\ of\ producible\ gas) \times 100$$

- Extraction Efficiency (%). This is a measure of the amount of producible resource (gas compounds) that was successfully extracted by this experimental process. The amount extracted was known from the change in sample mass after the conclusion of the test, where mass loss is assumed to be solely the result of gas release. Extraction efficiency is calculated as a percentage from the ratio between the change in sample mass and the amount of producible gas within that sample.

$$Extraction\ Efficiency = (w \div total\ mass\ of\ producible\ gas) \times 100$$

- Thermal Time Constant. Because heat was the driver of extraction, the speed of its interaction with the sample was important for deciding when to end a temperature plateau, especially as materials of varying physical properties were being tested.

To do this, and also to control the experiment schedules, an exponential thermal time constant was calculated for every sample at every temperature step.

$$T = (T2 - T1) \times \left(1 - e^{\left(-\frac{t}{\tau}\right)}\right) + T1$$

Where, T_1 = Initial body temperature

T_2 = Final body temperature

T = Body temp

t= Time required (t_2-t_1) for temp change

τ = Time constant

When t = τ, the body has reached 63.2% of its final temperature as shown in the Figure below. When t = 3τ, the body has reached 95% of its final temperature. The temperature of an object progresses toward the temperature of its environment in a simple exponential fashion (Figure 3.28).

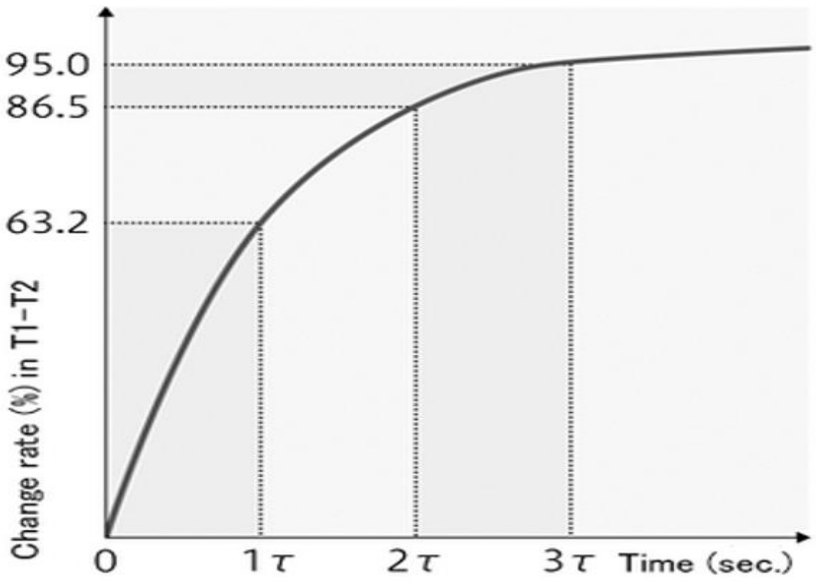

Figure 3.28. Exponential Decay Curve. The time constant (τ) is the amount of time it takes to reach 63.2% of steady state value.

This approach relies on the assumption that heat transfer through a body is much faster than heat transfer across the boundary of the body, in essence simplifying the heat transfer problem to describe a time-varying but spatially-uniform temperature field within the material. The appropriateness of this assumption will be the subject of future papers; however, in the context of this thesis, it provided some consistency to plateau duration. Logistical scheduling meant that plateaus were not always ended immediately after achieving the 95% temperature; the criteria were sometimes extended to fit the day-night cycle. Figure 3.29 shows an exponential curve (orange) fitted to the sample temperature curve (blue) obtained off a sample K-type thermocouple. Fitting started from a point after the initial sample temperature oscillations have ceased.

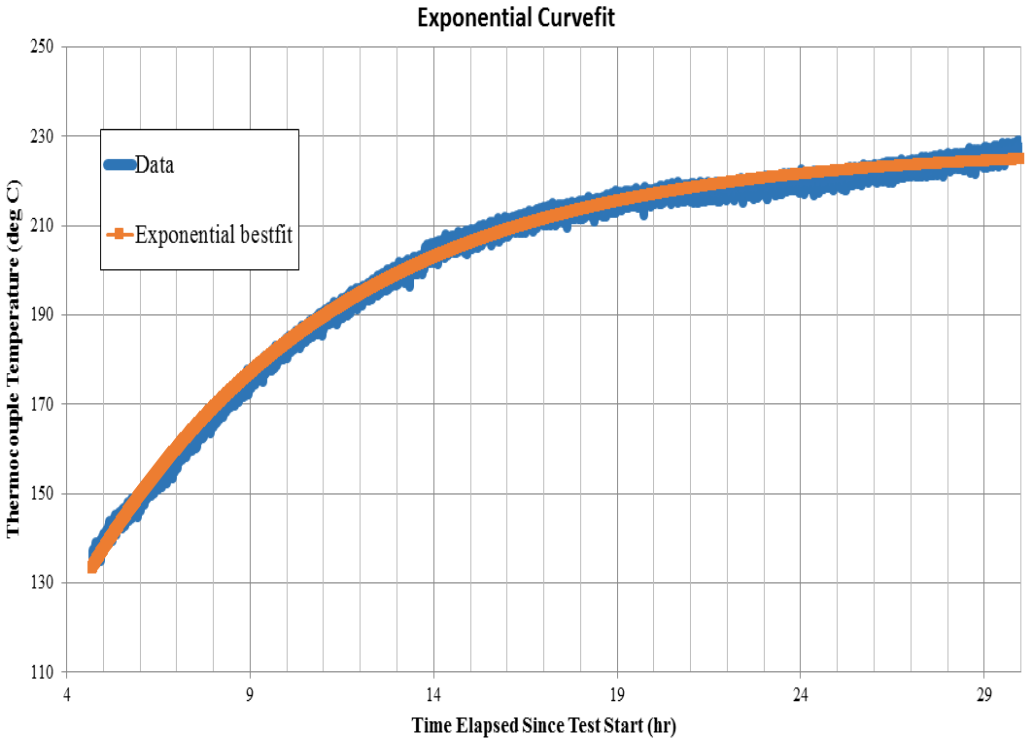

Figure 3.29. Exponential Curve-Fit to Experimental Temperature Data.

3.2.12. Sources of Uncertainty. A source of error in the mass measurements of ice is the uncertainty associated with the amount that can be collected from an empty vacuum chamber. Moisture is ubiquitous in the environment within which we exist and as a result, a finite amount collects on surfaces within the vacuum system. A purpose of the pre-test pump-down and bake-out was to de-moisturize the system and though the contribution from this phenomenon was reduced to a minimum, a certain measurable amount remained. There is also a certain amount of moisture that is collected from the external laboratory environment during the time when the cold trap is pulled out of the system to be sampled and weighed. These factors vary in magnitude as they are greatly affected by humidity and other environmental conditions.

Because contributions from these two sources of uncertainty are always present in the mass measurements of ice and liquid, it was considered a systematic error and the approach taken was to quantify it and subtract the calculated amount from the affected mass measurements. To do this, an empty chamber test was run following the same procedures as were followed for the experiments with samples. From this test, a typical mass value of the amount of non-sample derived ice (that can be collected from an empty chamber and from condensation of atmospheric gases on cold tap components at and after each temperature plateau) was obtained by taking a simple average (1.1 grams) of the icy material collected on the cold trap at the end of each of the four temperature plateaus and initial ambient temperature, pump-down step of the empty chamber test. This mass value was assumed to be a systematic error and was subtracted from each original mass measurement of the icy material and liquid melt. The uncertainty associated with this systematic error (0.4 g) was found to be the biggest contributor to the uncertainty of mass

measurements and propagated through calculations of cold trap efficiency, total mass of ice collected, total mass of liquid collected which are presented in Section four (Table 4.1). The propagation of error was calculated using the following method, where:

$q = reported\ mass\ of\ ice\ or\ liquid\ melt$

$m = measured\ mass\ of\ ice\ or\ liquid\ melt$

$x = systematic\ error\ in\ mass\ measurements\ (1.1g)$

$dx =\ uncertainty\ in\ x\ (0.4g)$

$dm =\ uncertainty\ in\ m\ (0.1g)$

$du = uncertainty\ in\ initial\ sample\ mass$

$dv = uncertainty\ in\ final\ sample\ mass$

$q1 = reported\ mass\ of\ ice\ or\ liquid\ melt\ collected\ after\ 1st\ step$

$q2 = reported\ mass\ of\ ice\ or\ liquid\ melt\ collected\ after\ 2nd\ step$ ….

$q5 = reported\ mass\ of\ ice\ or\ liquid\ melt\ collected\ after\ 5th\ step$

- The reported mass of icy material or liquid melt is simply:

$$q = m - x\ (\pm 0.4g)$$

- Uncertainty in reported mass of ice/liquid melt:

$$dq = \sqrt{((dm)^2 + (dx)^2)}$$

- Total reported mass of ice/liquid melt:

$$z = q1 + q2 + q3 + q4 + q5$$

- Uncertainty in total reported mass of ice/liquid:

$$dz = \sqrt{((dq1)^2 + (dq2)^2 \ldots + (dq5)^2)}$$

- Change in sample mass: $w = Initial\ mass\ (u) - Final\ mass\ (v)$

- Uncertainty in sample mass change:

$$dw = \sqrt{((du)^2 + (dv)^2)}$$

- Cold trap efficiency:

$$e = \frac{z}{w}$$

- Uncertainty in cold trap efficiency:

$$de = e \times \sqrt{\left(\left(\frac{dz}{z}\right)^2 + \left(\frac{dw}{w}\right)^2\right)}$$

3.2.13. Limitations. The maximum temperature achievable by the system during experiments ranged from 658^0C to 670^0C. As a result, total decomposition of the samples was not achieved and some of the volatiles potentially available in each sample remained intact. The major reason was radiative heat loss from the furnace. A constant heating rate of 400^0C/hour was maintained during all temperature ramps besides the ramp to the final plateau when the furnace struggled to achieve the set rate, this makes comparisons between the pressure trace derived from this point with those obtained during previous plateaus difficult. Another limitation was caused by the use of liquid nitrogen (LN_2) as the active coolant in the cold trap, which only cools the trap surface to -196^0C in the best case. This means gases with freezing points below this threshold could not be captured. The gases that were not collected for this reason are herein termed 'un-trappable'. Gaseous compounds such as carbon monoxide fall within this category. Additionally, for those gas species with freezing points close to the operating threshold, the efficiency of removal by freezing was decreased.

4. RESULTS AND DISCUSSION

Data is presented in the following sections from the experiments conducted on bulk samples of olivine, serpentine, and different forms of the Orgueil simulant as discussed in Section 3. A brief narrative of each test is supported by derived pressure-temperature profiles. While each experiment was different in some aspects, a strongly repeatable pattern of volatile release is evident from temperature/pressure/time profiles, from an analysis of gas yield as a function of increasing temperature, and from the thermal behavior of materials tested. Table 4.1 summarizes the obtained results and lists the experiments discussed in this chapter in their order of occurrence. 'CLASS' refers to a sample of the granular Orgueil simulant, 'CLASSbrick' refers to a sample of the consolidated variety while 'Serp' and 'Oliv' refer to samples of granular serpentine (lizardite) and olivine (forsterite) respectively. Samples were heated radiatively by heat transfer from the furnace heating elements to the exposed surface area and then by conduction through the material. Convective heat transport becomes a factor during episodes of gas release.

Experiments are discussed in terms of gas evolution patterns, the nature of gases produced and the amount of product recovered as an icy material on the cold trap. Measures of cold trap efficiency at retrieving products are presented alongside estimates of overall recovery and extraction efficiency which rely on earlier thermogravimetric results of the amount of producible gas contained within each sample type. Samples utilized are placed in two major groups:

a) Group A: Consisted of effectively single mineral serpentine (lizardite) and olivine (forsterite) samples included to evaluate the sensitivity of the experimental setup.

b) Group B: Consisted of granular and consolidated Orgueil simulant samples tested as analogs for the carbonaceous, volatile-bearing solar system bodies of interest.

4.1. GROUP A: SINGLE MINERAL TESTS

The single mineral experiments that are the most appropriate for comparison to the Orgueil simulant tests are hereby presented.

4.1.1. Serp #4. This experiment was run over a period of about 96 hours. The length of individual plateaus ranged from 20-24 hours, and this sample was heated to a maximum temperature of ~608^0C. The manner of sample temperature rise and accompanying gaseous release is shown by the temperature-pressure profile in Figure 4.1. Chamber pressure rises as rising sample temperature causes gas release as furnace temperature is ramped to the next plateau. After the initial spike in pressure corresponding to the initial spike in sample temperature reaches its peak, pressure progressively falls as temperature moves more slowly through the material producing less gas than during rapid temperature rise. The spikes in chamber pressure during the first two plateaus are a result of cycling in cold trap temperature. As it warmed some previously frozen molecules were remobilized increasing pressure and as it cooled, this gas was re-trapped returning pressure to a base level. This cycling was eliminated over the final plateaus and accordingly the spiking disappeared from the pressure curves. However, the furnace briefly lost power during the final plateau, leading to an immediate drop in chamber pressure that rose back to former levels soon after the furnace was re-set.

These interactions point to the chamber pressure profile as a suitable proxy for mass release rate during the course of a test. The disparity between sample and furnace

temperature over the final two plateaus is may be due to the presence of a temperature gradient within the furnace and/or the cooling effect of the endothermic release of volatiles on samples.

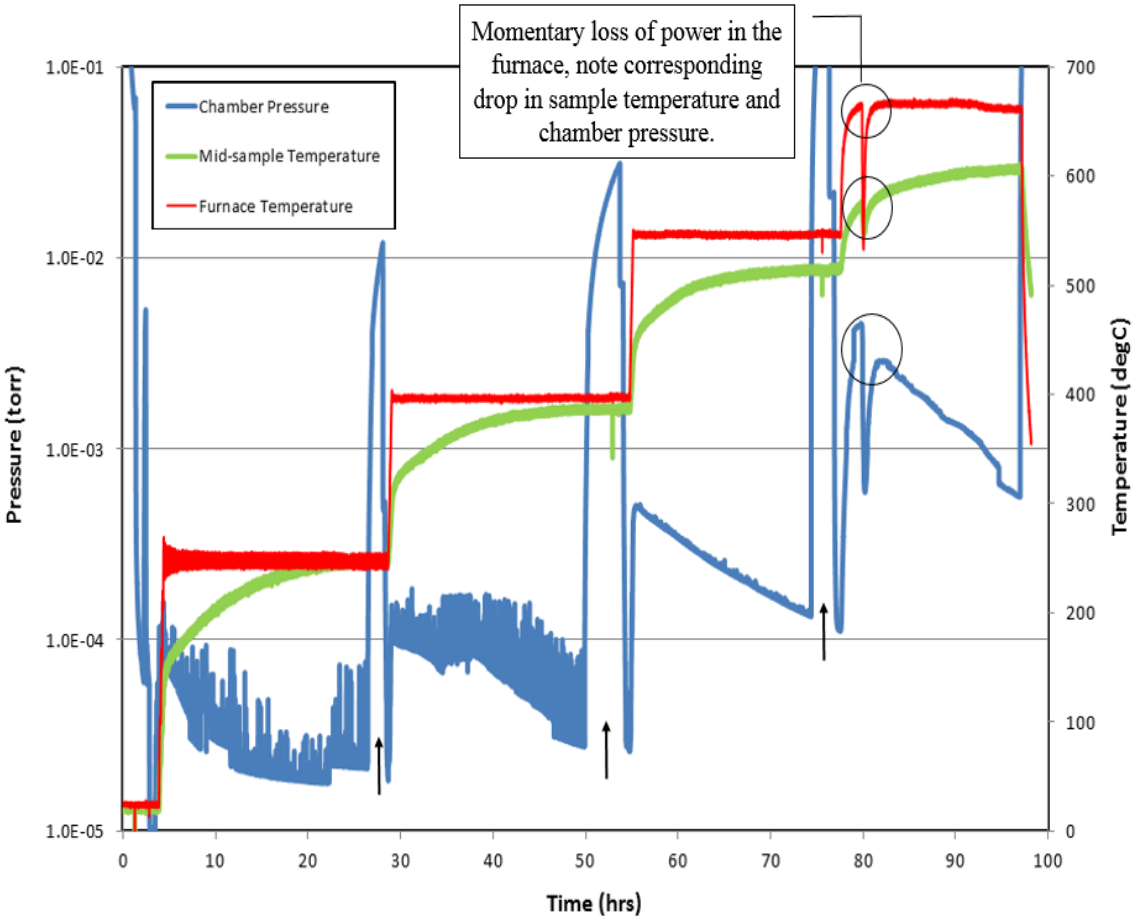

Figure 4.1. Pressure-Temperature Profile for Serp #4. (Primary Vertical Scale Showing Pressure is a Log-Scale, Up-Pointing Black Arrows Show Periods of Sustained Pressure Rise In-between Plateaus When System is Isolated from Vacuum Pumps).

Figure 4.2 shows this sample in its mesh container seated on the sample tray and ready to be put into the furnace while Figure 4.3 shows the icy material that was collected after various stages of this experiment.

Figure 4.2. Serp #4 Before the Start of Heating.

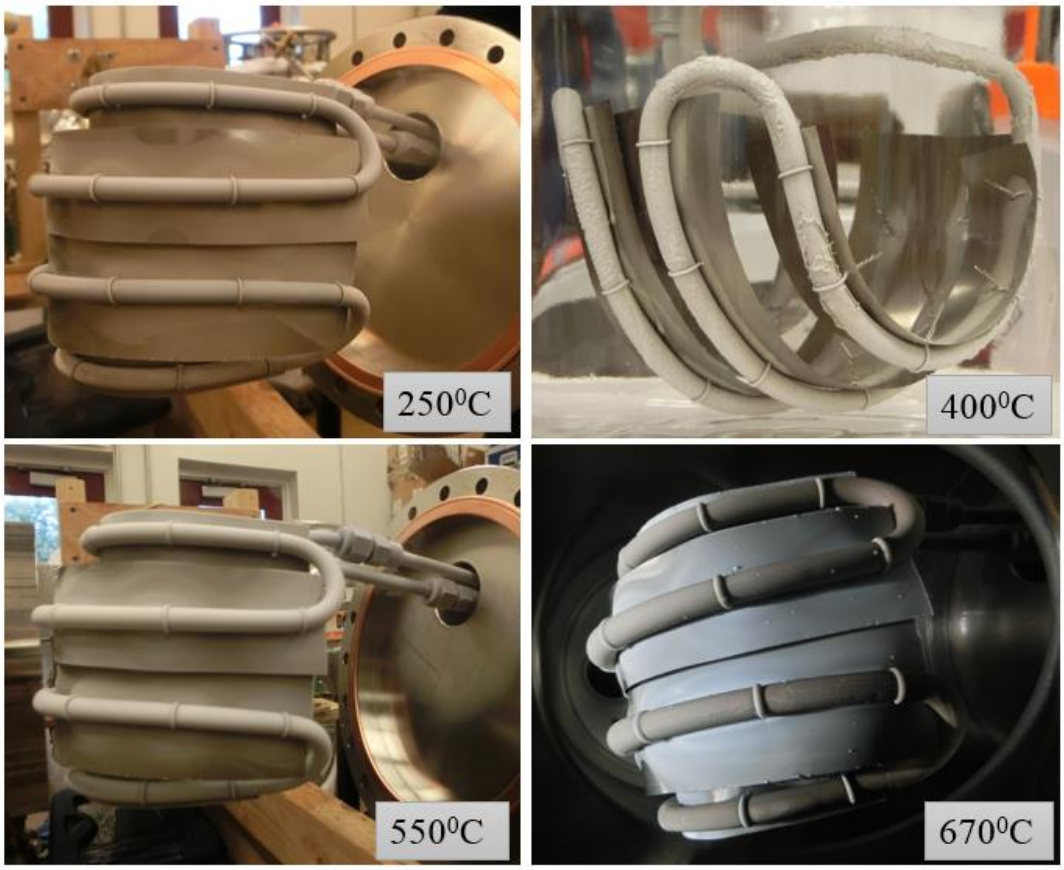

Figure 4.3. Icy Material Collected During Serp #4.

4.1.2. Oliv #3. Figure 4.4 shows the prepared Oliv #3 sample sitting within the furnace, note sheathed thermocouples going in through the top. This sample was more densely packed than the serpentine as a result of the physical nature of its crushed particles (see Table 4.1). The derived pressure curves in Figure 4.5 show a lower peak magnitude for the most productive plateaus when compared to curves derived from the serpentine test (Figure 4.1). This indicates that less gas was released from this sample type. Over an experiment that lasted for approximately 95 hours, four temperature plateaus were held, each for 20-24 hours and the sample averaged a maximum temperature of about 640^0C at the final step. Less gas produced at this stage meant less cooling and endothermic reactions allowing sample temperature to rise to a higher level than what was achieved during the serpentine test. During the second plateau, an increase in cold trap temperature temporarily led to a spike in chamber pressure as previously frozen out gas was remobilized in the system. The general trend of mass release shown by the chamber pressure curve is maintained. Figure 4.6 shows the sample after being heated and removed from the chamber while Figure 4.7 shows the nature of the icy material collected.

Figure 4.4. Oliv #3 Before the Start of Heating.

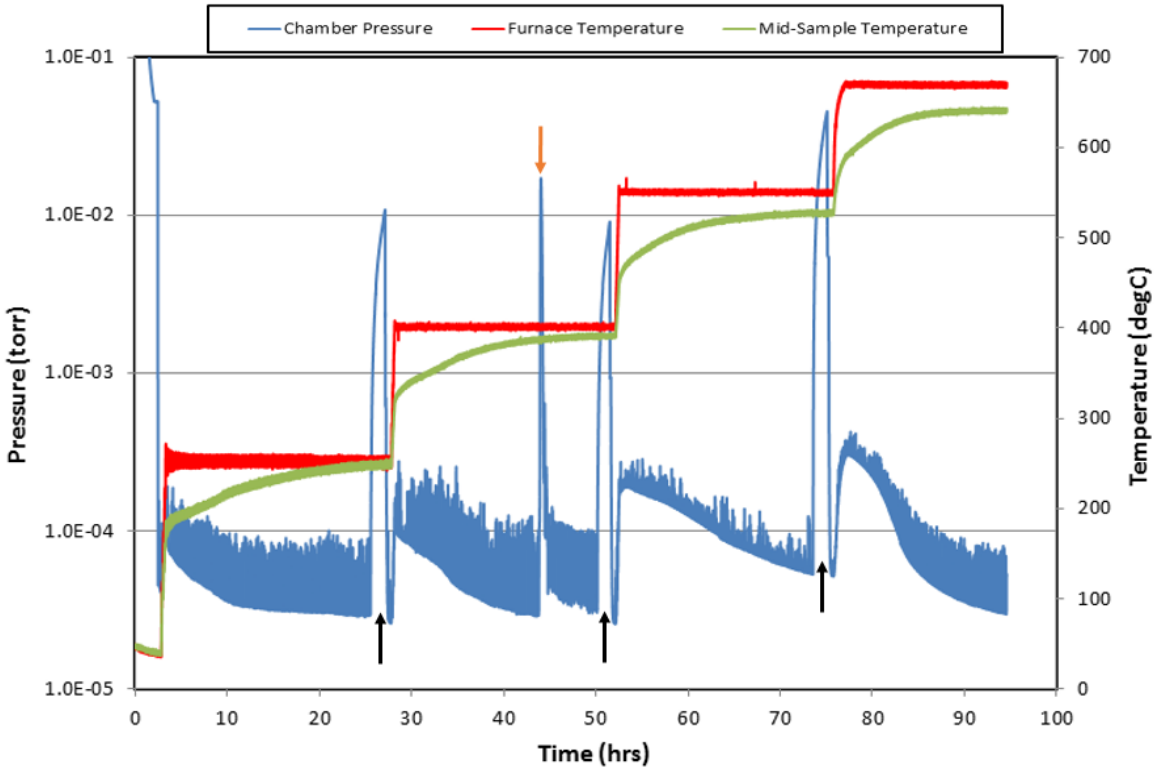

Figure. 4.5. Pressure-Temperature Profile for Oliv #3. (Primary Vertical Scale is a Log-Scale, Up-Pointing Black Arrows Show Periods of Sustained Pressure Rise In-between Plateaus when System is Isolated from Vacuum Pumps, Down-Pointing Orange Arrow Shows Effect of Coolant Loss at Cold Trap).

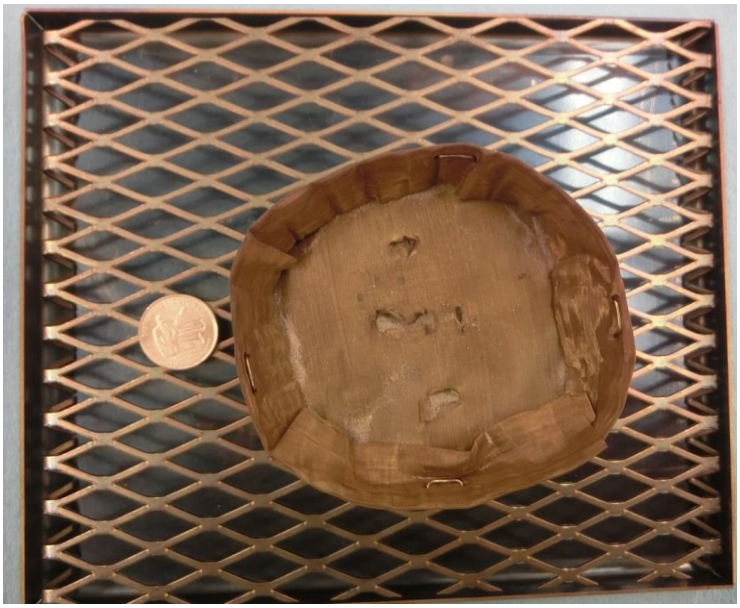

Figure 4.6. Oliv #3 at the Conclusion of Testing.

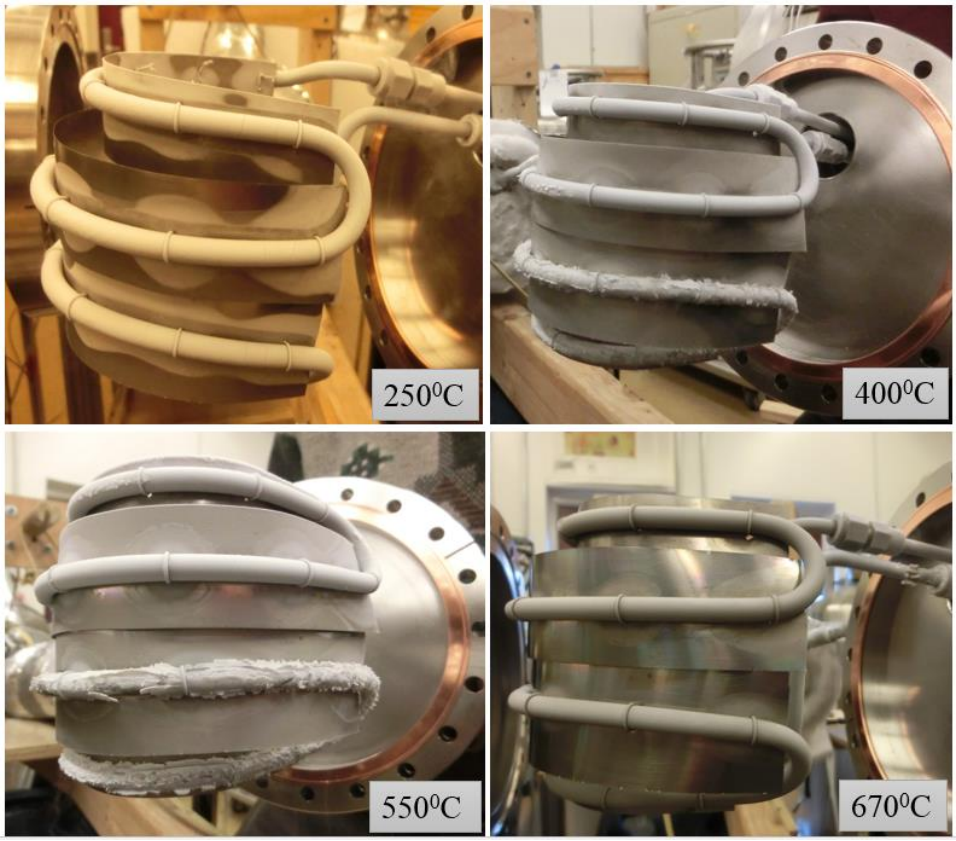

Figure 4.7. Icy Material Collected During Oliv #3.

4.2. GROUP B: ORGUEIL SIMULANT TESTS

Three samples each of granular and consolidated forms of this sample type were tested. Similarities in mineralogy meant that similar gas compounds were produced over similar temperature ranges. For the consolidated form, the possibility of greater residence time of extracted volatiles within the bulk mass existed especially if it were characterized by a more tortuous path of gas escape. This could lead to the occurrence of gas-phase reactions that may in turn affect the nature of recovered products. Radiative heat transfer from the heating elements in the furnace was constant for all tests but conduction across differed due to differences in porosity and bulk density; hence, variation in thermal

conductivity between these 2 forms was expected. Convective heat and mass transport was important during diffusion through the bulk mass. A tortuous path of gas escape could also lead to the build-up of internal pore pressure that could conceivably cause spalling if it had a high enough magnitude. Details of results from experiments on different forms this class of sample are presented in the following sections.

4.2.1. CLASS #1. In the sequence of tests presented, this was the first experiment run. At the time the vacuum setup was being run as a truly closed system without the benefit of active pumping from the turbo molecular pump during the course of the test. The pressure-temperature profile shown in Figure 4.8 highlights the issue of background and 'un-trappable' gases (note that the vertical scale is different from that of two previous Figures). Pressure within the system rose from high vacuum levels once the vacuum pumps were isolated and closed off to the system, even before heat was actively applied as background gases were released from chamber surfaces. With a sample in the chamber and at elevated temperature, this rate of rise was increased especially as the sample released species that were 'un-trappable' by the cold trap. This persistent rise in pressure created experimental difficulties as the chamber had to be pumped out once it rose past pre-determined levels. Excessively high pressures could cause arching of the furnace electronic components, condensation of gas on surfaces, and could adversely affect heat conservation within the system as convective heat transfer is introduced. Also, high pressures reduce the positive pressure gradient generated by vacuum for outward flow of volatiles.

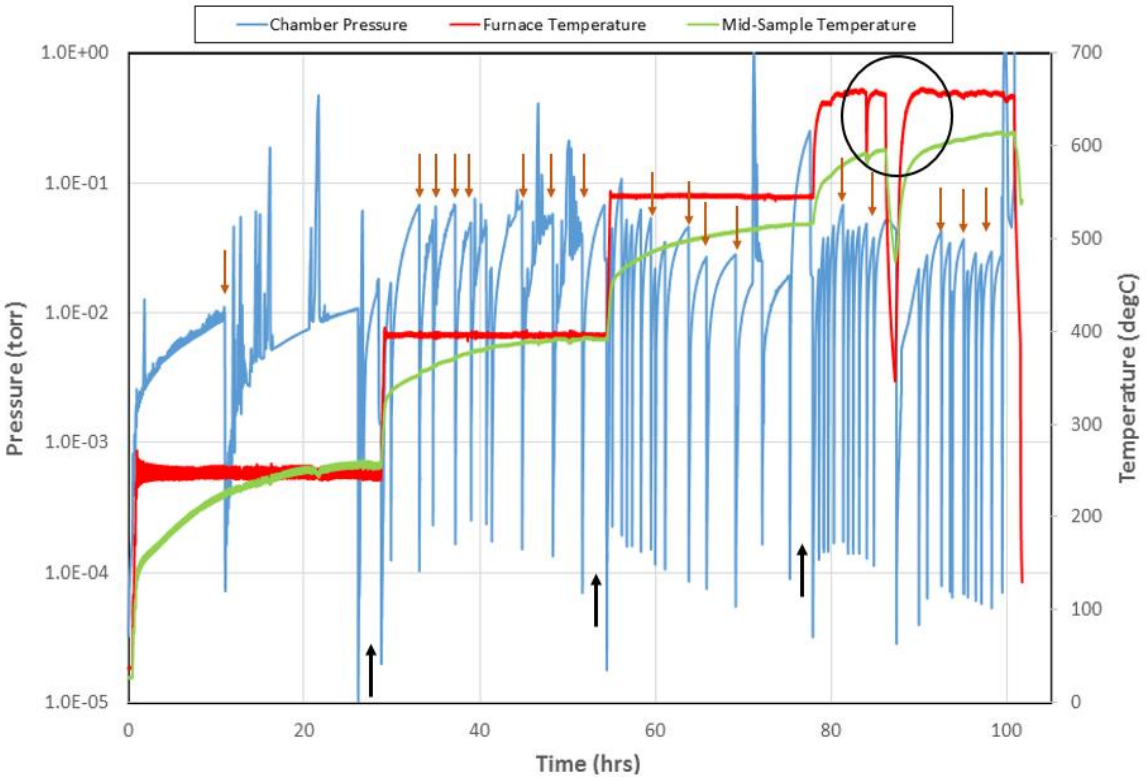

Figure 4.8. Pressure-Temperature Profile for CLASS #1. (Primary Vertical Scale Showing Pressure is a Log-Scale, Up-Pointing Black Arrows Show Periods of Sustained Pressure Rise In-between Plateaus when System is Isolated from Vacuum Pumps, Down-Pointing Orange Arrows Show Repeated Pump-Out Periods, Circle Marks Points of Furnace Shut-Down).

The orange arrows in Figure 4.8 point at some of these pump-out periods each characterized by an abrupt drop in pressure. Note how the need for these periods became more frequent during the final two plateaus which were the most productive in terms of gas release. The furnace lost power on two occasions during the final temperature plateau (marked by circle). This experiment was also run without an initial period where the sample is kept under vacuum while cryo-trapping is carried out. This negatively affected calculated cold trap efficiency (refer to Table 4.1). The prepared sample and its physical measurements are presented in Figure 4.9 and Table 4.1 while the nature of the icy material collected is shown in Figure 4.10.

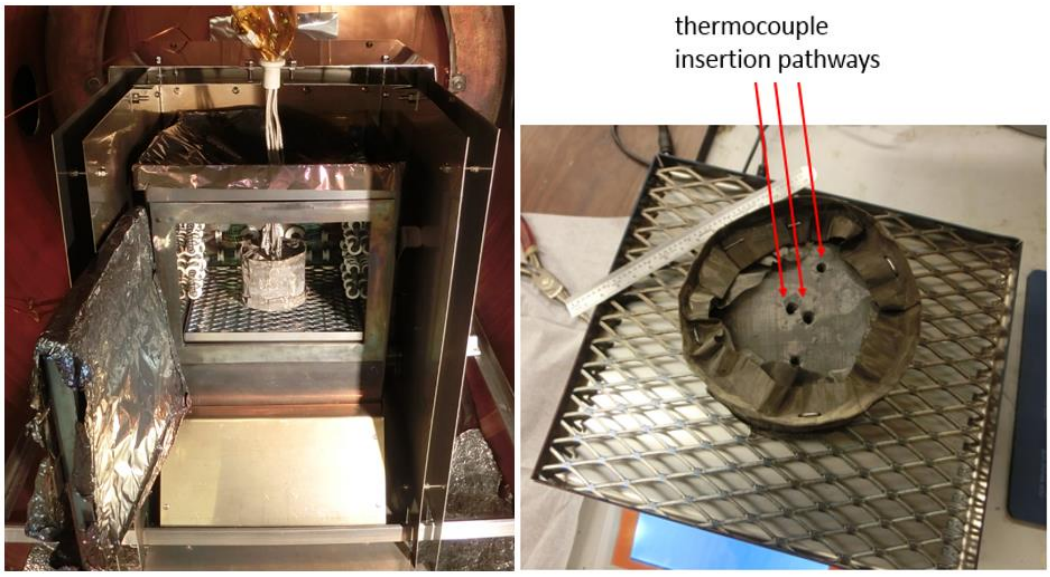

Figure 4.9. Prepared CLASS #1.

Figure 4.10. Icy Material Collected During CLASS #1.

4.2.2. CLASS #2. After considering lessons revealed by preliminary results from the first granular Orgueil simulant test (CLASS #1), the experimental procedures were adjusted to include a step where the cold-trap was frozen at some point during the initial stage of pump-down (with the sample in the chamber) that takes place before heat is actively applied in order to evaluate how much gas extraction occurs at this time. During this ~24 hour period, sample temperature reached ~45^0C while chamber pressure was maintained in the $1x10^{-2}$ torr range. At the end, the icy material recovered on the trap is weighed and sampled. Also, active throttled turbo-pumping (described in section 3.1.6) was adopted which allowed for the creation of much more informative pressure-temperature profiles (see Figure 4.11). Images of the prepared sample and its physical measurements are presented in Figure 4.12 and Table 4.1 respectively.

The heating experiment ran for ~120 hours. Each plateau was held for 20-24 hours with the exception of the first which it took more time for conditions to meet the established criteria. The sample achieved an average maximum final temperature of 611^0C. The general trend of a steep pressure rise followed by a slower subsequent fall is maintained over the course of a temperature plateau. The major spike in chamber pressure that occurred during the second plateau and around the 56^{th} hour was the result of a sustained loss of cooling at the cold-trap, smaller spikes were the result of fluctuations in cold-trap operating temperature. The cooling effect of volatile production contributes to the disparity between sample temperature and furnace control temperature during the final temperature plateau. Figure 4.13 presents images of the icy material collected during this test.

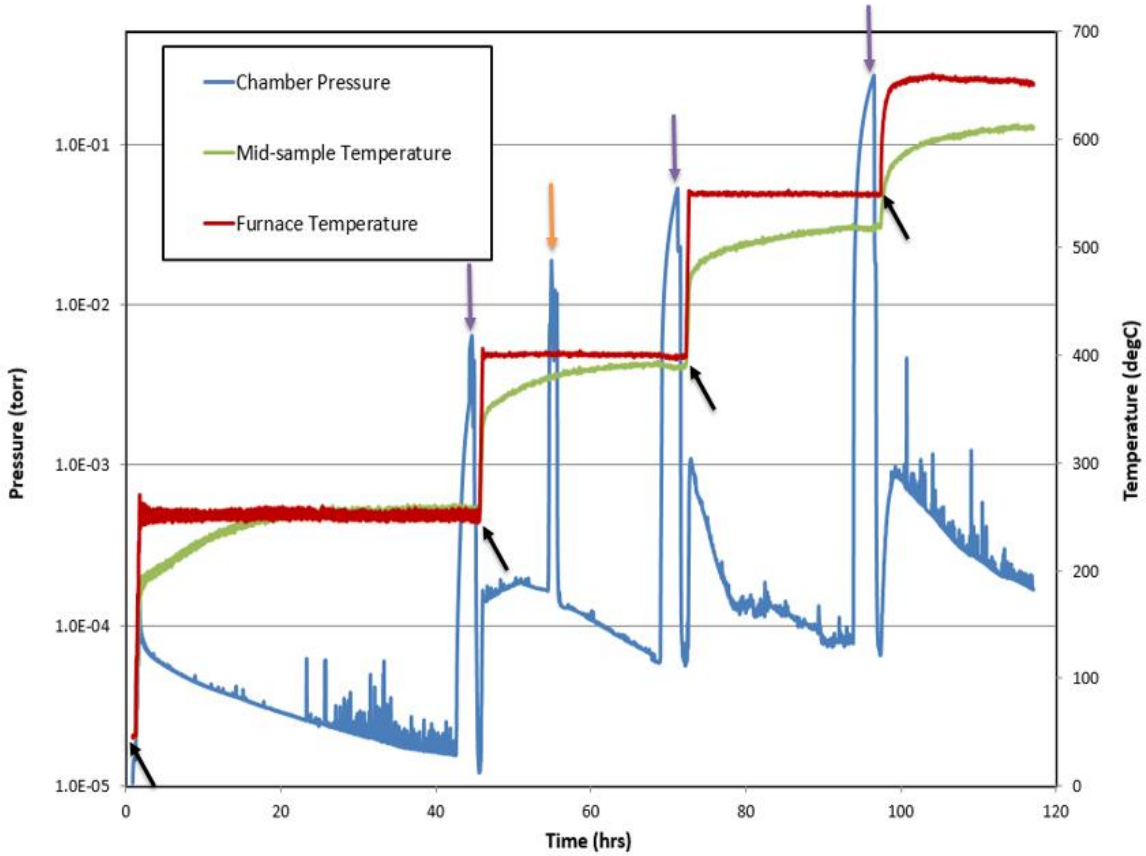

Figure 4.11. Pressure-Temperature Profile for CLASS #2.

Figure 4.12. Prepared CLASS #2.

Figure 4.13. Icy Material Collected During CLASS #2.

4.2.3. CLASS #3. Figure 4.14 shows the pressure-temperature profile derived from this test. Again, plateaus are held from between 20-24 hours with the exception of the first where it took longer for conditions to meet set criteria. The experiment lasted for a total of about ~140 hours with the sample achieving a maximum temperature of ~602^{0}C at the final temperature step. The general trend between sample temperature and chamber pressure seen in previous tests is maintained. Relatively sustained pressure spikes that occurred, once during the first temperature step and twice during the third step were a result of a loss of cooling at the cold-trap. The cooling effect of de-volatilization continues to contribute to the disparity between sample and furnace temperature at the final step. The prepared

sample and its physical measurements are presented in Figure 4.15 and Table 4.1 respectively. The nature of the icy material collected is presented in Figure 4.16.

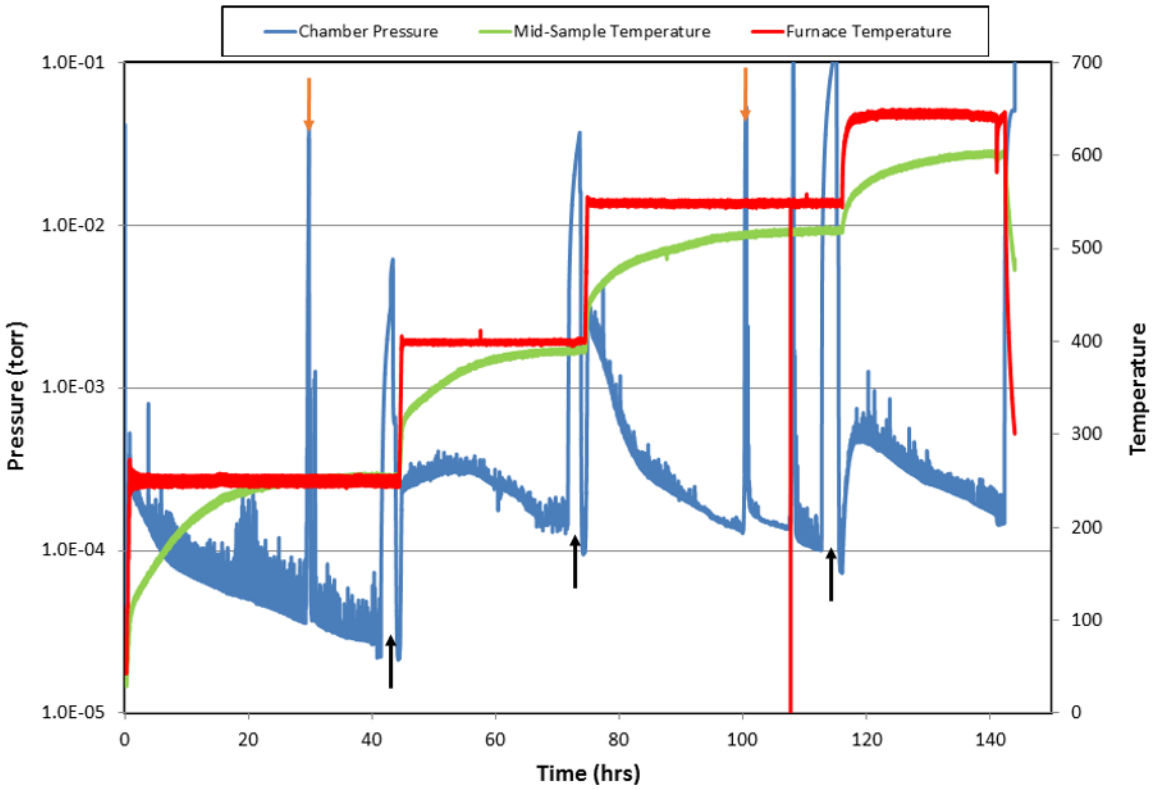

Figure 4.14. Pressure-Temperature Profile for CLASS #3.

Figure 4.15. Prepared CLASS #3.

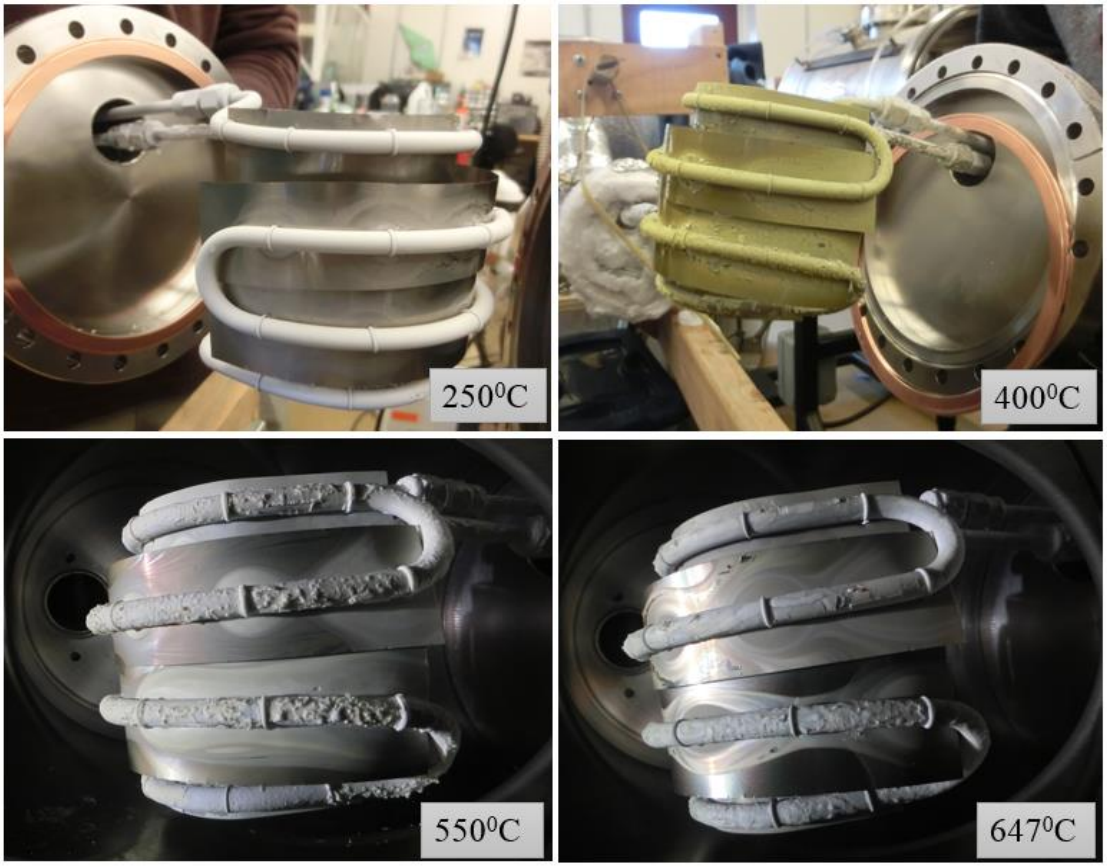

Figure 4.16. Icy Material Collected During CLASS #3.

4.2.4. CLASSbrick #1. Figure 4.17 and Table 4.1 show the prepared sample and its physical measurements. Figure 4.18 shows the pressure-temperature profile derived from this experiment. As per procedures, heat was applied in four steps with each lasting for 18-23 hours. The sample achieved a maximum temperature of 645^{0}C at the final stage. The general trend of pressure change with increasing sample temperature during a plateau is maintained, however the pace of heat rise through the consolidated mass was considerably quicker than what was observed in tests on the granular form.

Accordingly, the characteristic chamber pressure rise and fall over the course of a temperature plateau was also quicker. Momentary pressure excursions were due to a momentarily warm cold trap which was quickly returned to its normal operating

temperature. A shortage of LN_2 at the conclusion of the 400^0C plateau caused the test to be kept in a holding mode for ~48 hours. During this time, furnace temperature was dropped to 280^0C while chamber pressure held at ~$1x10^{-2}$ torr. To restart the experiment, furnace temperature was brought back and held at 400^0C to allow sample temperature to equilibrate at former levels before ramping the furnace to the 550^0C plateau.

Figure 4.17. Prepared CLASSbrick #1.

Sample temperature got much closer to furnace control temperature in this test compared to tests on the granular simulant suggesting that discrepancies seen were probably also influenced by packing density and thermocouple contact with material grains. Figure 4.19 shows the icy material collected.

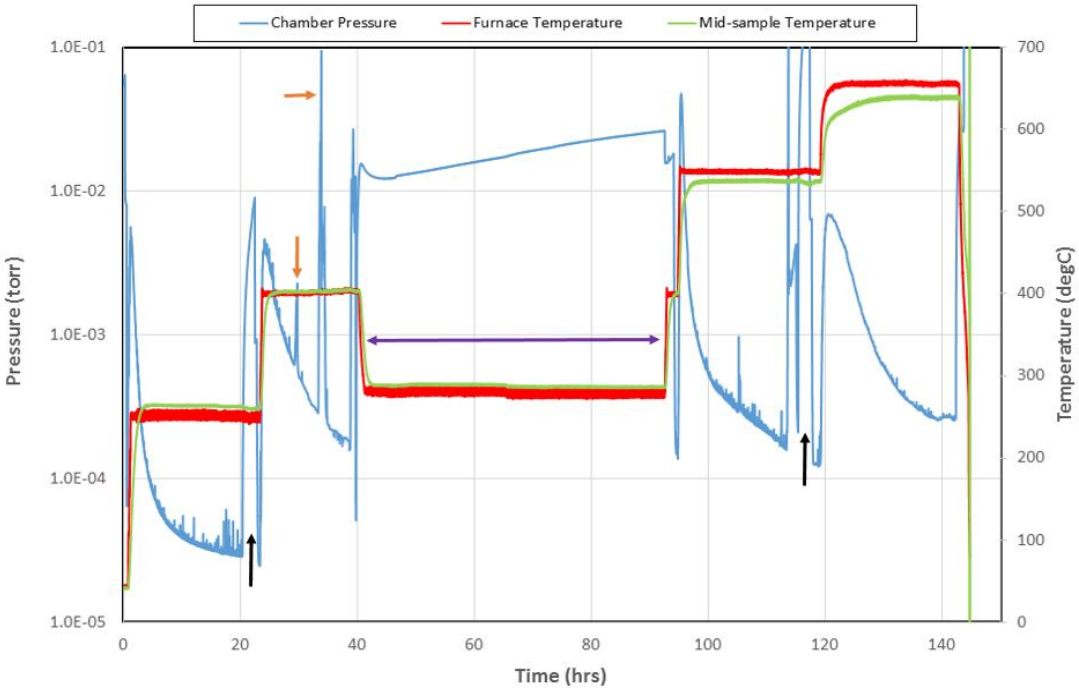

Figure 4.18. Pressure-Temperature Profile for CLASSbrick #1. (Purple Arrow Shows Holding Period).

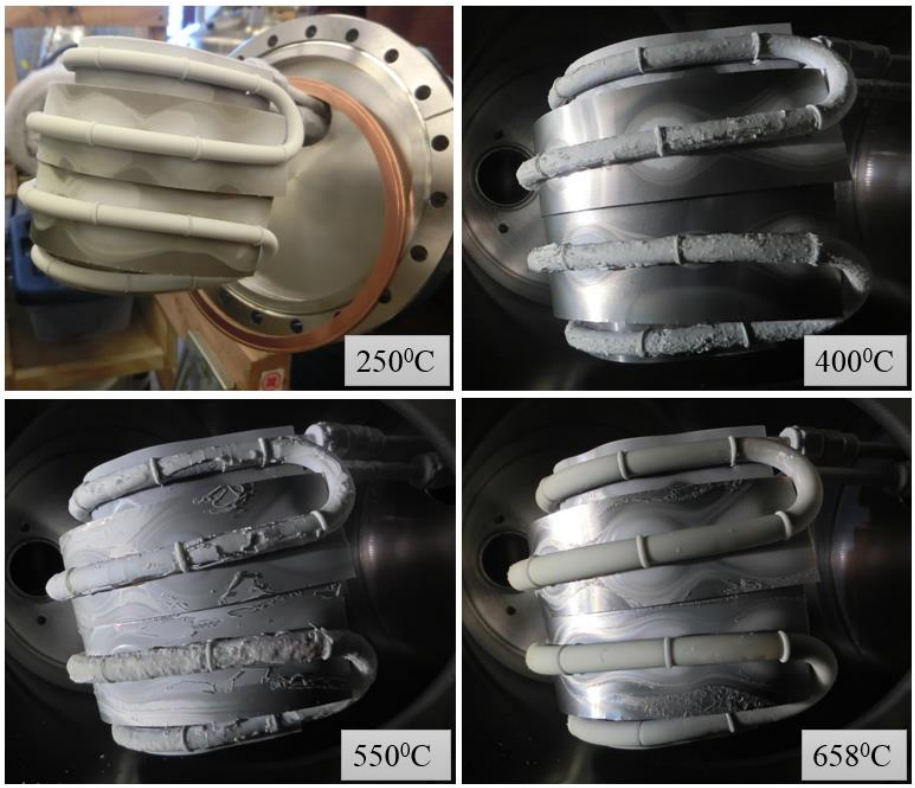

Figure 4.19. Icy Material Collected During CLASSbrick #1.

4.2.5. CLASSbrick #2. Figure. 4.20 shows the temp-pressure profile derived from this experiment. The sample achieved a maximum temperature of 619^0C at the final step. After the 250^0C plateau was concluded, the experiment was suspended in a holding mode due LN_2 supply issues. During this ~48 hour pause, furnace temperature was dropped to ambient and the sample was kept under vacuum. Pressure rise at this time was the result of the natural system leak-up which occurs when the system is kept at low pressure without active pumping rather than any outgassing from the sample.

The experiment was restarted by bringing temperature in the furnace back up to 250^0C and allowing sample temperature to equilibrate, before ramping up to the next temperature step. Pressure spikes during the course of a plateau were the result of a warming cold trap. There was a greater discrepancy between sample and furnace temperature at the highest 2 temp steps, somewhat similar to what was observed during tests on the granular simulant. This may be due to the thermocouple reading temperature from a location with minimal packing density such as a fracture allowing it to be more affected by the cooling effect of gas release. This particular sample shown in Figure 4.21 was intensely fractured and broke apart while it was being set-up.

It was supported in an upright position within the furnace by use of a piece of SS mesh. Table 4.1 presents approximate physical measurements of this sample while Figure 4.22 shows the nature of the icy material collected which was broadly consistent with what was obtainable from the class simulant tests with the first, the third and the final temperature plateau being the most productive in terms of gas release. This experiment ran for a total of ~160 hours including the holding period.

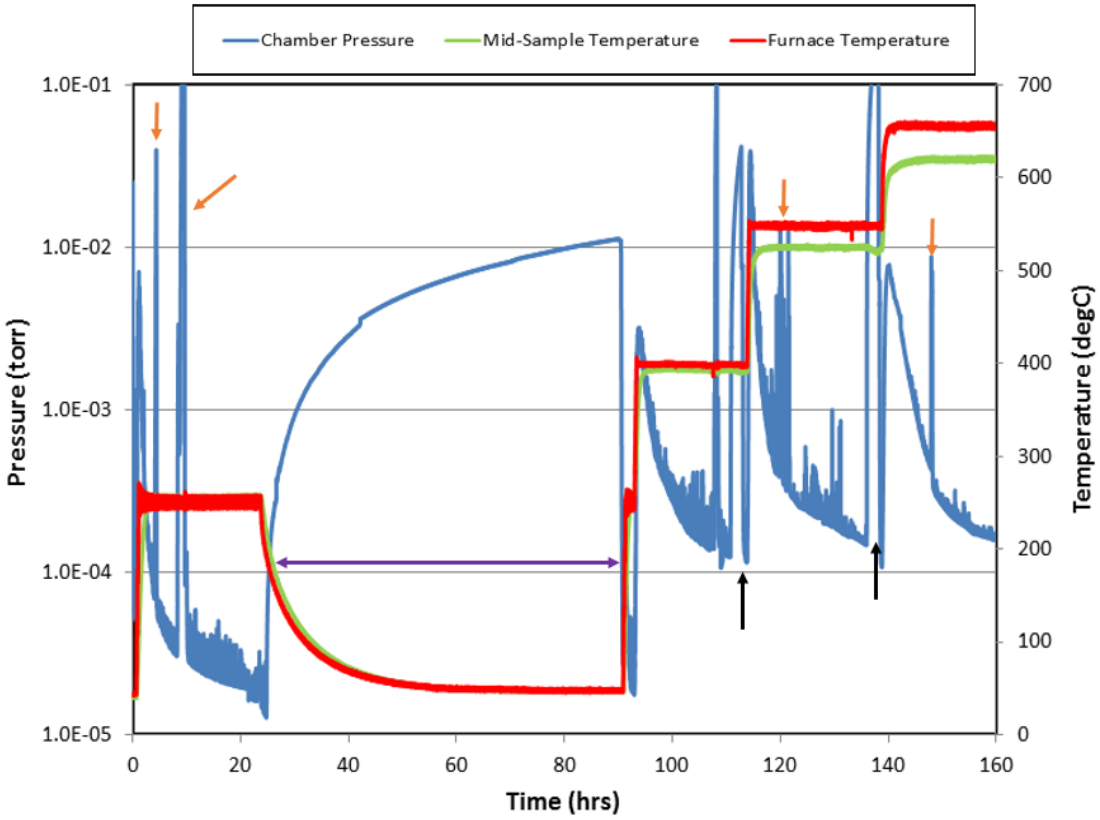

Figure 4.20. Pressure-Temperature Profile for CLASSbrick#2. Black Arrow Indicate Period between Plateaus, While Orange Arrows Show Anomalous Episodes.

Figure 4.21. Fractured CLASSbrick #2.

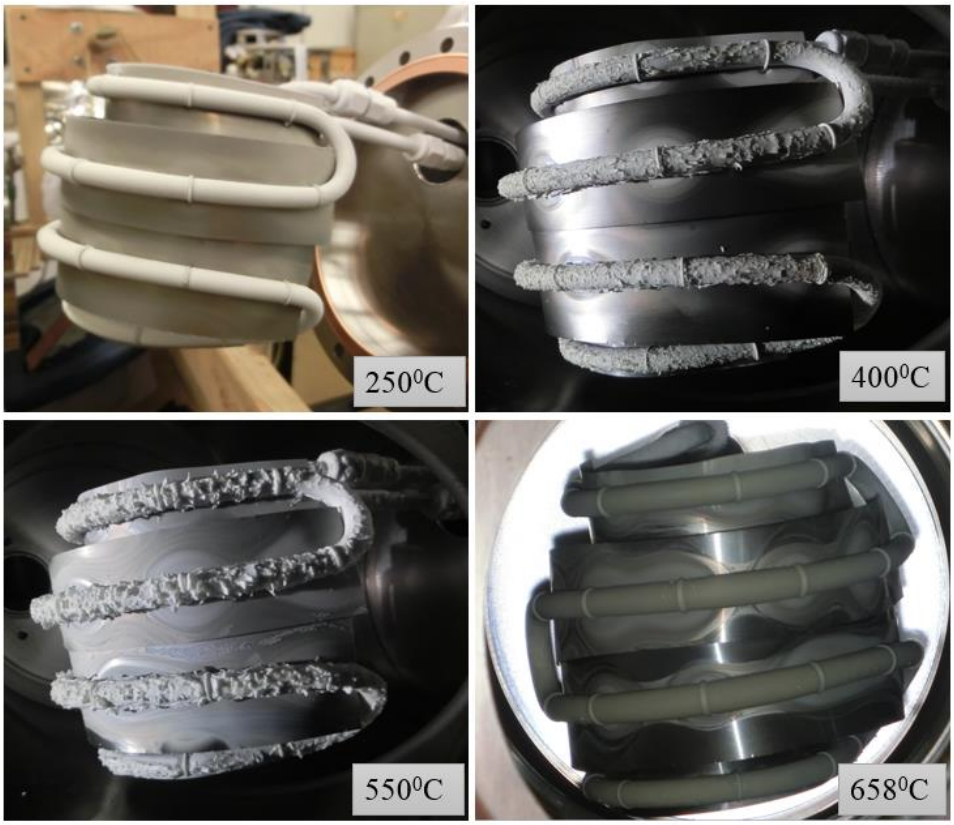

Figure 4.22. Icy Material Collected During CLASSbrick #2.

4.2.6. CLASSbrick #3. Figure 4.23 shows the prepared sample ready to be tested. Figure 4.24 shows the pressure-temperature profile derived during this experiment. This experiment ran for a total of ~95 hours with each of four temperature plateaus lasting between 20-22 hours. The sample achieved a maximum temperature of 645^{0}C at the final step. The general pattern of pressure rise with increasing sample temperature was maintained. The pressure spike just before the end of the 550^{0}C plateau was as a result of a warming cold trap. This sample was similar to CLASSbrick #1 in terms of fracture/void density and this was reflected in the relatively low discrepancy between sample and furnace temperature at the highest temperatures. Figure 4.25 shows the nature of the icy material collected during this experiment.

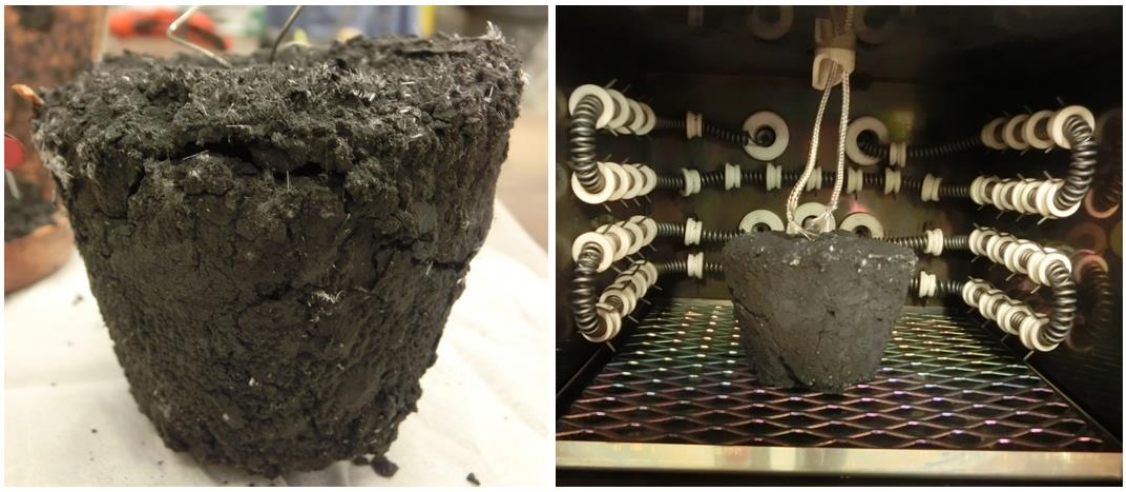

Figure 4.23. Prepared CLASSbrick #3.

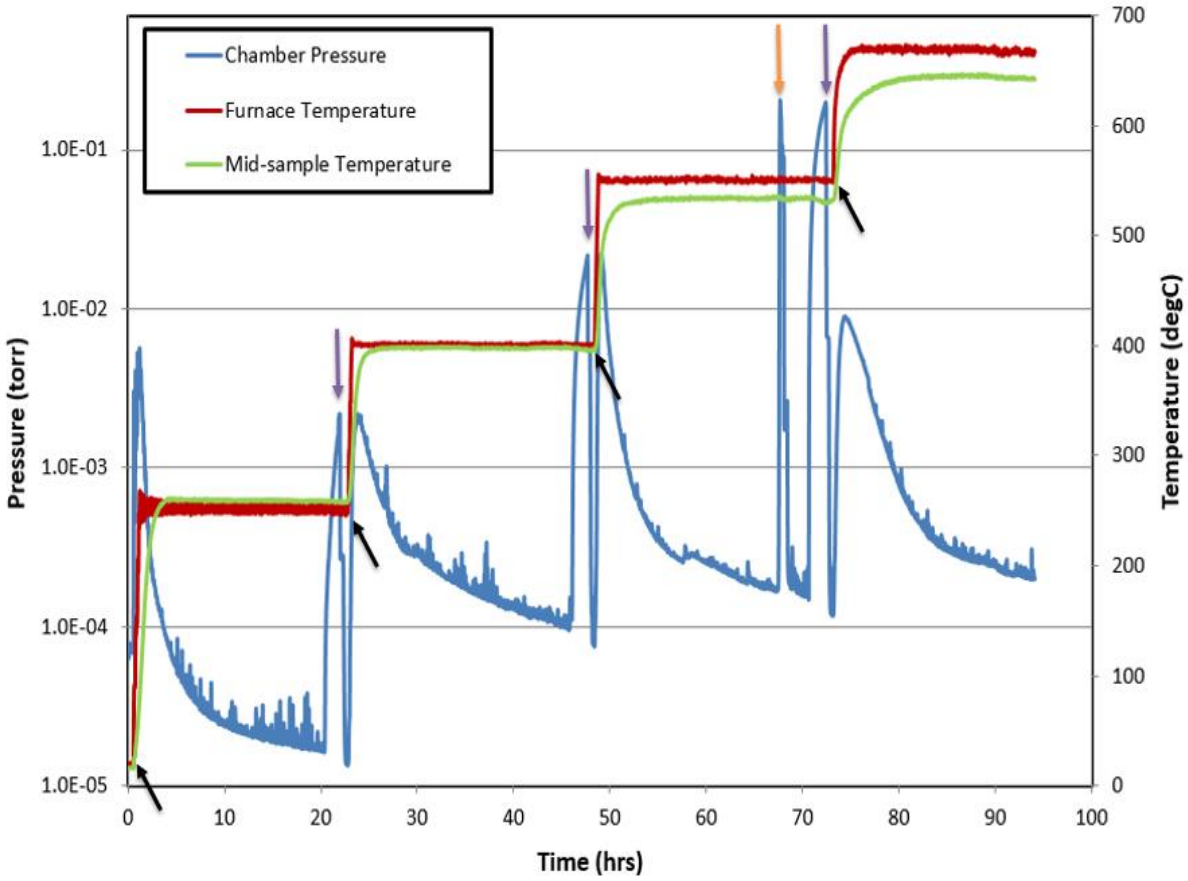

Figure 4.24. Pressure-Temperature Profile for CLASSbrick #3. Black Arrows Indicate Start of Heat Ramp, Purple Arrows Indicate Time between Plateaus, While Purple Arrow Points at an Anomalous Period.

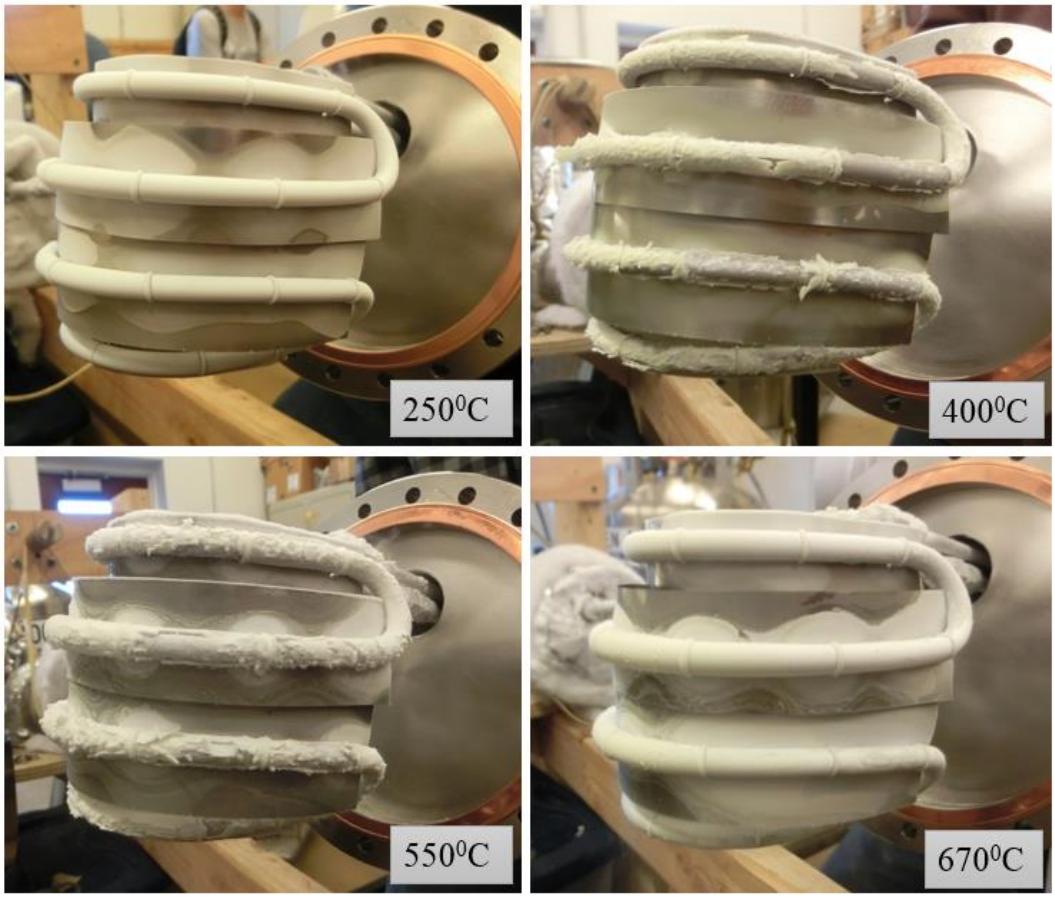

Figure 4.25. Icy Material Collected During CLASSbrick #3.

4.3. DISCUSSION OF RESULTS

Results presented in the following sections are discussed in terms of heating and volatile release behavior, gas species produced, the icy material recovered and the implications of cold trap efficiency and recovery estimations. Table 4.1 presents a concise summary of the results that were obtained and estimated, tests are listed in the order in which they occurred with the CLASS #1 being the first and Oliv #3 the last in this sequence. Note the higher densities of the consolidated orgueil simulant samples in comparison to simulant samples in granular form.

Table 4.1. Summary of Sample Physical Properties and Derived Experimental Results. Presented in the Order in Which Tests Were Conducted.

Sample ID	Shape	Approx. Height (cm)	Approx. Diameter (cm)	Approx. Bulk Density (g/cm^3)	Initial Mass (g)	Final Mass (g)	Change in Sample Mass (g)	Total mass of Ice Collected (g)	Total Mass of Liquid Melt (g)	Cold Trap Efficiency (%)	Extraction Efficiency (%)	Recovery (%)	Major Species Produced
CLASS #1	Cylindrical	7.6	8.2	1.0	401.0 ± 0.1	359.4 ± 0.1	41.6 ± 0.1	26.1 ± 0.8	7.6 ± 0.8	62.7 ± 1.9	53.0	34.0	H_2O, CO_2, S_2, CH_4, CO
Serp #4	Cylindrical	8.4	8.4	1.1	501.2 ± 0.1	456.0 ± 0.1	45.2 ± 0.1	45.3 ± 0.8	44.4 ± 0.8	100.2 ± 1.8	79.0	78.2	H_2O
CLASS #2	Cylindrical	7.0	7.5	1.3	401.0 ± 0.1	361.5 ± 0.1	39.5 ± 0.1	37.3 ± 0.9	31.3 ± 0.9	94.4 ± 2.3	51.0	48.0	H_2O, CO_2, S_2, CH_4, CO
CLASSbrick #1	Truncated Cone	6.0	Top = 8.5; Bottom = 5.0	1.8	497.0 ± 0.1	412.4 ± 0.1	84.6 ± 0.1	77.9 ± 0.9	69.9 ± 0.9	92.1 ± 1.1	72.0	67.0	H_2O, CO_2, S_2, CH_4, CO
CLASS #3	Cylindrical	7.3	7.5	1.2	400.5 ± 0.1	361.4 ± 0.1	39.1 ± 0.1	33.5 ± 0.9	26.3 ± 0.9	85.7 ± 2.3	50.0	43.0	H_2O, CO_2, S_2, CH_4, CO
CLASSbrick #2	Truncated Cone	6.0	Top = 8.5; Bottom = 5.0	1.8	472.7 ± 0.1	402.5 ± 0.1	70.2 ± 0.1	57.3 ± 0.9	48.4 ± 0.9	81.6 ± 1.3	63.0	52.0	H_2O, CO_2, S_2, CH_4, CO
CLASSbrick #3	Truncated Cone	6.0	Top = 8.5; Bottom = 5.0	1.8	487.8 ± 0.1	402.4 ± 0.1	85.4 ± 0.1	68.2 ± 0.9	62.2 ± 0.9	79.9 ± 1.1	74.0	59.0	H_2O, CO_2, S_2, CH_4, CO
Oliv #3	Cylindrical	6.1	7.4	1.9	502.0 ± 0.1	493.0 ± 0.1	9.0 ± 0.1	8.5 ± 0.9	6.4 ± 0.9	94.4 ± 10.1	126.0	113.0	H_2O

4.3.1. Single-Mineral Granular Samples. Serpentine and olivine samples produced a relatively similar trend of gas release following ramps in furnace temperature. As with other samples, this trend appears to have been controlled by heat transport through the material. Sample temperatures quickly achieved ~40-50% of its ultimate plateau maximum for all granular samples (Figure 4.26) after furnace temperature was ramped upwards. This quick rise was consequently followed by a rapid release of gas that caused a corresponding spike in chamber pressure. After furnace temperature reached a plateau maximum, temperature rise in the material slowed down and spent the remaining time at that temperature plateau in a slow climb toward its final temperature. Figure 4.27 shows the mass fraction of icy material (calculated as a percentage of the initial mass of the sample) recovered during single mineral tests at the end of each temperature plateau.

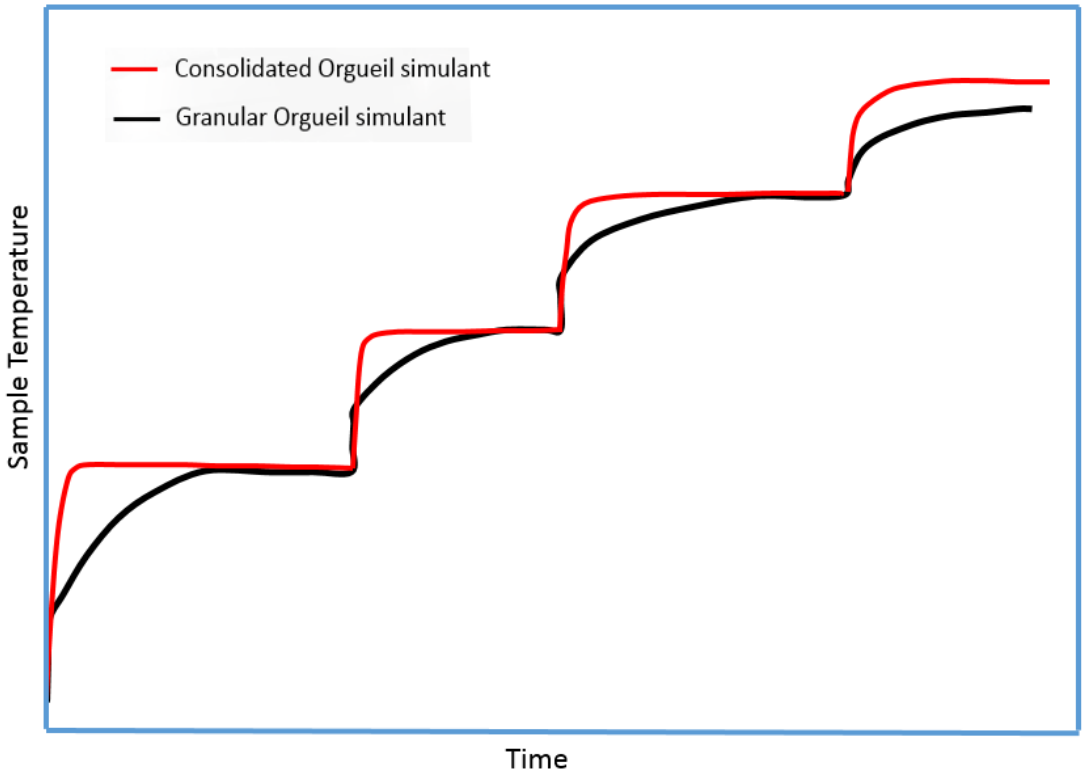

Figure 4.26. Schematic Comparing the Nature of Heat Rise.

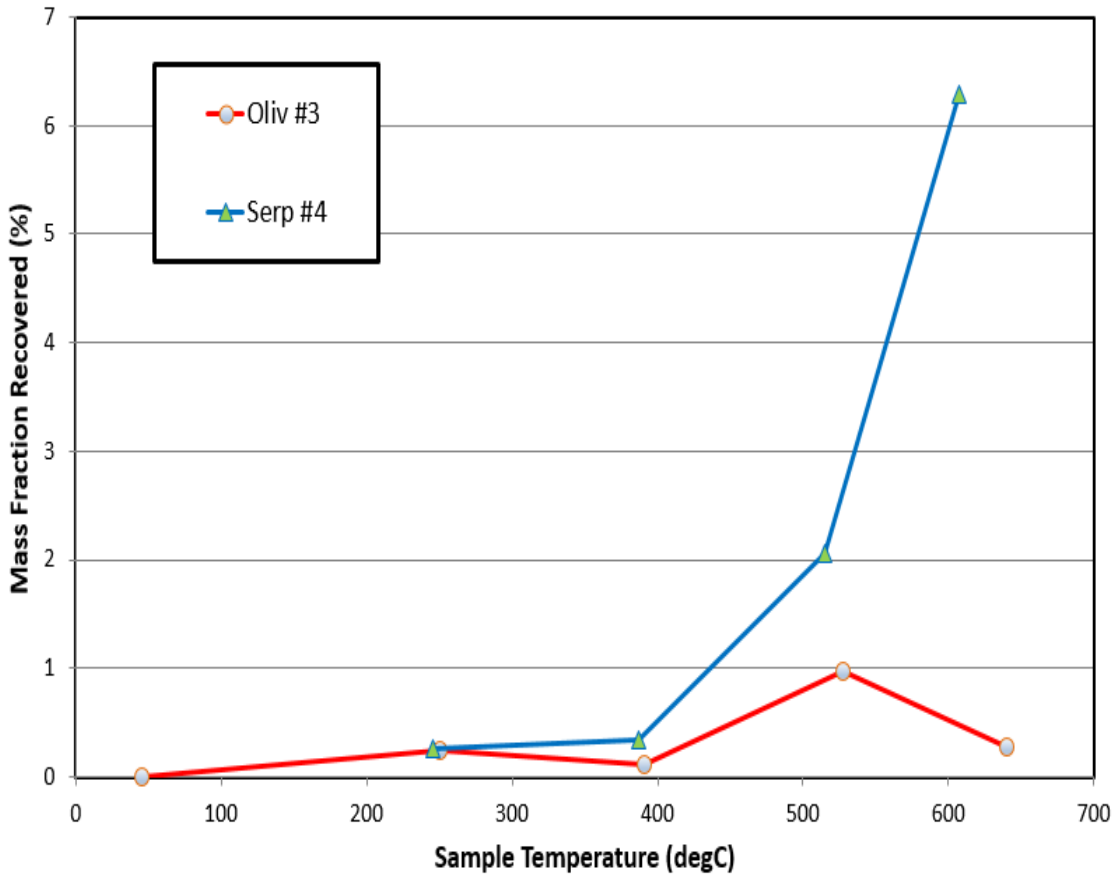

Figure 4.27. Mass Fraction of Volatiles Recovered as a Function of Temperature.

Note that serp #4 was run minus the initial step of cryo-trapping during pump-down, hence no result is reported for that stage. However, the relatively high value of cold trap efficiency (Table 4.1) calculated for this test show that very little gas is produced at this stage unlike what was characteristic for the Orgueil CLASS simulants, this assertion is supported by TGA results from heating serpentine which show negligible mass loss at the lowest temperatures (see Figure 3.17) There was a spike in gas production from 400^0C, and an even steeper spike at the final temperature as water was produced from hydroxyl groups present in serpentine (lizardite). Dlugogorski and Balucan (2014) noted that

prograde treatment of serpentine minerals below 800^0C forms forsterite in a reaction of the form;

$$2Mg_3Si_2O_5(OH)_{4(s)} \xrightarrow{< 800\ ^0C} 3Mg_2SiO_{4(s)} + SiO_2 + 4H_2O_{(g)}$$

Much less gas was collected from the olivine sample with the most significant release occurring during the 550^0C plateau, the temperature range over which production occurs suggests that gas was produced from what was likely hydroxyl-bearing impurities contained in this natural material as a result of terrestrial weathering. X-ray diffraction (XRD) results (see Figure 3.14) confirmed one such impurity to be lizardite which produces water following the reaction outlined above. Icy material captured on the cold trap during these experiments was typically clear white, odorless and mostly survived under ambient conditions as liquid water.

Table 4.1 shows that that the cold trap was efficient at retrieving released products collecting 94-100% of all gas that was produced from the olivine and serpentine test runs. This high efficiencies point at the dominant release of trappable gases over un-trappable varieties. 79% of the total available resource in the serpentine sample was extracted by vacuum pyrolysis while 100% of this amount was recovered by the cryo-trapping mechanism. The fact that resource extraction percentage calculated for olivine exceeds 100% is indicative of some of the problems with using TGA derived mass loss information to estimate the total gas content of a heterogeneous material. The 20-40 mg sample specimen used in thermogravimetry (TGA) must be completely representative of the larger body of material and if not, will produce misleading results. In this case, the sample used for TGA was very likely not representative of the larger body of material used in the

vacuum-pyrolysis experiment, one possibility is that it may have contained a smaller proportion of hydroxyl-bearing impurities and thus provided what appears to be a conservative estimate of the amount of gas producible.

4.3.2. **Orgueil Simulant.** The nature of temperature rise and gas release in granular Orgueil simulant samples broadly followed the pattern observed during tests on granular single-mineral samples. However, consolidated forms of the simulant displayed improved thermal conductivity that allowed for a significantly faster rate of sample temperature rise which in turn led to faster rates of volatile mass release.

This is highlighted by pressure curves that quickly reach a peak and then soon afterward decompose to former levels over the course of a temperature plateau. For the consolidated form, the heating style was much closer to isothermal than prograde as sample temperature reached a plateau maximum relatively quickly. Accordingly, the consolidated samples spent more than 90% of the time in a plateau step at a temperature close to its maximum.

Figure 4.28 shows the mass fraction of ice collected at the end of each temperature plateau and during the pre-test pump-down for all granular Orgueil simulant samples. 1.5-2.7 wt. % was recovered at the initial stage when the sample was held under non-heated vacuum and allowed to outgas at ambient temperatures that averaged 45^0C. This amount contained a significant, un-estimated proportion that was emplaced in the material from atmospheric contamination and was therefore loosely held. Hydrous sulphates such as epsomite which made up 6 wt. % of the simulant could also release some of its indigenous water under these conditions.

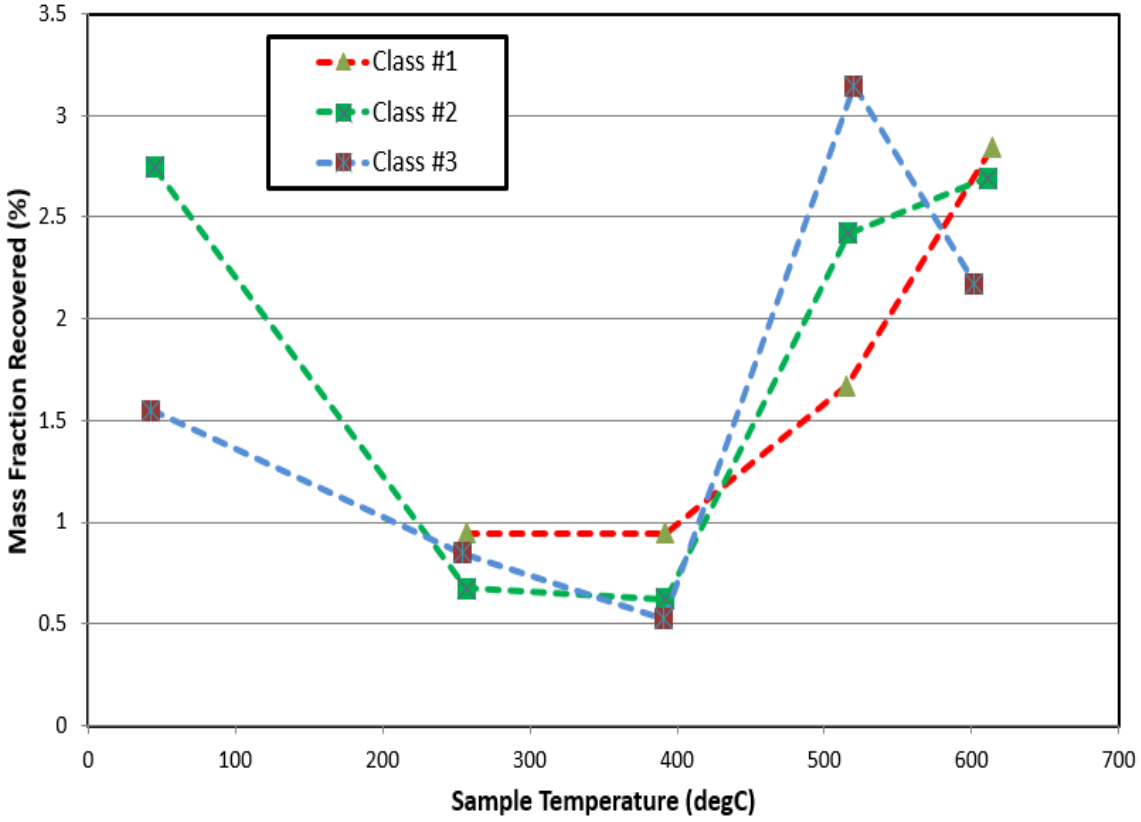

Figure 4.28. Mass Fraction of Volatiles Recovered as a Function of Temperature.

The first two active heating steps are the least productive in terms of volatile mass recovered. Gas release spikes at temperatures above 400^0C as water is produced from the Mg-serpentine phase. Going by the composition of the simulant and its pattern of gas release, it can be inferred that water production from this mineral phase was the largest single mineral contributor to volatile release.

Figure 4.29 shows the mass fraction of ice collected at various points during the experiments on the consolidated Orgueil simulant. The relatively high yield (3-5 wt. %) at the initial pump-down stage is reflective of the additional water that was used in the manufacture of this sample type. Clearly, some of this loosely held moisture remained

within the simulant even after it was dried. The mass fraction of volatiles recovered spiked above 400^0C which was indicative of mass release from the Mg-serpentine mineral phase.

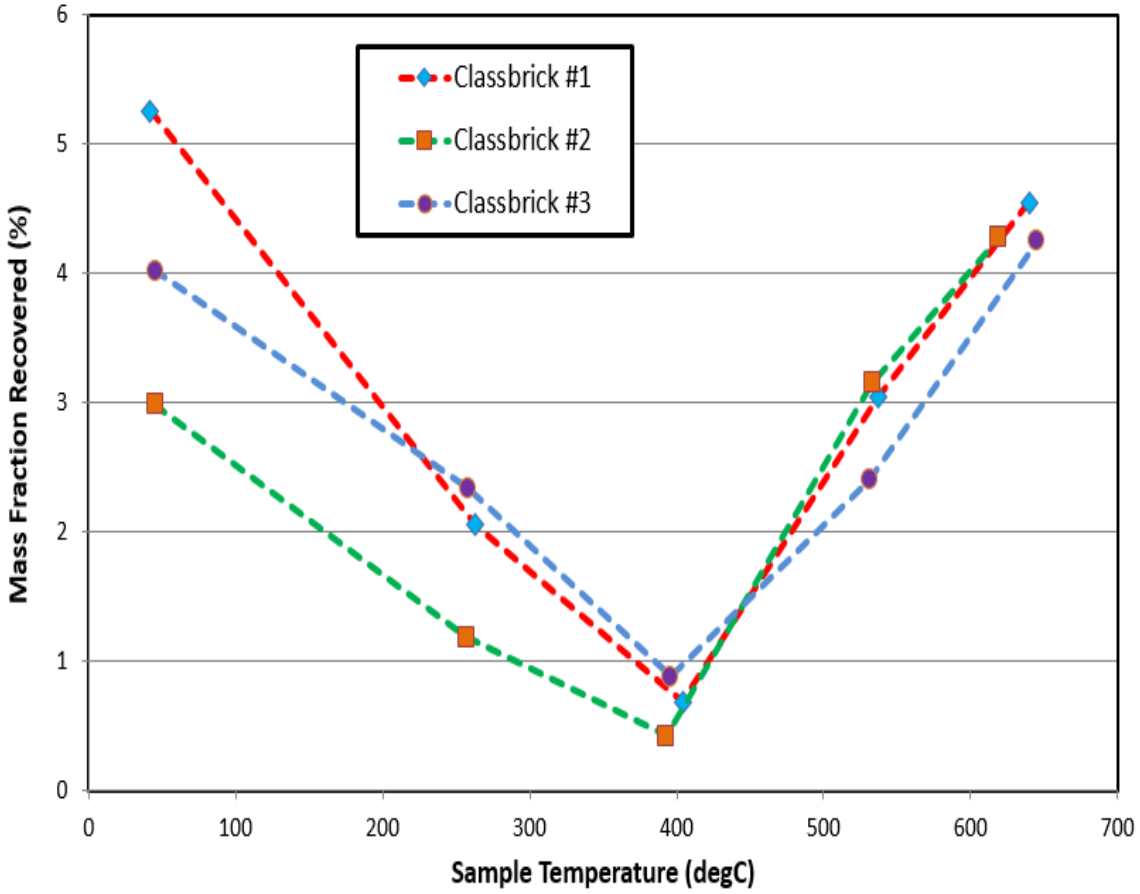

Figure 4.29. Mass Fraction of Volatiles Recovered as a Function of Temperature.

Besides pronounced differences in the amount of loosely held gaseous compounds available to be extracted at low temperatures, the granular and consolidated Orgueil simulant displayed broad similarities in the pattern of gas yield which was expected considering their similar mineral make-up. Generally, a greater fraction of volatile mass

was recovered and extracted from the consolidated form at each step of the heating experiment.

This may be due to the consolidated samples achieving higher temperatures, especially at the final two steps or it may alternatively be an indication of the greater productivity of isothermal heating over prograde heating to a similar temperature. Dlugogorski and Balucan (2014) report that thermal events are typically observed at higher temperatures in prograde heating experiments, while these same events occur at much lower temperature in isothermal studies. However, to make this determination requires further investigations which were not conducted here.

A summary of results and calculated test parameters from tests on granular and consolidated Orgueil simulant samples is presented on Table 4.1. Cold trap efficiency calculations show that 80-94% of extracted gas species were recovered. CLASS #1 is anomalously low because there was no cryo-trapping during the initial pump-down period meaning that the 1.5-2.7 wt. % volatiles that may have been produced at this stage were lost through the vacuum pumps. An average of 51% of the available resource was extracted from the granular samples while this number averages 70% for consolidated forms. This means that none of these samples were heated to total decomposition and a significant amount of producible material remained after heating was concluded. Estimated recovery ranged from 34-43% for the granular form and from 52-67% for consolidated forms. Recall that measures of resource extraction (%) and recovery (%) are based on thermogravimetric derived estimates, of the volatile content of the various sample types.

Generally, calculated cold trap efficiencies show that the LN_2-powered recovery mechanism was better at retrieving gases released from single-mineral Mg-serpentine

(lizardite). One reason for this is the relationship between the freezing point of a gas compound and the ability of a cold trap operating at a certain temperature to retrieve it. Table 4.2 shows the freezing points of produced species. The cold trap can only retrieve those whose freezing points lie above its operating temperature meaning compounds such as carbon monoxide (CO) that freeze below the operating temperature cannot be trapped. Water vapor which freezes at 0^0C and is efficiently retrieved was the main product from single mineral serpentine (lizardite) in contrast to the Orgueil simulant which produced 'un-trappable' CO, and less efficiently recovered methane and ethane. Other factors that influence cold trap efficiency included its relative frontal surface area and the molecular weight of the targeted gas compound.

Table 4.2. Freezing Points of Relevant Gas Compounds.

Gas compound	Freezing Point (^{0}C)
Sulphur (S/S_2)	115.2
Water Vapor (H_20)	0
Carbon dioxide (CO_2)	-78.5
Methane (CH_4)	-182
Ethane (C_2H_6)	-182.8
Carbon monoxide (CO)	-205
Nitrogen (N_2)	-210
Hydrogen (H_2)	-259.2

4.3.3. Estimates on the Nature and Amount of Gaseous Products. Due to the manner in which the vacuum-pyrolysis system was set up, the mass spectrometer operated in parallel with the cold trap. Figure 4.30 shows the relative proportion of atmosphere occupied by molecules of various gas species during a typical Orgueil granular simulant experiment (atmosphere composition history charts for other samples are presented in the Appendix). It gives mole percent/mole fraction which is the fraction of moles of a particular gas component in the mixture of gases that constitute the chamber atmosphere. In effect this result provides a ratio of gases present within the residual environment over the course of an experiment. It computes mole fraction by taking into account the total pressure in the mass spectrometer and the partial pressure of each selected gas component. Partial pressure is measured in the mass spectrometer by converting ion current to pressure using mass-dependent sensitivity factors while total pressure here refers to the internal pressure in the mass spectrometer (which is different from chamber total pressure measured by the external pressure gauges).

$$\text{Mole Fraction} = \frac{\text{Partial Pressure}}{\text{Total Pressure}}$$

It should be noted that this result does not provide an accurate estimate of the ratio of the different gas compounds produced from a sample but is rather a result biased in favor of gas species that are either un-trappable or trapped at very low efficiencies by the cold trap. Gas compounds which are efficiently frozen out of the atmosphere (H_2O, CO_2, and S_2) are not correctly represented in their appropriate proportions because such material is quickly immobilized on the surface of the trap as soon as they emerge from the sample body and therefore leave the residual environment.

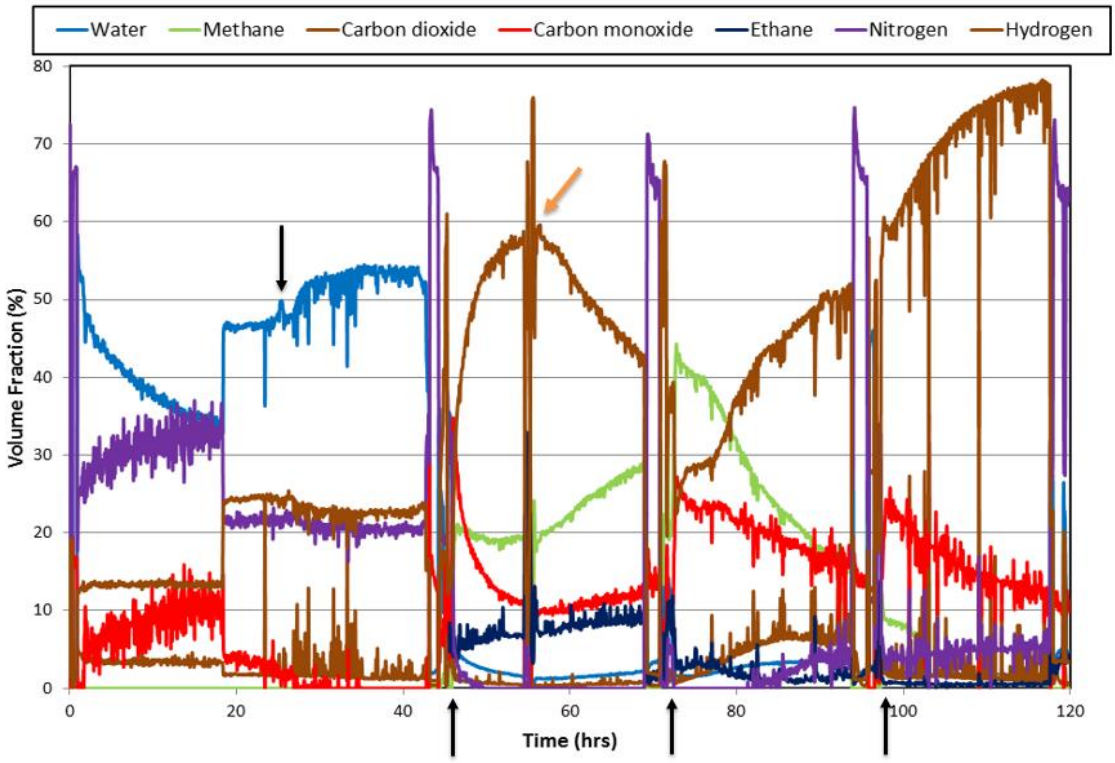

Figure 4.30. Showing the Relative Proportion of Gases Present in the Residual Environment During CLASS #2. (Black Arrows Indicate Start of Heat Ramp).

At various points over the course of CLASS #3 represented on the chart above, H_2, H_2O, CH_4, CO, and C_2H_6 constituted the major gas species present in the test environment. Methane as shown in Table 4.2 has a freezing point that is 14^0C above the estimated operating temperature of the cold trap (-196^0C), its close proximity to this threshold means that it is a specie likely to be captured at low efficiency. It is also important to note that temperature is not measured directly from the surface of the cold trap and therefore the surface could be at a temperature higher than liquid nitrogen temperature. Hydrogen evolved from metal surfaces within the chamber at a pace that quickened with increasing temperature. It freezes below liquid nitrogen temperature, therefore it could not be retrieved by the trap. CO is also not captured for this reason. The growth of the hydrogen component became prominent at temperatures of 400^0C and above for the Orgueil

simulant, leading to the thought that its presence might also be a marker for the start of the Mg-serpentine de-hydroxylation reaction. A number of mechanisms for this chemical reaction have been suggested (summarized in Dlugogorski and Balucan, 2014) whereby H^+ ions from less-tightly bonded hydroxyls in the serpentine mineral structure migrate to favorable reaction points during heating and combine with less well bonded hydroxyls to form a water molecule. Some fraction of the H^+ ions could conceivably combine to form H_2 as an intermediate or by-product. This process likely contributed to the high hydrogen component evident during the highest temperature plateaus. Nitrogen and hydrogen are also commonly part of the background atmosphere in vacuum systems at low pressure. Species not recoverable by the cold trap were removed at a steady rate by the 'throttled' turbo pump. Figure 4.31 shows the typical atmosphere during a consolidated simulant test.

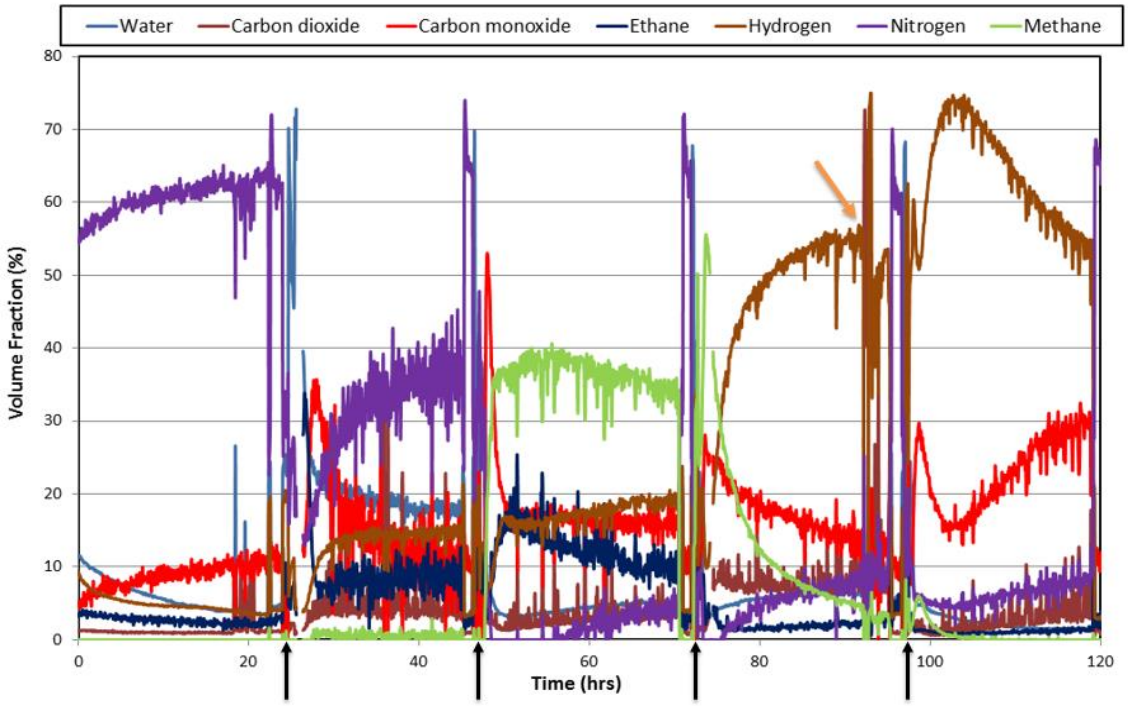

Figure 4.31. Showing the Relative Proportion of Gases Present in the Residual Environment During CLASSbrick #3. (Black Arrows Indicate Start of Heat Ramp).

Volatile-bearing phases in the Orgueil simulant are Mg-serpentine, epsomite, vermiculite, pyrite, smectite and sub-bituminous coal. Column 7 on Table 4.3 shows the estimated yield from each of these phases, calculated as:

Yield = Mass fraction of mineral in simulant × yield of gas from the given mineral

This gives an indication of the importance of a gas release from a given mineral in the Orgueil simulant. Results indicate that Mg-serpentine will be the most important mineral in terms of volatile production if the Orgueil simulant is heated to total decomposition producing about 38% of all final volatile products. Epsomite and sub-bituminous coal follow with 22% and 17% respectively. Consider column 8 which shows the potential yield of gas in terms of actual mass (grams) from each mineral component in a theoretical 400 gram Orgueil simulant sample. This is calculated by multiplying the yield fraction by the total mass of the sample (400g). This analysis suggests that at least 68 wt.% of all final products will be H_2O which is very likely an underestimation as this calculation only considers products from Mg-serpentine, vermiculite, epsomite and smectite to be water. However, in reality, some water will also be produced from the decomposition of sub-bituminous coal (not considered in this analysis as water producing due to a lack of knowledge by this author of the mass ratios between eventual products) and from the removal of atmospherically adsorbed, loosely held moisture which has been shown to be particularly important when considering thermal release events from this simulant. According to Hu G et al. (2006), gaseous sulphur in the form of allo-trophic species, S_n (n varies from 1-8) is produced from the thermal decomposition of pyrite with S_2 being the most dominant for decomposition at temperatures below 800K (527^0C).

Going by this theoretical analysis, a 400g sample will lose 61.6g (15.4%) of its initial mass as gas when decomposed, this assumes the absence of any secondary reactions. Recall that the amount of gas in granular and consolidated Orgueil simulant samples was experimentally estimated by thermogravimetric analysis to be 19.41% and 23.53% respectively meaning that this estimate is off by a factor of 0.26.

Mass fraction of gas release per source mineral values were obtained from thermogravimetric analysis results from experiments conducted by Montavani et al. (2016) on individual component mineral phases contained in the Orgueil simulant. Mass fraction of source mineral in Orgueil simulants values were obtained from Britt and Covey (2016) on the mineralogical make-up of the Orgueil simulant.

Table 4.3. Estimated Yield from Volatile-Bearing Phases in the Orgueil Simulant.

Volatile Source Mineral	Mass Fraction of Source Mineral in Orgueil Simulant	Chemical Reaction	Temperature Range (^{0}C)	Released Gas	Mass Fraction of Gas Release per Source Material	Yield from Orgueil Simulant	Theoretical Yield from 400 g Orgueil simulant (g)
Mg-serpentine	0.48	Dehydroxylation	550-700	H_2O	0.12	0.06	24
Vermiculite	0.09	Dehydration/dehydroxylation	65-150, 450-850	H_20	0.09	0.008	3.2
Pyrite	0.065	Desulphurization	250-740	S_n/S_2	0.35	0.023	9.2
Epsomite	0.06	Dehydration	25-275	H_20	0.56	0.034	13.6
Smectite	0.05	Dehydration/dehydroxylation	65-150, 650-750	H_2O	0.06	0.003	1.2
Sub-bituminous coal	0.05	Dehydration/dehydroxylation/decarbonation/desulphurization	300-800	H_2O, CO_2, CO, S_n	0.52	0.026	10.4

Figure 4.32 presents a chart that shows the mass fraction given in percent of recovered icy material that sublimated into the atmosphere under ambient conditions. This measure provides a rough estimate of the nature of the recovered icy material as among the gas compounds produced and recovered on the cold trap, only H_2O and S_2 are expected to survive the transition from ice to liquid. This result suggests that larger proportions of non-H_2O and S_2 material are captured during the 400 ^{0}C and 550 ^{0}C plateaus (during tests on the Orgueil simulant) which correspond to the 3rd and 4th temperature steps as presented on the chart below. Serp #4 is represented by the blue bars. As expected, very little non-water volatiles were produced from this sample and therefore most of the icy material collected from this sample survived the transition from solid to a liquid under ambient conditions.

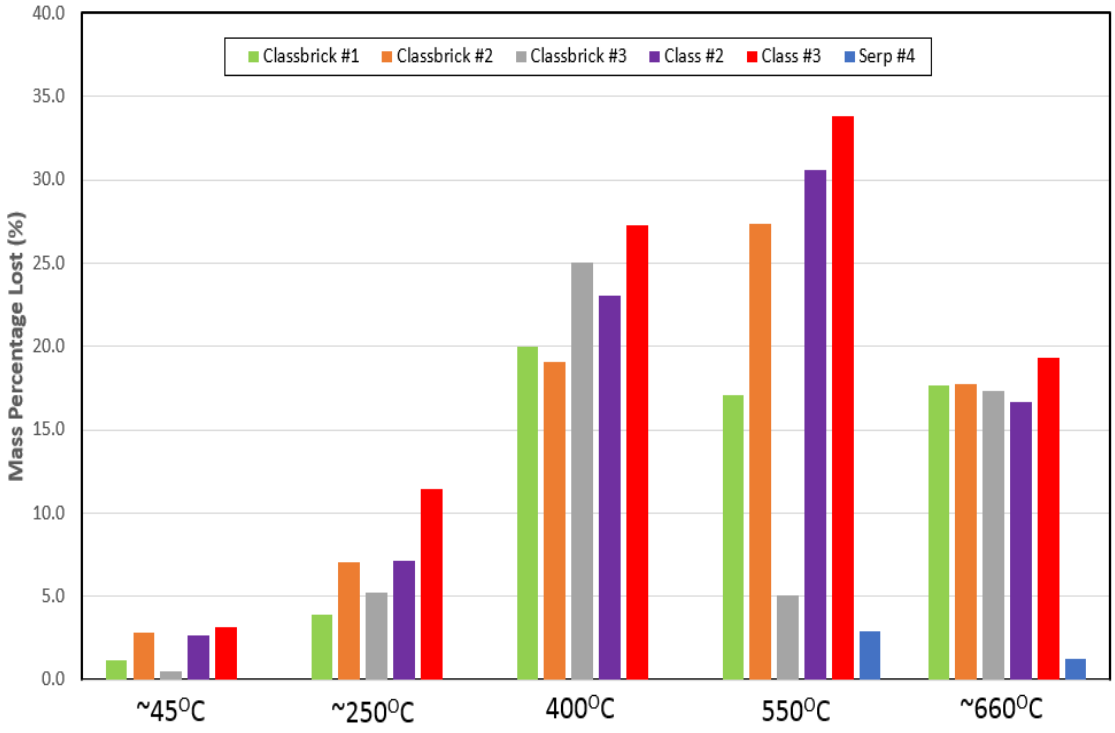

Figure 4.32. Mass Percent of Recovered Ice Sublimated at Ambient Conditions. For the Different Tests.

The images in Figure 4.33 show the nature of the liquid after its transition from the solid icy state. The yellowish-metallic color is an indication of the presence of sulphur compounds in (a). The material also had a ‘rotten egg’ smell that might be indicative of the presence of sulphide species.

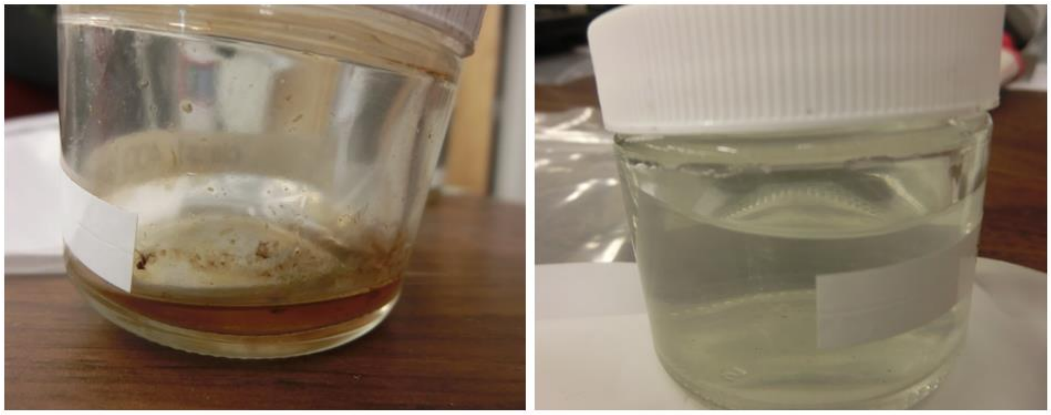

Figure 4.33. Typical Liquid Melt. (Left: From an orgueil simulant sample, right: From serpentine.

5. CONCLUSIONS

This thesis details experiments conducted to investigate the extraction and recovery of volatile resources such as H_2O, CO_2, S_2 and CH_4 from bulk simulants acting as analogs for carbonaceous solar system bodies. Gas release was determined by derived pressure-time curves and a liquid-nitrogen cooled trap acted to recover evolved gas by freezing

Some conclusions which may be drawn from this exercise include:

1. Vacuum pyrolysis is an effective driver of volatile release from bulk hydrated materials tested.
2. Material properties such as porosity and bulk density significantly affect thermal conductivity in vacuum pyrolysis of bulk bodies, this in turn affects heat transfer and consequently the kinetics of thermal decomposition.
3. Liquid nitrogen-cooled cold-trapping effectively captures the target volatiles as they are released from the ore minerals by heating.

5.1. FUTURE WORK

The composition of the dominant components of the melt-liquid derived from the icy material recovered during tests will be investigated. Of particular interest is the presence or absence of electrode poisons, potentially harmful if such liquid were to be subjected to electrochemistry to process it into more useful forms.

Physical strength tests on heated and non-heated samples of the simulant material will also be carried out to investigate changes caused by heating and gas escape.

Work is currently underway to calculate a mass release rate with time of the various gas compounds produced during these experiments using the total pressure curve and the

mass spectrometer partial pressure readings. Concurrently, a one-dimensional finite difference model of the experiment is being built to compare to the experimental results.

5.2. RECOMMENDATIONS

Detailed investigations need to be conducted that provide accurate and precise information on asteroid mineralogy and physical properties that goes beyond an inferred mineralogy for a few millimeters of surface material or a reliance on meteoritic material. Information on the spatial variation in asteroid composition, especially at depth would be particularly useful in calculating parameters such as potential reserves. More investigations need to be conducted to better understand the following observations:

1. Volatiles recoveries seem affected by the spatial variability, as well as the average values, of material composition and texture.
2. For this process, the composition of the original material being heated in terms of its mineralogy seemed to be the single most important factor controlling the nature of products derived more than any secondary reactions in the gas phase.

The ongoing sample return missions (OSIRIS-REX and Hayabusa-2) to carbonaceous bodies, if successful will provide unprecedented ground truth on the composition of this class of material and allow for an assessment of the viability and accuracy of the use of meteoritic studies and remote sensing methods to discern mineralogical composition of volatile-bearing solar system bodies.

APPENDIX

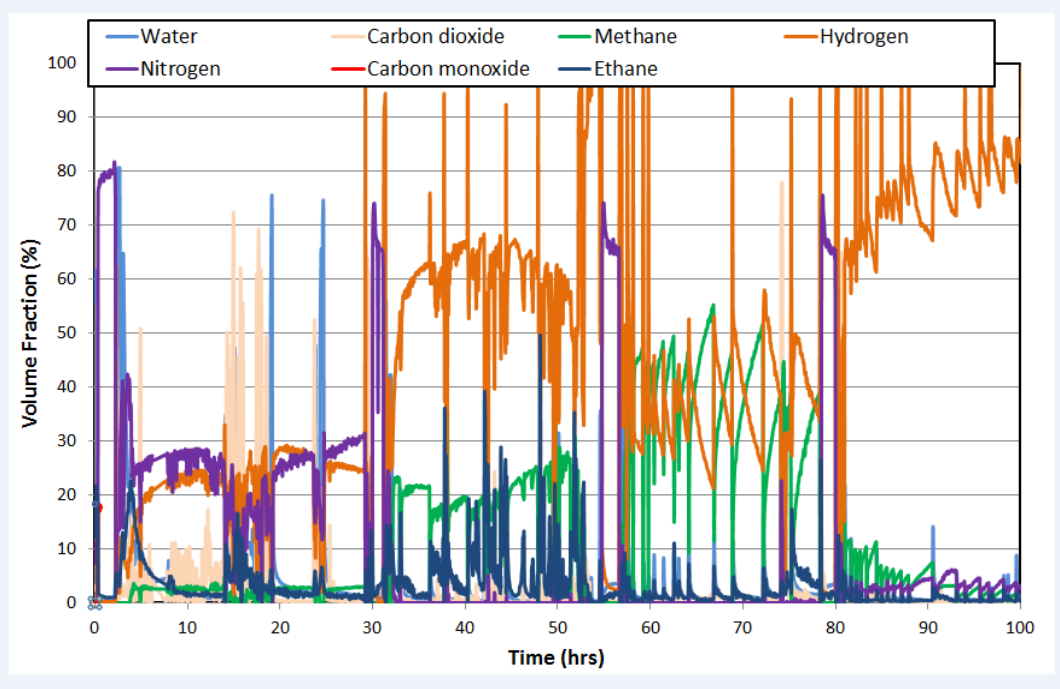

Gases present in the Residual Environment during CLASS #1

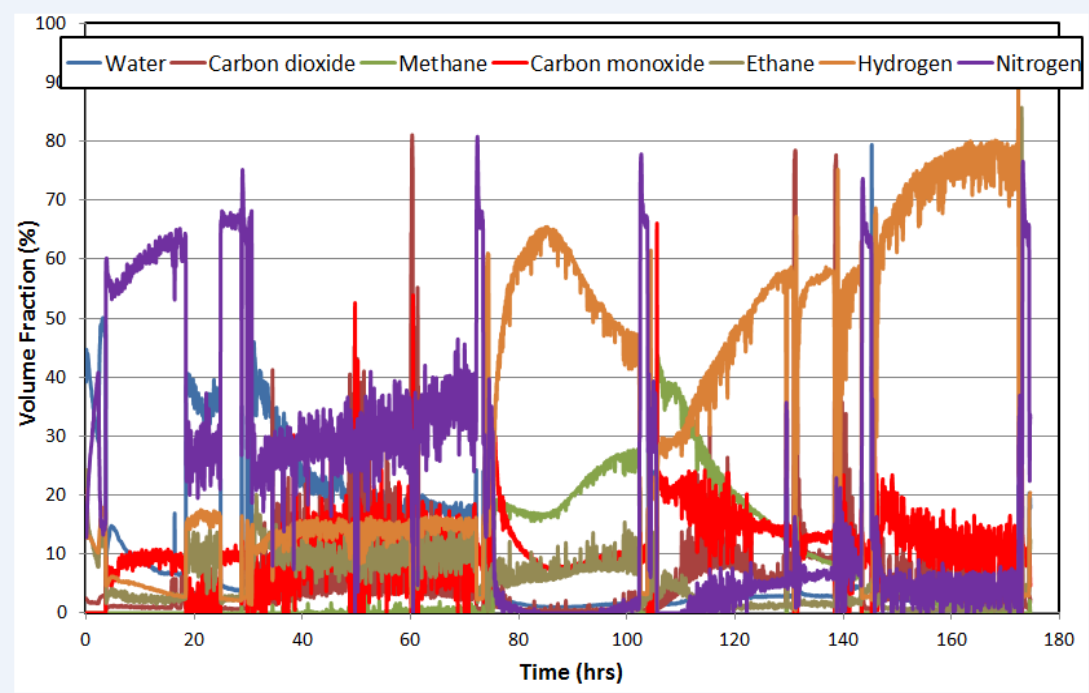

Gases Present in the Residual Environment during CLASS #3

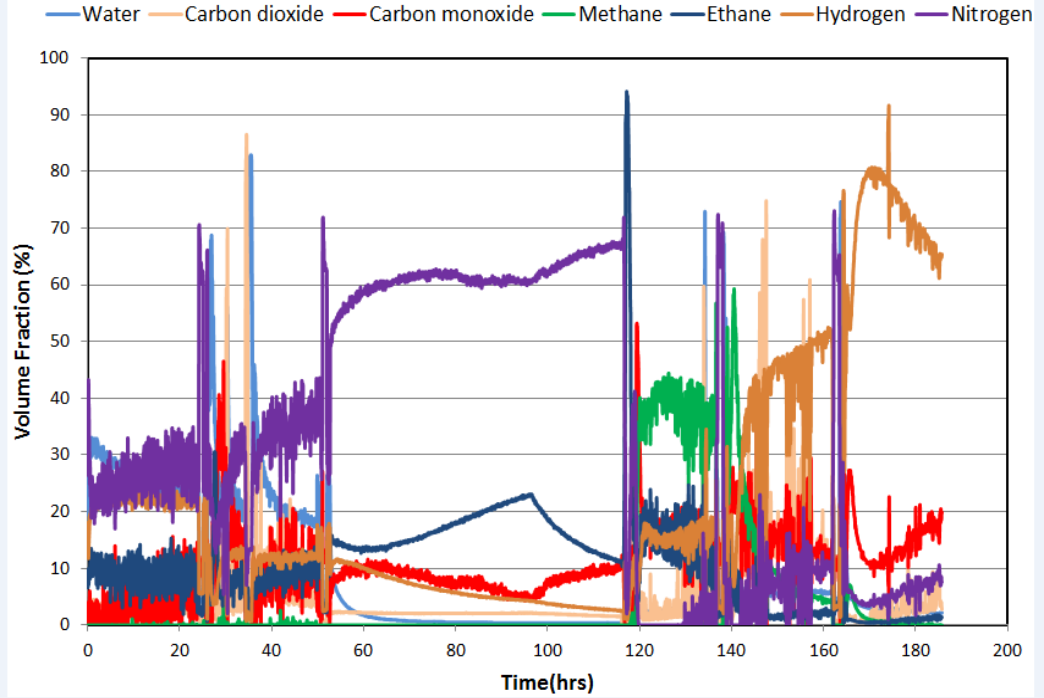

Gases Present in the Residual Environment during CLASSbrick #2

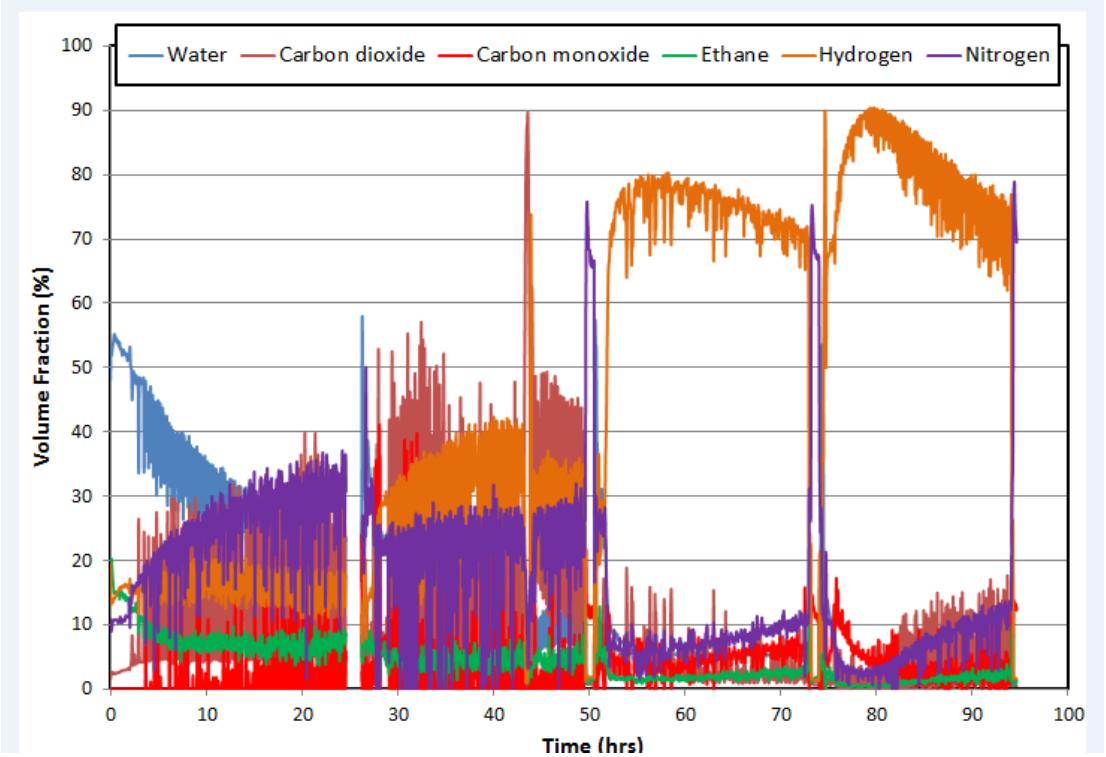

Gases present in the Residual Environment during Oliv #3

BIBLIOGRAPHY

Abe, M., et al. "Near-infrared spectral results of asteroid Itokawa from the Hayabusa spacecraft." Science 312.5778 (2006): 1334-1338.

Akai, Junji. "TTT diagram of serpentine and saponite, and estimation of metamorphic heating degree of Antarctic carbonaceous chondrites." Antarctic Meteorite Research 5 (1992): 120.

Asphaug, E., et al. "Brazil nuts on Eros: size-sorting of asteroid regolith." (2001).

Baer, James, Steven R. Chesley, and Robert D. Matson. "Astrometric masses of 26 asteroids and observations on asteroid porosity." The Astronomical Journal 141.5 (2011): 143.

Balucan, Reydick D., Bogdan Z. Dlugogorski, Eric M. Kennedy, Irina V. Belova, and Graeme E. Murch, "Energy cost of heat activating serpentinites for CO2 storage by mineralisation," International Journal of Greenhouse Gas Control, Vol 17, p 225-239. (2013).

Beck, P., et al. "Hydrous mineralogy of CM and CI chondrites from infrared spectroscopy and their relationship with low albedo asteroids." Geochimica et Cosmochimica Acta 74.16 (2010): 4881-4892.

Benner, Lance AM, et al. "Near-Earth Asteroid 2005 CR37: Radar images and photometry of a candidate contact binary." Icarus 182.2 (2006): 474-481.

Binzel, Richard P., et al. "MUSES-C target asteroid (25143) 1998 SF36: a reddened ordinary chondrite." Meteoritics & Planetary Science 36.8 (2001): 1167-1172.

Bland, Philip A., Gordon Cressey, and Olwyn N. Menzies. "Modal mineralogy of carbonaceous chondrites by X-ray diffraction and Mössbauer spectroscopy." Meteoritics & Planetary Science 39.1 (2004): 3-16.

Boström, Kurt, and Kurt Fredriksson. "Surface conditions of the Orgueil meteorite parent body as indicated by mineral associations." Surface conditions of the Orgueil meteorite parent body as indicated by mineral associations, by Boström, Kurt; Fredriksson, Kurt. Washington, Smithsonian Institution, (1966).

Brearley, Adrian J., and Rhian H. Jones. "Chondritic meteorites." Reviews in Mineralogy and Geochemistry 36.1 (1998): 3-1.

Zussman, J., G. W. Brindley, and J. J. Comer. "Electron diffraction studies of serpentine minerals." American Mineralogist 42.3-4 (1957): 133-153.

Brindley, G. W., and Ryozo Hayami. "Mechanism of formation of forsterite and enstatite from serpentine." (1965).

Britt, D. T., and GJ Consolmagno SJ. "Modeling the structure of high porosity asteroids." Icarus 152.1 (2001): 134-139.

Brozović, Marina, et al. "Radar and optical observations and physical modeling of triple near-Earth Asteroid (136617) 1994 CC." Icarus 216.1 (2011): 241-256.

Bullock, E. S., et al. "Mineralogy and texture of Fe-Ni sulfides in CI1 chondrites: Clues to the extent of aqueous alteration on the CI1 parent body." Geochimica et Cosmochimica Acta 69.10 (2005): 2687-2700.

Burbine, Thomas H., et al. "Meteoritic parent bodies: Their number and identification." Asteroids III 653 (2002).

Burgess, R., I. P. Wright, and C. T. Pillinger. "Determination of sulphur-bearing components in C1 and C2 carbonaceous chondrites by stepped combustion." Meteoritics 26.1 (1991): 55-64.

Bus, Schelte J., and Richard P. Binzel. "Phase II of the small main-belt asteroid spectroscopic survey: The observations." Icarus 158.1 (2002): 106-145.

Busch, Michael W., et al. "Radar observations and the shape of near-Earth Asteroid 2008 EV5." Icarus 212.2 (2011): 649-660.

Campins, Humberto, et al. "Water ice and organics on the surface of the asteroid 24 Themis." Nature 464.7293 (2010): 1320-1321.

Chabot, N., Abell, P., Britt, D., Dankanich, J., Emery, J., Rivkin, A., and Sheeres, D.“Report of the Small Bodies Assessment Group Asteroid Redirect Mission SpecialactionTeamLunarandPlanetaryInstitute/SBAGwebsitehttp://www.lpi.usra. edu/sbag/documents/SBAG _ARM_SAT_07_30_14.pdf (7/30/14) (2014).

Chapman, Clark R. "Cratering on asteroids from Galileo and NEAR Shoemaker." Asteroids III (2002): 315-329.

Chesley, Steven R., et al. "Orbit and bulk density of the OSIRIS-REx target Asteroid (101955) Bennu." Icarus 235 (2014): 5-22.

Clark, Beth Ellen, et al. "Asteroid space weathering and regolith evolution." Asteroids III 585 (2002).

Clayton, Robert N., and Toshiko K. Mayeda. "Oxygen isotope studies of carbonaceous chondrites." Geochimica et Cosmochimica Acta 63.13 (1999): 2089-2104.

Cordell, Bruce, and Otto Steinbronn. "An analysis of possible advanced space strategies featuring the role of space resource utilization." Acta Astronautica 26.1 (1992): 19-27.

Cole, D.M., and Cox, D. W., Islands in Space, The Challenge of the Planetoids, Chilton books, Philadelphia, Pa., 1964.

Consolmagno, G. J., D. T. Britt, and R. J. Macke. "The significance of meteorite density and porosity." Chemie der Erde-Geochemistry 68.1 (2008): 1-29.

Cole, D.M., and Cox, D. W., Islands in Space, The Challenge of the Planetoids, Chilton books, Philadelphia, Pa., 1964.

Court, Richard W., and Mark A. Sephton. "Meteorite ablation products and their contribution to the atmospheres of terrestrial planets: An experimental study using Court, Richard W., and Mark A. Sephton. "The contribution of sulphur dioxide from ablating micrometeorites to the atmospheres of Earth and Mars." Geochimica et Cosmochimica Acta 75.7 (2011): 1704-1717.pyrolysis-FTIR." Geochimica et Cosmochimica Acta 73.11 (2009): 3512-3521.

Court, Richard W., and Mark A. Sephton. "New estimates of the production of volatile gases from ablating carbonaceous micrometeoroids at Earth and Mars during an E-belt-type Late Heavy Bombardment." Geochimica et Cosmochimica Acta 145 (2014): 175-205.

Cutler, Andrew H., and Man L. Hughes. "Transportation economics of extraterrestrial resource utilization." Space Manufacturing 5 (1985): 233-244.

Demura, Hirohide, et al. "Pole and global shape of 25143 Itokawa." Science 312.5778 (2006): 1347-1349.

Dlugogorski, Bogdan Z., and Reydick D. Balucan. "Dehydroxylation of serpentine minerals: Implications for mineral carbonation." Renewable and Sustainable Energy Reviews 31 (2014): 353-367.

Elvis, Martin, et al. "Ultra-low delta-v objects and the human exploration of asteroids." Planetary and Space Science 59.13 (2011): 1408-1412.

Endre, Magnus, and Adolf Bischoff. "Carbonates in CI chondrites: Clues to parent body evolution." Geochimica et cosmochimica acta 60.3 (1996): 489-507.

Faust, George Tobias, and Joseph John Fahey. The serpentine-group minerals. No. 384-A. US Govt. Print. Off.,, 1962.

Fujiwara, Akira, et al. "The rubble-pile asteroid Itokawa as observed by Hayabusa." Science 312.5778 (2006): 1330-1334.

Fredriksson, Kurt, and John F. Kerridge. "Carbonates and sulfates in CI chondrites: Formation by aqueous activity on the parent body." Meteoritics & Planetary Science 23.1 (1988): 35-44.

Gaffey, Michael J., et al. "Mineralogical variations within the S-type asteroid class." Icarus 106.2 (1993): 573-602.

George Faust and Joseph Fahey “The Serpentine group minerals”, Geological Survey Professional Paper 384-A, United States Government Printing Office (1962), Washington.

Gertsch, R.E., Barnes, R., Cutler, A. H., and Gaffey, M,. Space Resources. In Proc. Of the Fourth Annual L5 Space Development conference, ed. F. Hecker, AAS 85-746 to 85-749 (San Diego:Univelt), pp.63-90. (1985).

Gertsch, Richard E. "Asteroid mining." (1992).

Gertsch, Richard, John L. Remo, and Leslie Sour Gertsch. "Near-Earth Resources." Annals of the New York Academy of Sciences 822.1 (1997): 468-510.

Gertsch, L. S., and R. E. Gertsch. "Mine planning for asteroid orebodies." Space Resources Roundtable II. (2000).

Gradie, Jonathan C., Clark R. Chapman, and Edward F. Tedesco. "Distribution of taxonomic classes and the compositional structure of the asteroid belt." Asteroids II. (1989).

Gibson Jr, E. K., and F. F. Andrawes. "Nature of the gases released from lunar rocks and soils upon crushing." Lunar and Planetary Science Conference Proceedings. Vol. 9. (1978).

Greshake, Ansgar, et al. "Heating experiments simulating atmospheric entry heating of micrometeorites: Clues to their parent body sources." Meteoritics & Planetary Science 33.2 (1998): 267-290.

Gao, Xia, and Mark H. Thiemens. "Isotopic composition and concentration of sulfur in carbonaceous chondrites." Geochimica et Cosmochimica Acta 57.13 (1993): 3159-3169.

Gounelle, Matthieu, and Michael E. Zolensky. "A terrestrial origin for sulfate veins in CI1 chondrites." Meteoritics & Planetary Science 36.10 (2001): 1321-1329.

Herrick, Samuel. "Exploration and 1994 exploitation of Geographos." Asteroids (1979): 222-226.

Hiroi, Takahiro, et al. "Thermal metamorphism of the C, G, B, and F asteroids seen from the 0.7 μm, 3 μm, and UV absorption strengths in comparison with carbonaceous chondrites." Meteoritics & Planetary Science 31.3 (1996): 321-327.

Holsapple, Keith A. "Spin limits of Solar System bodies: From the small fast-rotators to 2003 EL61." Icarus 187.2 (2007): 500-509.

Howard, K. T., et al. "Modal mineralogy of CM2 chondrites by X-ray diffraction (PSD-XRD). Part 1: Total phyllosilicate abundance and the degree of aqueous alteration." Geochimica et Cosmochimica Acta 73.15 (2009): 4576-4589.

Howard, K. T., et al. "Modal mineralogy of CM chondrites by X-ray diffraction (PSD-XRD): Part 2. Degree, nature and settings of aqueous alteration." Geochimica et Cosmochimica Acta 75.10 (2011): 2735-2751.

Hsieh, Henry H., and David Jewitt. "A population of comets in the main asteroid belt." Science 312.5773 (2006): 561-563.

Hu G et al. Decomposition and oxidation of pyrite. Prog Energy Combust Sci (2006);32(3):295–314.

Jewitt, David, Jing Li, and Jessica Agarwal. "The dust tail of asteroid (3200) Phaethon." The Astrophysical Journal Letters 771.2 (2013): L36.

Johnson, Richard D., and Charles Holbrow. "Space Settlements." A Design Study. NASA, Washington, SP-413 (1977).

Johnson, Craig A., and Martin Prinz. "Carbonate compositions in CM and CI chondrites and implications for aqueous alteration." Geochimica et Cosmochimica Acta 57.12 (1993): 2843-2852.

Kuck, D.L (1979), Near-Earth Extraterrestrial Resources, in Space Manufacturing 3, Proceedings of the 4th Princeton/AIAA Conference, May 14-17, (1979).

Lewis, John S. "The temperature gradient in the solar nebula." Science 186.4162 (1974): 440-443.

Lewis, John S. Space Resources. John Wiley & Sons, Inc., (1987).

Lewis, John S. "Mining the sky: untold riches from the asteroids, comets, and planets." Reading, Mass.: Addison-Wesley Pub. Co., c1996. 1 (1996).

Lebofsky, Larry A., et al. "The nature of low-albedo asteroids from 3-μm multi-color photometry." Icarus 83.1 (1990): 16-26.

Licandro, Javier, et al. "The nature of comet-asteroid transition object (3200) Phaethon." Astronomy & Astrophysics 461.2 (2007): 751-757.

Licandro, J., et al. "(65) Cybele: detection of small silicate grains, water-ice, and organics." Astronomy & Astrophysics 525 (2011): A34.

Li, Jianyang, Michael F. A'Hearn, and Lucy A. McFadden. "Photometric analysis of Eros from NEAR data." Icarus 172.2 (2004): 415-431.

Lowry, S. C., et al. "The internal structure of asteroid (25143) Itokawa as revealed by detection of YORP spin-up." Astronomy & Astrophysics 562 (2014): A48.

Lunine, Jonathan I. "Origin of water ice in the solar system." Meteorites and the early solar system II (2006): 309-319.

Mackenzie, K. J. D., and R. M. Berezowski. "Thermal and Mossbauer studies of iron-containing hydrous silicates. III. Cronstedtite." Thermochimica Acta 44.2 (1981): 171-187.

Magri, Christopher, et al. "Radar and photometric observations and shape modeling of contact binary near-Earth Asteroid (8567) 1996 HW1." Icarus 214.1 (2011): 210-227.

Mainzer, Amy, et al. "NEOWISE observations of near-Earth objects: Preliminary results." The Astrophysical Journal 743.2 (2011): 156.

Mantovani, James G., Laurent Sibille, Ivan I. Townsend, Jason M. Schuler, Armando Delgado, Kevin D. Grossman, Adam M. Swanger, Matthew W. Nugent, Daniel T. Britt, and S. Wiggins,. “Excavation and volatile analysis in icy asteroid simulant: Preliminary results,”presented to Space Resources Roundtable XVII / Planetary and Terrestrial Mining Sciences Symposium, held at Colorado School of Mines, Golden, Colorado, 7-9 June 2016 (2016).

McSween, Harry Y. "Are carbonaceous chondrites primitive or processed? A review." Reviews of Geophysics 17.5 (1979): 1059-1078.

Milliken, Ralph E., and Andrew S. Rivkin. "Brucite and carbonate assemblages from altered olivine-rich materials on Ceres." Nature Geoscience 2.4 (2009): 258-261.

Miyamoto, Hideaki, et al. "Regolith migration and sorting on asteroid Itokawa." Science 316.5827 (2007): 1011-1014.

Morrison, David, and John Niehoff. "Future exploration of the asteroids." Asteroids 1 (1979): 227-250.

Mommert, M., et al. "Constraining the physical properties of near-Earth object 2009 BD." The Astrophysical Journal 786.2 (2014): 148.

Mueller, Robert P., and Paul J. Van Susante. "A Review of Extra-Terrestrial Mining Robot Concepts." Earth and Space: Engineering, Science, Construction, and Operations in Challenging Environments. 2012. 295-314. (2012).

Nichols, Charles R. "Volatile products from carbonaceous asteroids." Resources of near-earth space (1993): 543-568.

Nolan, Michael C., et al. "Shape model and surface properties of the OSIRIS-REx target Asteroid (101955) Bennu from radar and light curve observations." Icarus 226.1 (2013): 629-640.

Nozaki, Wataru, Tomoki Nakamura, and Takaaki Noguchi. "Bulk mineralogical changes of hydrous micrometeorites during heating in the upper atmosphere at temperatures below 1000 C." Meteoritics & Planetary Science 41.7 (2006): 1095-1114.

Okada, Tatsuaki, et al. "X-ray fluorescence spectrometry of asteroid Itokawa by Hayabusa." Science 312.5778 (2006): 1338-1341.

O' Leary, Brian. "Mining the Apollo and Amor asteroids." Science 197.4301 (1977): 363-366.

Oleary, Brian, et al. "Retrieval of asteroidal materials." Space Resources and Space Settlements. (1979).

O'Neill, Gerard K. "The colonization of space." Physics Today 27.9 (1974): 32-40.

Opeil, C. P., G. J. Consolmagno, and D. T. Britt. "The thermal conductivity of meteorites: New measurements and analysis." Icarus 208.1 (2010): 449-454.

Ostro, Steven J., et al. "Radar imaging of binary near-Earth asteroid (66391) 1999 KW4." Science 314.5803 (2006): 1276-1280.

Paulik, J., Paulik, F., and Arnold, M., Dehydration of magnesium sulfate heptahydrate investigated by quasi isothermal-quasi isobaric TG,Therm. Acta 50, 105-110 (1981).

Pravec, Petr, and Alan W. Harris. "Fast and slow rotation of asteroids." Icarus 148.1 (2000): 12-20.

Rivkin, A. S., et al. "Hydrated minerals on asteroids: The astronomical record." Asteroids III 1 (2002): 235-253.

Rivkin, Andrew S., and Joshua P. Emery. "Detection of ice and organics on an asteroidal surface." Nature 464.7293 (2010): 1322-1323.

Rivkin, A., E. Howell, and J. Emery. "The LXD-mode main-belt/NEO observing program (LMNOP): results." Asteroids, Comets, Meteors 2014. (2014).

Rivkin, Andrew S., et al. "Astronomical Observations of Volatiles on Asteroids." Asteroids IV (2015): 65-87.

Robinson, M. S., et al. "The geology of 433 Eros." Meteoritics & Planetary Science 37.12 (2002): 1651-1684.

Ross, Shane D. "Near-earth asteroid mining." Space (2001).

Sánchez, Paul, and Daniel J. Scheeres. "The strength of regolith and rubble pile asteroids." Meteoritics & Planetary Science 49.5 (2014): 788-811.

Sanders, Gerald. "ISRU-An overview of NASA's current development activities and long-term goals." 38th Aerospace Sciences Meeting and Exhibit. (2000).

Sanders, Gerald B., et al. "Results from the NASA capability roadmap team for in-situ resource utilization (ISRU)." (2005).

Scheeres, D. J., and R. W. Gaskell. "Effect of density inhomogeneity on YORP: The case of Itokawa." Icarus 198.1 (2008): 125-129.

Scheeres, Daniel J., et al. "Scaling forces to asteroid surfaces: The role of cohesion." Icarus 210.2 (2010): 968-984.

Sercel, Joel, “Asteroid Privided In-situ Supplies (APIS)”, Personal Communication (2016).

Smykatz-Kloss, Werner. "Determination of impurities in minerals by means of standardized differential thermal analysis." Purity Determinations by Thermal Methods. ASTM International, (1984).

Sonter, Mark Joseph. "The technical and economic feasibility of mining the near-earth asteroids." Acta Astronautica 41.4-10 (1997): 637-647.

Takir, Driss, and Joshua P. Emery. "Outer main belt asteroids: Identification and distribution of four 3-μm spectral groups." Icarus 219.2 (2012): 641-654.

Takir, Driss, et al. "Nature and degree of aqueous alteration in CM and CI carbonaceous chondrites." Meteoritics & Planetary Science 48.9 (2013): 1618-1637.

Takir, Driss, Joshua P. Emery, and Harry Y. McSween. "Toward an understanding of phyllosilicate mineralogy in the outer main asteroid belt." Icarus 257 (2015): 185-193.

Tedesco, Edward F., and François-Xavier Desert. "The infrared space observatory deep asteroid search." The Astronomical Journal 123.4 (2002): 2070.

Tsiolkovsky, Konstantin Eduardovich. "Exploration of the universe with reaction machines." The Science Review 5 (1903).

Thomas, P. C., et al. "Shoemaker crater as the source of most ejecta blocks on the asteroid 433 Eros." Nature 413.6854 (2001): 394-396.

Thomas, Cristina A., and Richard P. Binzel. "Identifying meteorite source regions through near-Earth object spectroscopy." Icarus 205.2 (2010): 419-429.

Tholen, David J. "Asteroid taxonomic classifications." Asteroids II. (1989).

Tsuchiyama, Akira, et al. "Three-dimensional structure of Hayabusa samples: origin and evolution of Itokawa regolith." Science 333.6046 (2011): 1125-1128.

Urey, Harold Clayton. "The planets: their origin and development." (1952).

Veverka, J., et al. "NEAR9s Flyby of 253 Mathilde: Images of a C Asteroid." Science 278.5346 (1997): 2109-2114.

Veverka, Joseph, et al. "NEAR at Eros: Imaging and spectral results." Science 289.5487 (2000): 2088-2097.

Volquardsen, Eric L., Andrew S. Rivkin, and Schelte J. Bus. "Composition of hydrated near-Earth object (100085) 1992 UY4." Icarus 187.2 (2007): 464-468.

Whiteley, Robert J., David J. Tholen, and Carl W. Hergenrother. "Lightcurve analysis of four new monolithic fast-rotating asteroids." Icarus 157.1 (2002): 139-154.

Wyart, Matthieu, Sidney R. Nagel, and Thomas A. Witten. "Geometric origin of excess low-frequency vibrational modes in weakly connected amorphous solids." EPL (Europhysics Letters) 72.3 (2005): 486.

Yano, Hajime, et al. "Touchdown of the Hayabusa spacecraft at the Muses Sea on Itokawa." Science 312.5778 (2006): 1350-1353.

Zolensky, Michael, Ruth Barrett, and Lauren Browning. "Mineralogy and composition of matrix and chondrule rims in carbonaceous chondrites." Geochimica et Cosmochimica Acta 57.13 (1993): 3123-3148.

Zolensky, Michael E., et al. "CM chondrites exhibit the complete petrologic range from type 2 to 1." Geochimica et Cosmochimica Acta 61.23 (1997): 5099-5115.

Zacny, Kris, et al. "Mobile In-Situ Water Extractor (MISWE) for Mars, Moon, and Asteroids in Situ Resource Utilization." AIAA SPACE 2012 Conference & Exposition. (2012).

Zacny, Kris, et al. "Asteroid mining." AIAA SPACE 2013 Conference and Exposition. (2013).

VITA

Egboche Christopher Unobe hails from the North-Central Region of Nigeria, in West Africa. He received his B.Sc. in Geology from Ahmadu Bello University, Zaria in 2011. He began working towards a Master's degree in January 2015 at Missouri University of Science and Technology and during his time there, he actively participated in graduate research and teaching. He received his MS in Geological Engineering in July 2017 from Missouri University of Science and Technology.